Available online at www.sciencedirect.com
SCIENCE DIRECT®
Physics Reports 390 (2004) 453–551
PHYSICS REPORTS
www.elsevier.com/locate/physrep

Simple models for complex nonequilibrium fluids

Martin Kröger[a,b,*]

[a] *Polymer Physics, Materials Science, ETH Zentrum, 8092 Zürich, Switzerland*
[b] *Institut f. Theoretische Physik, Techn. Univ. Berlin, 10623 Berlin, Germany*

Accepted 15 October 2003
editor: E. Sackmann

Abstract

This review is concerned with the nonequilibrium dynamics and structure of complex fluids based on simple micro- and mesoscopic physical models which are not rigorously solvable by analytic methods. Special emphasis is placed on the finitely extendable nonlinear elastic (FENE) chain models which account for molecular stretch, bending, and topology. More coarse-grained descriptions such as primitive path models, and elongated particle models are reviewed as well. We focus on their inherently anisotropic material—in particular rheological—properties via deterministic and stochastic approaches. A number of representative examples are given on how simple (often high-dimensional) models can, and have been implemented in order to enable the analysis of the microscopic origins of the nonlinear viscoelastic behavior of polymeric materials. These examples are shown to provide us with a number of routes for developing and establishing coarse-grained (low-dimensional) models devoted to the prediction of a reduced number of significant material properties. At this stage approximations which allow for an analytical treatment are discussed as well. Concerning the types of complex fluids, we cover the range from flexible to semiflexible polymers in melts and solutions, wormlike micelles, structural suspensions including ferrofluids in field-induced anisotropic or liquid crystalline phases.

PACS: 05.10.−a; 83.10.Mj; 05.20.Dd

Keywords: Polymer; Non-Newtonian rheology; Flow; Structure; Dynamics; Viscosities; Orientation; Microscopic models; Mesoscopic models; Computer simulation; Molecular dynamics; Brownian dynamics; Stochastic differential equation; Constitutive equation; Kinetic theory; Liquid crystal; Ferrofluid; Semiflexible chain; Network; Tube model; Primitive path; Elongated particle; Order parameter

* Corresponding author. Polymer physics, Materials Science, ETH Zentrum, 8092, Zurich, Switzerland.
E-mail address: mkroeger@mat.ethz.ch (M. Kröger).

0370-1573/$ - see front matter © 2003 Elsevier B.V. All rights reserved.
doi:10.1016/j.physrep.2003.10.014

Contents

Nomenclature

(NE)MD, BD, MC	(Nonequilibrium) molecular/Brownian dynamics, Monte Carlo simulation
FP, EL, DE, HL	Fokker–Planck, Ericksen–Leslie, Doi–Edwarxds, Hinch–Leal
$\psi, p_{..}$	configurational/orientational distribution, statistical weighting factor
n, ρ, ϕ	bead number density, volume density, concentration
N, L, Q	number of beads within a single chain, chain contour, tube segment length
H, Q_0	Hookean spring coefficient, and maximum extension for FENE spring
b, T, β	FENE parameter ($b = HQ_0^2/k_BT$), temperature T, $\beta = (k_BT)^{-1}$
s	dimensionless chain contour position $0 < s < 1$
B, r	shape factor for elongated particles (1: rod, 0: sphere, -1: disk), axis ratio r
$\boldsymbol{x}_i$	position vector of bead i ($i = 1 \ldots N$)
$\boldsymbol{Q}, \boldsymbol{Q}_j$	connector(s) between adjacent beads within primitive chain (j=1 … $N-1$)
$\boldsymbol{u}, \boldsymbol{u}_j$	unit vector(s) tangential to the primitive path (normalized $\boldsymbol{Q}$)
$\mathscr{L}, \mathscr{L}_{\mathrm{FP}}$	angular operator $\mathscr{L} = \boldsymbol{u} \times \partial/\partial\boldsymbol{u}$, FP differential operator
$\boldsymbol{T}_{..}, \mathscr{D}_{..}$	orienting torque and damping terms entering the FP equation
$\overline{\bullet}$	anisotropic (symmetric traceless) part of tensor $\bullet$
$\boldsymbol{\sigma}, \boldsymbol{a}, \boldsymbol{a}_i$	stress tensor, (anisotropic) alignment tensor (of rank i), $\boldsymbol{a} \equiv \overline{\boldsymbol{a}_2}$
$\boldsymbol{g}$	dimensionless anisotropic 2nd moment of ψ for FENE dumbbells
$\boldsymbol{T}^{(k)}$	symmetry adapted basis tensors, Eqs. (8,9), $k \in \{0, 1, 2, 3, 4, \mathrm{tr}\}$
a_k, g_k	components of the alignment (gyration) tensor with respect to $\boldsymbol{T}^{(k)}$

$\boldsymbol{n}, S_{1,2,..}, \chi$	director in the EL theory, order parameters, flow alignment angle
τ, D	relaxation time, diffusion coefficient (sometimes labeled by a model)
λ	tumbling parameter or relaxation time (depends on context)
$\boldsymbol{M}, \boldsymbol{H}, h$	magnetization, magnetic field, Langevin parameter
$\boldsymbol{v}$	macroscopic flow field (shear flow $v_x = \dot{\gamma} y$, $\boldsymbol{v} = \dot{\gamma}\boldsymbol{e}^{(2)}$ for convenience)
$\boldsymbol{\kappa}, \boldsymbol{\omega}$	transposed macroscopic velocity gradient $(\nabla \boldsymbol{v})^{\mathrm{T}}$, vorticity $(\nabla \times \boldsymbol{v})/2$
$\boldsymbol{\gamma}, \boldsymbol{\Omega}$	symmetric and antisymmetric part of the velocity gradient ∇v
$\dot{\gamma}, \Gamma$	shear rate or dimensionless shear rate
$\eta, \eta^*, \eta_{1,2,3}, \Psi_{1,2}$	shear, complex shear, Miesowicz viscosities; 1st, 2nd viscometric function
$\alpha_{..}, \gamma_{..}$	EL viscosity and rotational viscosity coefficients
$a_{+,-,0}$	shear flow adapted components of the alignment tensor, Eq. (50)
ξ	parameter for the coarse-graining from atomistic to tapeworm (Section 8.8)
$m, \epsilon\sigma$	parameters of the Lennard-Jones and WCA potentials
$\delta_{ij}, \boldsymbol{I}$	Kronecker symbol $\delta_{i,j} \equiv 1$ $(i = j)$ and 0 otherwise; unit tensor of rank 3
ϵ	total antisymmetric tensor of rank three

1. Introduction

We hope that the complexity of the world is neither in contrast with the simplicity of the basic laws of physics [1] nor with the simple physical models to be reviewed or proposed in the following. However, physical phenomena occurring in complex materials cannot be encapsulated within a single numerical paradigm. In fact, they should be described within hierarchical, multi-level numerical models in which each sub-model is responsible for different spatio-temporal behavior and passes out the averaged parameters to the model, which is next in the hierarchy (Fig. 1). This review is devoted to the understanding of the nonequilibrium properties of complex fluids such as the viscoelastic behavior of polymeric liquids, the rheological properties of ferrofluids and liquid crystals subjected to magnetic fields, based on the architecture of their molecular constituents. The topic is of considerable concern in basic research for which models should be as simple as possible, but not simpler. Certainly, it also of technological relevance. Statistical physics and nonequilibrium thermodynamics are challenged by the desired structure–property relationships. Experiments such as static and dynamic light and neutron scattering, particle tracking, flow birefringence, etc. together with rheological measurements have been essential to adjust or test basic theoretical concepts, such as a 'stress-optic rule' which connects orientation and stress, or the effect of molecular weight, solvent conditions, and external field parameters on shape, diffusion, degradation, and alignment of molecules.

During the last decade the analysis of simple physical particle models for complex fluids has developed from the molecular computation of basic systems (atoms, rigid molecules) to the simulation of macromolecular 'complex' system with a large number of internal degrees of freedom exposed to external forces. This review should be in several aspects complementary to the ones which appeared recently in this journal. The foundations of molecular and Brownian dynamics methods for simple microscopic models for macromolecular systems have been extensively revisited [2]. Exciting

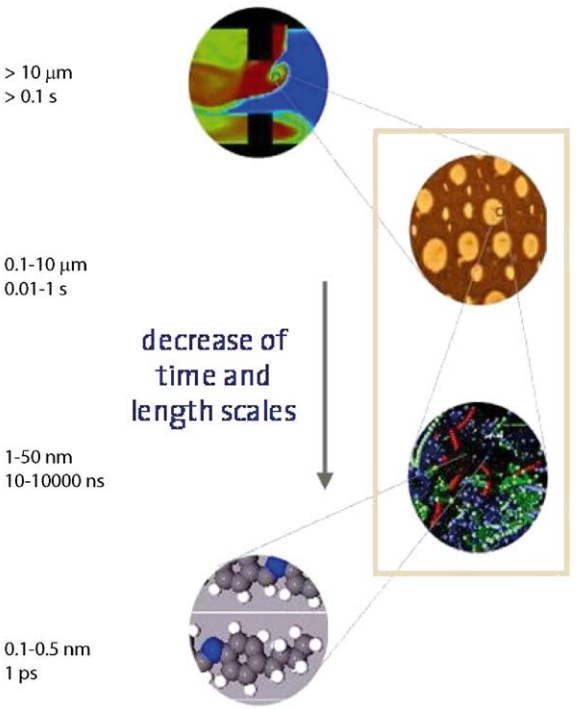

Fig. 1. Time and length scales of a typical polymer problem. In this review we are concerned with micro- and mesoscopic models (framed) which aim to describe physical behavior beyond equilibrium, beyond chemical details (bottom), and may be implemented into the macro-computation of complex flows (top).

progress in the field of physical models (of the simple type to be discussed in this article) for polymer adsorption at thermodynamical equilibrium has been reviewed [3]. Constructive methods of invariant manifolds for kinetic problems should be reviewed in a forthcoming paper [4]. Multi-scale simulation in polymer science with special emphasis on coarse-grained models (including a soft-ellipsoid model) has been recently reviewed by Kremer and Muller-Plathe [5]. In the light of these and further modern reviews on physical micro- and mesoscopic models to be mentioned below our focus is placed onto aspects which have been less extensively considered. Upon these are orientation and entanglement effects, the implications of stretchability, flexibility, order parameters, scission and recombination on material properties of anisotropic, dilute and concentrated polymeric bulk fluids in the presence of macroscopic flow and electromagnetic fields.

This review is first of all concerned with the applicability and suitability of bead–spring multi-chain models which incorporate finite extensibility of segments (so-called FENE models, cf. Table 1), molecular architecture and flexibility, and capture topological interactions. Second, it aims to give an overview about the range of applications of simple mesoscopic theories, in particular primitive path models and elongated particle models, where topological aspects are either approximately treated or disregarded. In view of a rapidly growing amount of research and number of publications on these topics, we try to present a balanced selection of simple, representative examples, connect them with related research, and thereby get in touch with a large—still not exhaustive—number of classical and

Table 1
Recommended nomenclature for finitely extendable nonlinear elastic (FENE) models (for dilute/concentrated solutions, melts, etc., cf. Fig. 3)

Model	For finitely extendable ...	Ref.
Simulation (*linear or branched chains*) NEMD/NEBD:		
FENE	Linear flexible classical polymers including dumbbells ($N = 2$)	[42] or Eq. (1)
FENE-*n*	Branched flexible classical polymers, including H-shaped (maximum functionality $n = 3$), star polymers ($n > 3$)	[42] or Eq. (1)
FENE-B	Linear semiflexible (B for 'bend') classical polymers, actin filaments	Eq. (48)
FENE-B*n*	Branched FENE-B, maximum functionality *n*, semiflexible classical networks	Eq. (48)
FENE-C	FENE which allows for unimolecular scission and recombination (C for 'cut'), wormlike micelles, equilibrium polymers	[31] or Eq. (5.2)
FENE-C*n*	FENE-C, maximum functionality *n*, living flexible and saturated networks	[31] or Eq. (5.2)
FENE-CB	Semiflexible FENE-C, associative polymer networks	Eq. (47)
FENE-CB*n*	Semiflexible FENE-Cn, living semiflexible non-saturated networks	Eq. (47)
Analytic (*linear chains*), *approximate explicit constitutive equations*:		
FENE-P	(P for 'Peterlin') approximation for FENE dumbbells, second moment as single state variable	[43–45]
FENE-P^2	Second-order Peterlin model	[37]
FENE-PM	Small set of equations approximating FENE-P chains	[46,47]
FENE-PCR	Also known as FENE-CR, Peterlin approximation plus a non-constant diffusion coefficient	[48]
FENE-PCD	Also known as FENE-CD, Peterlin approximation plus a configuration dependent diffusion coefficient	[49]
FENE-L	Second-order L-shaped closure model for FENE chains	[37]
FENE-LS	Simplified version of FENE-L	[50]
FENE-PMF	FENE-P supplemented by a mean-field (MF) interaction term modeling concentration effects	[51], Section 2.1

Models based on the Peterlin approximation should carry a '*P*', models for branched macromolecules should be suffixed by the maximum functionality considered (for linear chains, $n = 2$, it is understood that the suffix 2 is skipped). Many of the proposed simulation models have not been extensively studied, and analytic approaches such as FENE-P*n* (Peterlin approximation for branched FENE chains) are missing.

modern approaches. In order to keep this review short, we do not summarize knowledge available from standard text books. We therefore do not provide an introduction to the simulation methods used, the theory of stochastic differential equations, the statistical physics of simple, molecular, and macromolecular liquids, linear response theory, rheology, or experimental methods. We are going to cite the relevant original literature where implementation details can be found.

The existence of universality classes is significant for the theoretical description of polymeric complex fluids. Any attempt made at modeling polymer properties might expect that a proper

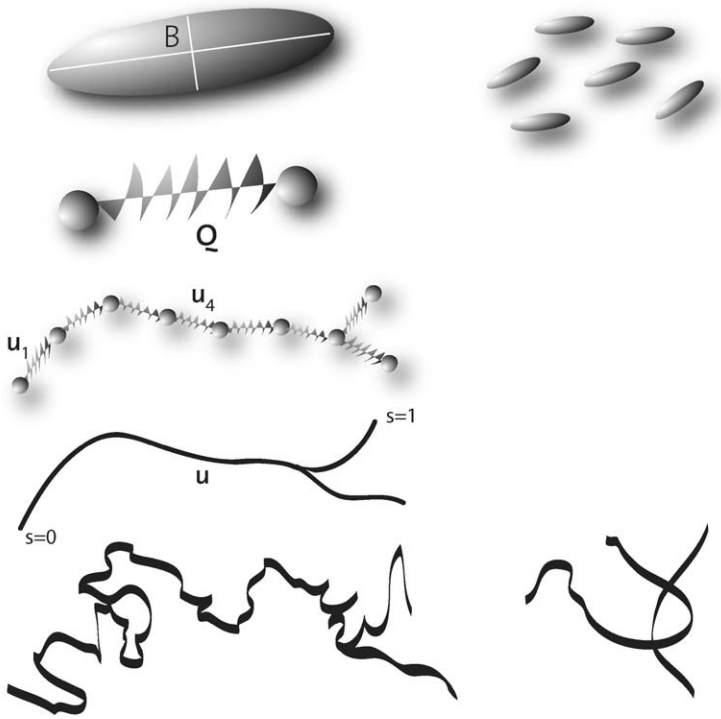

Fig. 2. Simple microscopic models for complex fluids with increasing level of abstraction and decreasing degrees of freedom (lhs, bottom to top), and their sketched range of application: (a) atomistically detailed polymer which accounts for anisotropic intermolecular interactions including entanglements, (b) coarse grained model via a mapping (Section 8.8) to a 'primitive path', (c) further approximated by a multibead (nonlinear FENE) chain, (d) further coarse-grained to a (FENE) dumbbell which accounts for entropic elasticity and orientation but not for entanglement effects, and (e) ellipsoids of revolution—including rigid rods, dissipative particles, with spherical or mean-field interaction. Models must meet the requirement of being thermodynamically admissible.

description must incorporate the chemical structure of the polymer into the model, since this determines its microscopic behavior. Thus a detailed consideration of bonds, sidegroups, etc. may be envisaged. However, the universal behavior that is revealed by experiments suggests that macroscopic properties of the polymer are determined by a few large scale properties of the polymer molecule. Structural details may be ignored even for microscopic (beyond-atomistic) models since at length scales in the order of nanometers, different polymer molecules become equivalent to each other, and behave in the same manner. This universal behavior justifies the introduction of crude mechanical models, such as bead–spring chain models, to represent real polymer molecules (Fig. 2).

The FENE chain model and its variations can be considered as a maximum coarse-grained, still brute force simulation model to the physical properties of polymeric fluids. These models did not fail to describe rheooptical material properties quite satisfactory when solved without approximation, but are often numerically expensive while conceptually simple. FENE chains constitute the appropriate level of description in order to test polymer kinetic theory [6,7], and assumptions made to simplify their analysis. In this article we should discuss several realizations in detail, hope to stimulate

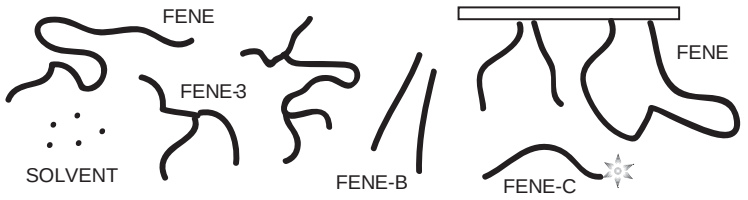

Fig. 3. Simple FENE models for a range of macromolecular fluids to be treated in a unified fashion: with/without solvent (simple fluid) for linear/star/branched, flexible/semiflexible, bulk/confined/tethered, non-/breakable macromolecules, cf. Table 1. Charged, tethered polymers have been excluded from the review since an excellent review is available in this series [3].

advanced treatments, and therefore disregard many other realizations (FENE chain models for star polymers, co-polymers, polymer blends, brushes, polyelectrolytes, in order to mention a few).

The dynamics of a single, fluorescing, DNA macromolecule held at one end by 'optical tweezers' and subjected to a uniform flow was successfully compared with simulations [8] of a FENE chain that accounted for the molecule's entropic elasticity, Brownian motion, and hydrodynamic drag. Using self-diffusion data and analytical expressions to obtain this drag in the limits of the undeformed coil and of the fully stretched thread, these results once more confirmed the success of the FENE chain model in predicting the rheological properties of simple polymeric systems. Excellent agreement between the theoretical predictions based on the FENE models and data from experimentation indicated that the model also seemed able [9] to interpret the underlying physical mechanisms for the dynamics of polymer solutions [10–12], melts [13–15], copolymer melts [16,17], brushes [18] not only in the quiescent state, but also subjected to flow fields [9,10,19–28]. During the last decade, the FENE chain model has been extended to incorporate the effect of scission, recombination (FENE-C) and branching of chains in order to investigate the formation and development of complex micellar systems and networks [16,29–32], cf. Fig. 3. The model has been further extended (FENE-B) to incorporate semiflexibility of chains [33–36], and studied in confined geometries. To give an overview about the range of applicability of the sufficiently detailed and simple microscopic models, we restrict ourselves to the formulation and analysis of models for particulate fluids and validate them against experimental data.

The nomenclature given in Table 1 is recommended in order make the search for results obtained for extensions of the original FENE dumbbell more comfortable. Actually, the most complete summary of the various 'analytic' FENE models may be found in [37]. Configuration tensor models such as the FENE-P and more general quasi-linear models (Johnson–Segalman, Gordon–Schowalter, Phan–Thien/Tanner, etc.) have been also developed in a fully nonisothermal setting [38–40]. NEMD together with a dissipative particle dynamics (DPD) thermostat had been successfully applied to study the shear-induced alignment transition of diblock copolymer melts, surfactants and liquid crystals in a large-scale system [16], based on an effective simplified continuum model for FENE dumbbells [41] biased towards phase separation. Simplified versions of FENE chain models neglect flexibility or finite extensibilty and have been widely used. Rigid elongated particles further neglect stretchability. Models dealing with these objects will be reviewed in certain detail as long as the simplified description turns out to be appropriate (unentangled: dilute polymers, rigid molecules: liquid crystals). Some space will be reserved for the discussion on the connection between the different levels

of description, projection operators, coarse-graining procedures, and the theory of nonequilibrium thermodynamics which sets a framework for simple physical models.

In Section 2 FENE dumbbell models are presented. In the quiescent state, polymers in dilute solution should have negligible interactions with each other on purely geometrical grounds, in contrast to semi-dilute or concentrated solutions and melts. The flow behavior of polymer solutions is, however, more complex than that of the familiar Newtonian fluids. Within these solutions shear thinning and the Weissenberg effect [6] are typical phenomena of technological importance. These effects are found to be strongly correlated with flow-induced conformational changes of the dissolved polymer chains and they can be dramatic in dilute solutions. Orientation and deformation of chain molecules can, and has been measured in flow birefringence light scattering and neutron scattering experiments (for methods and references see [52]), and via computer simulation [53–56]. For a review on molecular orientation effects in viscoelasticity we refer to Ref. [57]. For this introductory section we will be concerned with approximate solutions for FENE dumbbells (with $N = 2$ beads) in the infinitely dilute and dilute regimes.

Section 3 is next on the hierarchy and treats multibead chains ($N > 2$ beads) in dilute solutions. We start from a stochastic approach to polymer kinetic theory. The model takes into account configuration-dependent hydrodynamic interaction (HI) and simplifies to the Zimm bead–spring chain model in the case of preaveraged HI, for which parameter-free 'universal ratios' such as the ratio between radius of gyration and hydrodynamic radius are known. The Chebyshev polynomial method and a variance reduction simulation technique [58] are revisited to implement an efficient NEBD simulation. The full dependence of several characteristic ratios vs both chain length and hydrodynamic interaction parameter is resolved, and compared with analytical and experimental results. Polymer solutions under good solvent conditions have been also studied extensively via NEMD by taking into account explicit solvent particles, e.g., in Refs. [53–56,59]. In that case, hydrodynamic interactions and excluded volume are incorporated through momentum transfer and a WCA potential between beads, respectively.

Section 4 demonstrates insights obtained by NEMD into the microscopic origin of the nonlinear viscoelastic properties of (dense) polymer melts by using a FENE chain model. Stress–strain relationships for polymer melts are the main requirement for the conventional flow simulation of polymer processing, useful in modelling industrial applications including injection moulding, film blowing, and extrusion. The reliability and accuracy of such simulations depends crucially on the constitutive equations. Although closed-form phenomenological models have been widely used in research and commercial codes, their degree of success is limited because of a lack of physical ingredient on the molecular level. For the purpose of realistic modelling, and further development of semiempirical constitutive equations, full FENE chain models are shown to be uniquely suited.

Section 5 extends the FENE chain system in several directions. We offer explicit examples of recently established models: wormlike micellar systems modelled by a FENE-C potential, model liquid crystals composed of semiflexible FENE chains, as well as a model for semiflexible (FENE-B, actin) filaments and networks. Results for the models are obtained by NEMD or NEBD, though we will also discuss analytic descriptions that are able to guide the interpretation of important aspects of the results.

Section 6 offers illustrative examples on how to formulate and handle kinetic model equations for primitive paths (coarse-grained atomistic chains) by approximate analytical or 'exact' numerical treatments. The role of topological interactions is particularly important, and has given rise to

a successful theoretical framework: the 'tube model'. Progress over the last 30 years had been reviewed in the light of specially synthesized model materials, an increasing palette of experimental techniques, simulation and both linear and nonlinear rheological response in Ref. [7]. Here we review a selected number of improved versions of primitive path models which allow to discuss the effect of approximations on the linear and nonlinear rheological behavior of polymer melts. Brute force FENE chain simulation results summarized in the preceding chapters are used to test the assumptions made in the formulation of these kinetic models.

Section 7 deals with elongated particle models. There are many early approaches in the literature to the modelling of fluids with simple microstructure. For example, equations for suspensions of rigid particles have been calculated by averaging the detailed motion of the individual particles in a Newtonian fluid. In particular, the solution for the motion of a single ellipsoid of revolution in a steady shear [60] in terms of a Fokker–Planck (FP) equation has been used to determine the governing equations for the slow flow of a dilute suspension of noninteracting particles. In more concentrated systems, various approximations to the particle motions have been used. Hinch and Leal [61] have named this approach, based upon a detailed analysis of the microstructure, 'structural'. Alternatively, 'phenomenological' continuum theories for anisotropic fluids have been postulated. These theories tend to be quite general, being based upon a small number of assumptions about invariance. Perhaps the most successful and well-known example is the Ericksen–Leslie (EL) director theory for uniaxial nematic liquid crystals. Additionally, numerous models have been developed and discussed in terms of symmetric second and higher order tensorial measures of the alignment. Given these diverse methods of derivation and apparently diverse domains of application, one may ask if, and how, such diverse approaches may be interrelated. The answer and several examples (including concentrated suspensions of rod-like polymers, liquid crystals, ferrofluids) are given in this section.

Section 8 is an attempt to review several strategies and open questions concerning the thermodynamically admissible description of complex nonequilibrium fluids on different levels (conc. length and time scales or structural details) of description. We will touch the theory of projection operators which act on the space coordinates of atoms such that the resulting quantities serve either as slow variables needed to proceed with a separation of time scales in the corresponding Langevin equations. Attempts being made to characterize the system with (a few) structural quantities, known to be within reach of analytical theoretical descriptions and/or accessible through experimentation will be reviewed. A similar formal structure, namely a symplectic structure, for thermodynamics and classical mechanics was noted early by Peterson [62] in his work about the analogy between thermodynamics and mechanics. He notes that the equations of state, by which he means identical relations among the thermodynamic variables characterizing a system, are actually first-order partial differential equations for a function that defines the thermodynamics of the system. Like the Hamilton–Jacobi equation, such equations can be solved along trajectories given by Hamilton's equations, the trajectories being quasi-static processes, obeying the given equation of state. This gave rise to the notion of thermodynamic functions as infinitesimal generators of quasi-static processes, with a natural Poisson bracket formulation. In this case the formulation of thermodynamic transformations is invariant under canonical coordinate transformations, just as with classical mechanics. These illuminating ideas have been further developed [63,64] and generalized Poisson structures are now recognized in many branches of physics (and mathematics). We are therefore also concerned with the formulation of so-called 'thermodynamically admissible' simple models for complex fluids, where admissibility is assumed whenever the complete set of state variables characterizing the systems

possess the 'General Equation for the Non-Equilibrium Reversible-Irreversible Coupling' (GENERIC) structure [40]. This structure (a special representation of a less predictive 'Dirac' structure which also contains the Matrix model by Jongschaap [65] as a special case, connections between thermodynamic formalism are revisited in [66]) requires a Poisson bracket for the reversible part of the dynamics. Specifically, the time-structure invariance of the Poisson bracket as manifested through the Jacobi identity has been used to derive constraint relationships on closure approximations [67]. An explicit coarsening procedure from atomistic chains (or FENE chains, Section 4) to primitive paths (Section 6, Fig. 2) is given in Section 8.8.

2. FENE dumbbell models in infinitely diluted solution

Dumbbell models are very crude representations of polymer molecules. Too crude to be of much interest to a polymer chemist, since it in no way accounts for the details of the molecular architecture. It certainly does not have enough internal degrees of freedom to describe the very rapid motions that contribute, for example, to the complex viscosity at high frequencies. On the other hand, the elastic dumbbell model is orientable and stretchable, and these two properties are essential for the qualitative description of steady-state rheological properties and those involving slow changes with time. For dumbbell models one can go through the entire program of endeavor—from molecular model to fluid dynamics—for illustrative purposes, in order to point the way towards the task that has ultimately to be performed for more realistic models. According to [6], dumbbell models must, to some extend then, be regarded as mechanical playthings, somewhat disconnected from the real world of polymers. When used intelligently, however, they can be useful pedagogically and very helpful in developing a qualitative understanding of rheological phenomena.

Before we turn to FENE chain models with increasing complexity and predictive power for entangled polymeric systems, we should summarize some of the efforts undertaken to analyze various approximations to the original FENE dumbbell model for infinitely dilute solutions. This model can be rigorously solved by Brownian dynamics (BD) and had been used in the pioneering micro–macro simulations [68].

A FENE dumbbell consists of two beads (mass points) connected with a nonlinear spring. Its internal configuration is described by a connector vector $\boldsymbol{Q}$. The FENE spring force law is given by [42,45,6]

$$\boldsymbol{F}^{(\mathrm{FENE})} = -\frac{H\boldsymbol{Q}}{1 - Q^2/Q_0^2}\ , \tag{1}$$

with H and Q_0 denoting the (harmonic) spring coefficient and the upper limit for the dumbbell extension. The singularity of the force at $Q^2 = Q_0^2$ is the mathematical implementation of the dumbbell's finite extensibility. The FENE spring is a valid approximation to a chain of freely rotating elements (the Kramers chain) as long as the number of elements is large, and it gives a reasonable approximation for the entropy of chains of finite length. An infinitely dilute FENE polymer solution is modeled by a suspension of FENE dumbbells in a continuous, Newtonian solvent, where the dumbbell beads are centers of a hydrodynamic drag force, exerted by the surrounding solvent. Assuming Stokes law the drag force is considered being proportional to the relative velocity between

solvent and bead, with a constant ζ, the friction coefficient. Point of departure for the statistical analysis is the diffusion equation for the configurational distribution function $\psi(\boldsymbol{Q},t)$

$$\frac{\partial\psi}{\partial t}=\frac{2k_BT}{\zeta}\,\Delta\psi+\frac{2}{\zeta}\boldsymbol{\nabla}\cdot\{\boldsymbol{F}\psi\}-\boldsymbol{\nabla}\cdot\{(\boldsymbol{\kappa}\cdot\boldsymbol{Q})\psi\}\ . \tag{2}$$

Here, T is the absolute temperature, k_B denotes Boltzmann's constant, and $\boldsymbol{F}=\boldsymbol{F}^{(\mathrm{FENE})}$ denotes the deterministic force. The Laplacian and nabla operators refer to derivatives in configuration space. Time dependent expectation values with respect to ψ will subsequently be denoted by angular brackets $\langle\ldots\rangle$, and the FENE parameter $b\equiv HQ_0^2/k_BT$, the relaxation time $\tau\equiv\zeta/4H$ and a dimensionless shear parameter $\Gamma\equiv\tau\gamma$ will be often used. We will be (throughout this review) concerned with homogeneous flow whose transposed velocity gradient is denoted as $\boldsymbol{\kappa}\equiv(\boldsymbol{\nabla v})^{\dagger}$, i.e., $\boldsymbol{v}=\boldsymbol{\kappa}\cdot\boldsymbol{r}$. This enables us to carry out the calculations in the frame of a special coordinate system, the one fixed by the center of mass of the dumbbell, the directions of the axes are specified by the flow geometry. Notice, that (2) can be solved analytically only for potential flows [6].

The FENE dumbbell model has been originally used to describe non-Newtonian rheological effects in monodisperse and idealized infinitely dilute polymer solutions with [69–71] or without hydrodynamic interaction [42,45], and to interpret scattering patterns [71–73]. Analytic theories—except those we are going to illustrate in more detail in the next section—have been restricted to infinitely dilute solutions based on a one-particle-description, in which interactions with surrounding molecules have not been considered. The FENE dumbbell with the pre-averaging Peterlin approximation (FENE-P) has been used extensively to describe the rheological behavior of dilute [6] polymer solutions. The model is, however, severely limited, since it cannot describe the broad distribution of relaxation times that real polymer molecules possess. Detailed comparisons of various FENE dumbbell models for dilute solutions conc. its rheological behavior in shear, elongational [74,75] and also turbulent flows [76] are available. It was shown that while in the linear viscoelastic limit and in elongational flow the behavior is close, in shear and turbulent flows serious deviations appear. Fairly understood (in terms of a FENE-P model, cf. Ref. [75]) is the effect of drag reduction upon adding small amounts of polymers to highly viscous liquid, which are transported through (long) pipelines.

The FENE-P chain, which is conceptually located between FENE-dumbbell models and full FENE chain models, however, has not been as widely used because of the large number of coupled equations that must be solved simultaneously in order to calculate the stress tensor. In Ref. [46] the FENE-PM chain, as a 'good' and efficient approximation to the FENE-P chain had been introduced. The reduced number of equations greatly expedites calculations for longer chains. It had been demonstrated [77,78] by means of standard and stochastic numerical techniques that the pre-averaging Peterlin approximation used to derive the FENE-P macroscopic constitutive equation has also a significant impact on the statistical and rheological properties of the full FENE chain model.

2.1. FENE-PMF dumbbell in finitely diluted solution

Results of light scattering experiments on dilute polymer solutions in various concentrations below the (equilibrium) overlap concentration have revealed a strong concentration dependence of the polymer conformation in shear flow [79]. In order to present yet another candidate for describing the observed phenomena in an approximate fashion, for illustrative purposes, in order to introduce the Peterlin approximation and basis tensors for later use, and before turning to the recommended

full FENE models in the next sections, let us treat the FENE dumbbell model supplemented by a mean field term which describes the concentration dependence in the frame of a one-particle description. The basic idea [55] is to consider interactions between different molecules in an averaged approximation.

2.2. Introducing a mean field potential

The mean field term models the effect of concentration induced anisotropy caused by inter- as well as intramolecular interactions in the polymer solution. An expression for the mean field potential can be adapted from theories for concentrated solutions of rodlike polymers [80] and liquid crystals [81,82] or obtained by carrying out a finite multipole expansion of the intermolecular pair potentials, in which the unknown multipole moments are taken to be phenomenological coefficients [83]. The series has to be written down to an order, which, after averaging with the configuration distribution function, leads to a nonconstant and anisotropic expression involving the tensor of gyration, i.e. up to the quadrupole–quadrupole interaction. The corresponding mean field force reads

$$\boldsymbol{F}^{(\mathrm{MF})} = \frac{k_B T}{Q_0^2} f\left(\frac{c}{c^*}\right) \langle\, \overline{\boldsymbol{QQ}} \,\rangle^* \cdot \boldsymbol{Q} \ . \tag{3}$$

The symbol $\overline{\ldots}$ denotes the irreducible (symmetric traceless) part of a tensor, $\overline{\boldsymbol{QQ}} = \boldsymbol{QQ} - \boldsymbol{I}/3$, n is the concentration (mass density) of the polymers in solution, n^* is a reference concentration. The scalar function f represents a phenomenological coefficient. If it is assumed to be zero for infinitely dilute solutions data of [79] suggest $f = (c/c^*)^{1/3}$ with a characteristic concentration c^*. This means f is proportional to the reciprocal average distance between the molecules. The ansatz differs from the ones used in [80–82] in the respect that a connector vector $\boldsymbol{Q}$ with variable length enters the expression for the potential instead of a unit vector specifying the direction of a rod.

2.3. Relaxation equation for the tensor of gyration

By multiplying (2) for homogeneous flows with $\boldsymbol{QQ}$ and subsequent integration by parts, with $\boldsymbol{F} = \boldsymbol{F}^{(\mathrm{FENE})} + \boldsymbol{F}^{(\mathrm{MF})}$, we obtain

$$\frac{\mathrm{d}}{\mathrm{d}t}\langle \boldsymbol{QQ} \rangle = \frac{4k_B T}{\zeta}\boldsymbol{I} + \frac{4}{\zeta}\{\langle \boldsymbol{F}^{(\mathrm{FENE})}\boldsymbol{Q}\rangle + \langle \boldsymbol{F}^{(\mathrm{MF})}\boldsymbol{Q}\rangle\} + \boldsymbol{\kappa}\cdot\langle \boldsymbol{QQ}\rangle + \langle \boldsymbol{QQ}\rangle \cdot \boldsymbol{\kappa}^{\dagger} \ . \tag{4}$$

The second moment will be expressed in a dimensionless form $\boldsymbol{g} \equiv \langle \boldsymbol{QQ}\rangle^* \equiv \langle \boldsymbol{QQ}\rangle/Q_0^2$. For a stationary shear flow (plane Couette geometry) with shear rate $\dot{\gamma}$ the second-rank gradient tensor $\boldsymbol{\kappa}$ is given by $\kappa_{\mu\nu} = \dot{\gamma}\,\delta_{\mu 1}\delta_{2\nu}$ if we denote with $\boldsymbol{e}^{(1)}$ the flow direction, $\boldsymbol{e}^{(2)}$ the gradient direction, and $\boldsymbol{e}^{(3)} = \boldsymbol{e}^{(1)} \times \boldsymbol{e}^{(2)}$ the vorticity direction. For this geometry the orientation angle χ and the mean square dumbbell elongation $\langle Q^2\rangle$ are related to the tensor $\boldsymbol{g}$ by [84] $\tan 2\chi = (2g_{12})/(g_{11} - g_{22})$, and $\langle Q^2\rangle/Q_0^2 = g_{\lambda\lambda} = \mathrm{Tr}\,\boldsymbol{g}$, while the tensor of gyration $\frac{1}{4}\langle \boldsymbol{QQ}\rangle$ equals $\frac{1}{4}Q_0^2\,\boldsymbol{g}$. In dilute solutions the tensor of gyration is assumed to be isotropic under equilibrium conditions. By construction the mean field potential vanishes under equilibrium conditions, since it is linear in the irreducible part of the gyration tensor.

Next, we wish to obtain a closed approximate set of equations for a stationary solution of the relaxation equation (4). Inserting (1) and (3) and the explicit expression for $\boldsymbol{\kappa}$ into (4) yields

$$\frac{1}{b}\,\delta_{\mu\nu} = \left\langle \frac{Q_\mu Q_\nu}{Q_0^2 - Q^2} \right\rangle - \frac{1}{b} f\left(\frac{c}{c^*}\right) \langle \overline{Q_\mu Q_\lambda} \rangle^* \langle Q_\lambda Q_\nu \rangle^* - \Gamma\{\delta_{\mu 1}\langle Q_2 Q_\nu\rangle^* + \delta_{\nu 1}\langle Q_2 Q_\mu\rangle^*\} \ . \tag{5}$$

We choose a standard decoupling approximation, referred to as Peterlin approximation [6,43,44], modified such that it is exact in equilibrium. Thus, a term equal to zero is added and subsequently approximated by carrying out the involved averaging under equilibrium conditions. This can be done, because the equilibrium distribution function ψ_{eq} for the given problem is known [42,6]. Coupled moment equations may be alternatively derived by making use of a Taylor series expansion for the expectation value associated with the FENE force term, cf. [51,45,6]. One obtains

$$\begin{aligned}\left\langle \frac{Q_\mu Q_\nu}{Q_0^2 - Q^2} \right\rangle &\approx \frac{\langle Q_\mu Q_\nu\rangle^*}{1 - \langle Q^2\rangle^*} - \left\{ \frac{\langle Q_\mu Q_\nu\rangle^*_{\mathrm{eq}}}{1 - \langle Q^2\rangle^*_{\mathrm{eq}}} - \left\langle \frac{Q_\mu Q_\nu}{Q_0^2 - Q^2} \right\rangle_{\mathrm{eq}} \right\} \\ &= \frac{\langle Q_\mu Q_\nu\rangle^*}{1 - \langle Q^2\rangle^*} - \left\{ \frac{1}{b+2} - \frac{1}{b} \right\} \delta_{\mu\nu} \ . \end{aligned} \tag{6}$$

Use had been made of the isotropic moments (after Taylor expansion) which become $\forall_n \langle Q^{2n}\rangle^*_{\mathrm{eq}} \approx \prod_{k=1}^{n}(2k+1)/(b+2k+3)$. Insertion of the (6) into (5) yields the desired closed set of nonlinear equations

$$\frac{\boldsymbol{g}}{1 - \mathrm{Tr}\,\boldsymbol{g}} - \frac{1}{b} f\left(\frac{n}{n^*}\right) \overline{\boldsymbol{g}} \cdot \boldsymbol{g} - \tau(\boldsymbol{\kappa}\cdot\boldsymbol{g} + \boldsymbol{g}\cdot\boldsymbol{\kappa}^\dagger) = \frac{\boldsymbol{I}}{b+2} \ . \tag{7}$$

Explicit equations for the components $g_{\mu\nu}$ can be derived most conveniently in a symmetry-adapted form.

2.4. Symmetry adapted basis

The symmetric second-rank tensor of gyration has six independent components. In the plane Couette geometry two more components vanish for symmetry reasons, because invariance under the transformation $\boldsymbol{e}^{(3)} \to -\boldsymbol{e}^{(3)}$ is required. An exception will be discussed in Section 7.6. The corresponding four independent components of the second moment are g_{11}, g_{12}, g_{22}, and g_{33}. We transform (7) to a version which separates the irreducible and trace-dependent parts of the tensor of gyration, since these are especially emphasized in the terms associated with the FENE and mean field forces. The irreducible part of the tensor is decomposed with respect to a set of pseudospherical cartesian basis tensors. This will result in a simple expression for the orientation angle and in a more tractable expansion for small shear parameters. The resulting equations are easily decoupled in this case. A set of orthonormal basis tensors $\boldsymbol{T}^{(k)}$ with $k = 0, 1, 2, \mathrm{tr}$ is chosen according to [85,86] whose elements are given by

$$\begin{aligned} &\boldsymbol{T}^{(0)} = (3/2)^{1/2}\,\overline{\boldsymbol{e}^{(3)}\boldsymbol{e}^{(3)}}, \quad \boldsymbol{T}^{(1)} = 2^{-1/2}(\boldsymbol{e}^{(1)}\boldsymbol{e}^{(1)} - \boldsymbol{e}^{(2)}\boldsymbol{e}^{(2)}) \ , \\ &\boldsymbol{T}^{(2)} = 2^{1/2}\,\overline{\boldsymbol{e}^{(1)}\boldsymbol{e}^{(2)}}, \quad \boldsymbol{T}^{(tr)} = 3^{-1/2}(\boldsymbol{e}^{(1)}\boldsymbol{e}^{(1)} + \boldsymbol{e}^{(2)}\boldsymbol{e}^{(2)} + \boldsymbol{e}^{(3)}\boldsymbol{e}^{(3)}) \end{aligned} \tag{8}$$

with the orthonormality relation $\forall_{k,l} T^{(k)}_{\mu\nu} T^{(l)}_{\mu\nu} = \delta^{kl}$. Note, that $\boldsymbol{T}^{(0)}$, $\boldsymbol{T}^{(1)}$, and $\boldsymbol{T}^{(2)}$ are symmetric traceless, while $\boldsymbol{T}^{(tr)}$ is associated with the trace of a tensor. Two more 'symmetry braking' basis tensors

$$\boldsymbol{T}^{(3)} = 2^{1/2}\,\overline{\boldsymbol{e}^{(1)}\boldsymbol{e}^{(3)}}, \quad \boldsymbol{T}^{(4)} = 2^{1/2}\,\overline{\boldsymbol{e}^{(2)}\boldsymbol{e}^{(3)}} \tag{9}$$

will be used in connection with 'rheochaotic states' in Section 7.6. The tensor $g_{\mu\nu}$ can be decomposed according to $g_{\mu\nu} = \sum_k g_k T^{(k)}_{\mu\nu}$ with $g_k = T^{(k)}_{\mu\nu} g_{\mu\nu}$. The orientation angle χ and the (mean square) dumbbell elongation $\langle Q^2\rangle^*$ now take the form $\tan 2\chi = g_2/g_1$, $\langle Q^2\rangle^* = \sqrt{3} g_{\rm tr}$. Using the decomposition and the orthonormality relation a set of coupled non-linear equations for the pseudospherical and trace-dependent components of $\boldsymbol{g}$ is derived from (7):

$$\begin{aligned}
g^{(0)} &= -\Gamma\frac{\sqrt{3}}{3} g_2 - J((g_1^2 + g_2^2 - g_0^2) + \sqrt{2} g_0 g_{\rm tr}) \,, \\
g^{(1)} &= \Gamma g_2 - J(2 g_1 g_0 - \sqrt{2} g_1 g_{\rm tr}) \,, \\
g^{(2)} &= \Gamma\left(\frac{g_{\rm tr}\sqrt{6}}{3} + \frac{g_0\sqrt{3}}{3} + g_1\right) - J(2 g_2 g_0 - \sqrt{2} g_2 g_{\rm tr}) \,, \\
g^{(\rm tr)} &= \Gamma\frac{\sqrt{6}}{3} g_2 + J(g_0^2 + g_1^2 + g_2^2) + \frac{\sqrt{3}}{b+2} \,, \\
\text{with } g^{(i)} &\equiv \frac{g_i}{1 - \sqrt{3}\, g_{\rm tr}}, \quad J \equiv b^{-1} f(c/c^*)/\sqrt{6} \,.
\end{aligned} \tag{10}$$

Note that Eqs. (6), (7), (10) correct some misprints in [51]. We cannot give an analytical solution of the system without carrying out further approximations, which would result in a significant change of the model. For small dimensionless shear rates Γ, however, exact analytical expressions for the orientation angle and the dumbbell elongation are $\tan 2\chi = (1-\phi)/(\tilde{b}\,\Gamma)$ and

$$\langle Q^2\rangle^* = \frac{3}{b+5}\left\{1 + \frac{2}{3}\left(1 - \left(1 - \frac{1}{\sqrt{2}}\right)\phi\right)(1-\phi)^{-2}\tilde{b}^3\,\Gamma^2\right\} \tag{11}$$

with $\phi = \phi(c) \equiv f(c/c^*)(b+2)/(b(b+5)^2)$ and $\tilde{b} \equiv (b+2)/(b+5)$. These expressions show that for a given shear rate the orientation angle decreases and the radius of gyration increases with rising (still small) concentration. Of course, they reduce to the ones known for FENE dumbbels at zero concentration ($c = \phi = 0$). For Hookean dumbbell the relations for χ and $\langle Q^2\rangle^*$ are obtained for $b \to \infty$, $\tilde{b} = 1$.

For larger shear rates the system of coupled nonlinear equations (10) has to be solved numerically. Solutions are restricted to a limited range of f (or ϕ). To illustrate the influence of the mean field term, results are presented for a fixed value of $b = 1$ for the FENE parameter (the significance of b in the original theory has been well analyzed in [42,45]). For comparison, we will show plots for the dumbbell elongation and the orientation angle for various b and different concentration parameters.

In Fig. 4 the radius of gyration in units of the equilibrium radius is given for different concentrations vs dimensionless shear rate Γ. For given rate, the radius of gyration increases with rising concentration. The relative increase is larger for smaller shear rates, because with rising shear, the deformation is limited by Q_0. Fig. 5 shows the related plot for the orientation angle. For all

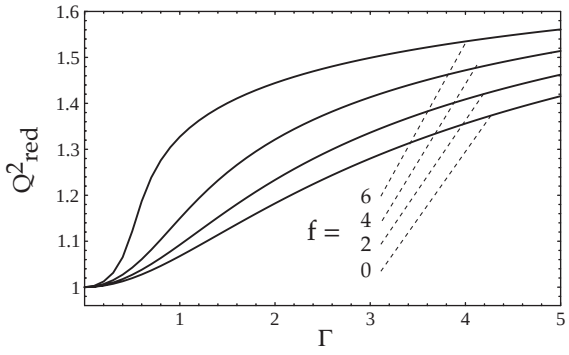

Fig. 4. Radius of gyration in units of its equilibrium value vs shear parameter Γ for concentration parameters of $f = 0$, 2, 4, and 6, and a FENE parameter $b = 1$ [51].

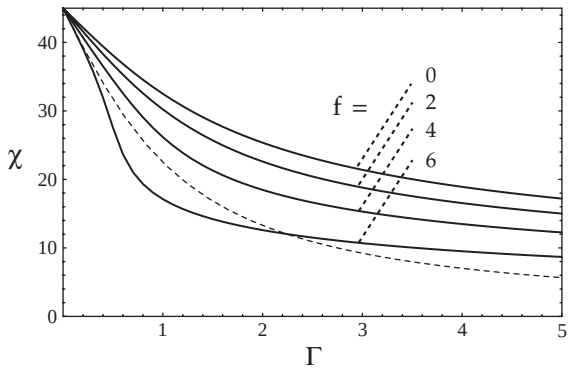

Fig. 5. Orientation angle versus shear parameter Γ, see Fig. 4 for the choice of parameters. Dashed curve according to a linear bead spring theory resulting in $\tan 2\chi = \Gamma^{-1}$ [51].

concentrations the curve differs from the simple law $\tan 2\chi \propto \dot{\gamma}^{-1} \propto \Gamma^{-1}$, which results from linear theories or from perturbation results of low order. A dashed curve referring to the simple law is given for comparison.

The quantity $g \equiv \sqrt{g_1^2 + g_2^2}$ shown in Fig. 6 is a measure for the degree of alignment into the shear plane. As expected, we find an increasing anisotropy with rising concentration. The influence of the FENE parameter b is presented in Figs. 7 and 8. The shear rate is given in units of a characteristic time constant $\lambda = \tau\, b/3$ for FENE dumbbells in this case to achieve comparability with results from the original theory [42,45]. The mean field influence is controlled by variation of ϕ which characterizes the mean field magnitude independently of b in the case of small shear rates. In the range of higher shear rates the dumbbell elongation falls with rising concentration parameter (Fig. 7). Especially for higher b, the elongation is now limited by the mean field, not by the finite extensibility.

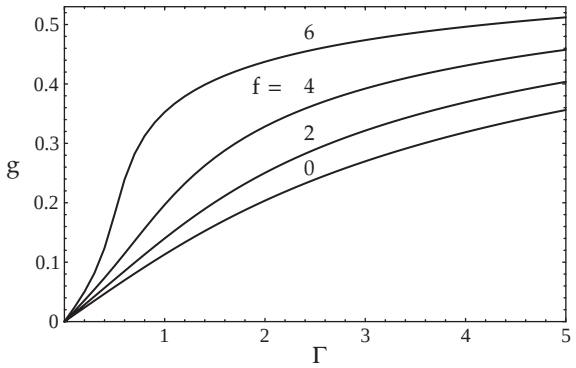

Fig. 6. Quantity $g = (g_1^2 + g_2^2)^{1/2}$ related to pseudospherical components of the tensor of gyration vs shear parameter Γ [51].

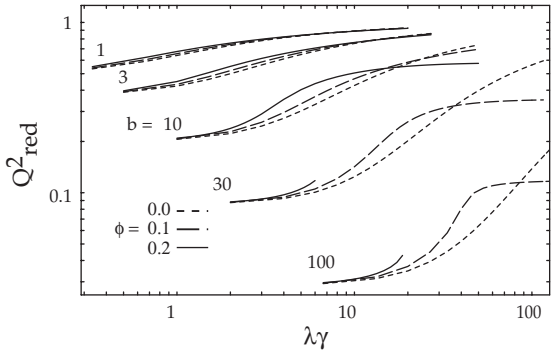

Fig. 7. FENE dumbbell elongation vs shear parameter $\lambda\dot{\gamma} = b\Gamma\dot{\gamma}/3$ for various b and different concentration parameters ϕ [51].

2.5. Stress tensor and material functions

The polymer contribution to the stress tensor $\boldsymbol{\tau}^p$ for the FENE dumbbell takes the form of an extended Kramers expression [6], cf. Section 8.7,

$$\boldsymbol{\sigma}^p = n\langle(\boldsymbol{F}^{(\mathrm{FENE})} + \boldsymbol{F}^{(\mathrm{MF})})\boldsymbol{Q}\rangle + n\,k_B T\boldsymbol{I}\ . \tag{12}$$

Using (4) and the definition of the convected time derivative $\delta/\delta t(\ldots) \equiv \mathrm{d}/\mathrm{d}t(\ldots) - \boldsymbol{\kappa}\cdot(\ldots) - (\ldots)\cdot\boldsymbol{\kappa}^\dagger$ leads to $\boldsymbol{\sigma}^p = (n\zeta/4)\delta/\delta t\langle\boldsymbol{QQ}\rangle$. This is similar to a Giesekus expression [6] resulting from the original FENE dumbbell theory. The shear flow material functions for the fluid in a plane Couette geometry

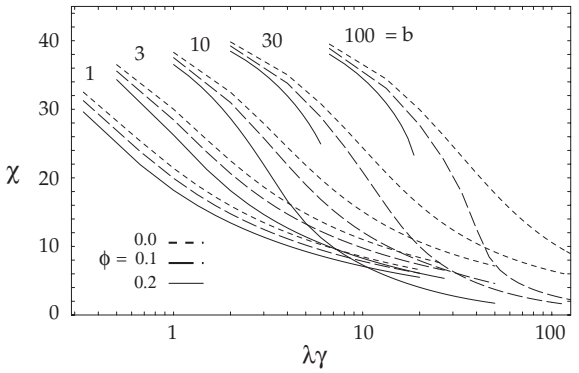

Fig. 8. Orientation angle vs shear parameter $\lambda\dot{\gamma}$ for various b and different concentration parameters ϕ [51].

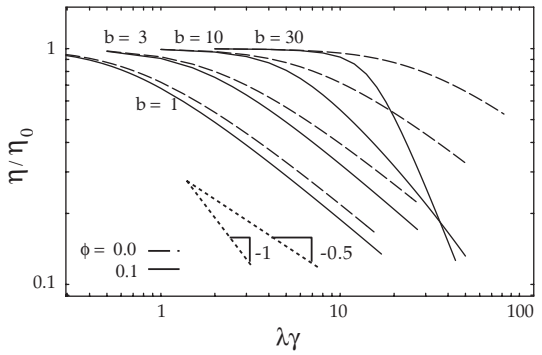

Fig. 9. Reduced viscosity vs shear parameter $\lambda\dot{\gamma}$ for various b and different concentration parameters ϕ [51].

[6] are therefore given as functions of the tensor of gyration. In particular, we have

$$\frac{\eta_p}{\eta_{p,0}} = (b+5)\, g_{22} = (b+5)\left(\frac{\sqrt{3}}{3}\, g_{\mathrm{tr}} - \frac{\sqrt{6}}{6}\, g_0 - \frac{\sqrt{2}}{2}\, g_1\right) \tag{13}$$

for the reduced viscosity $\eta_p \equiv \tau_{xy}\dot{\gamma}^{-1}$ and

$$\frac{\Psi_1}{\Psi_{1,0}} = (b+5)\,\frac{g_{12}}{\Gamma} = (b+5)\,\frac{\sqrt{2}g_2}{2\Gamma} \tag{14}$$

for the reduced first viscometric function $\Psi_1 \equiv (\sigma_{xx} - \sigma_{yy})\dot{\gamma}^{-2}$. The 2nd viscometric function $\Psi_2 \equiv (\sigma_{yy} - \sigma_{zz})\dot{\gamma}^{-2}$ is equal to zero in the present case. Fig. 9 shows the reduced viscosity versus shear parameter $\lambda\dot{\gamma}$ for various b and two different concentration parameters ϕ. There is a stronger shear thinning effect for $\phi \neq 0$. These results compare well with data from light scattering experiments [79,51] such that there is no need to present detailed comparisons (which can be also found in Refs. [87,88]).

With increasing concentration (close to and above the overlap concentration) correlations between different molecules become stronger and the one-particle description has to be abandoned [89,90].

Scattering experiments have been performed on semi-dilute polymer solutions at rest and in laminar shear flow at different temperatures by SANS [91] and by (small angle) light scattering (SALS) [92–94] as well as by dynamic light scattering [95].

2.6. Reduced description of kinetic models

Numerical implementation of kinetic models in direct numerical flow calculations is in general computationally expensive. This is especially true for chain models to be discussed in later sections. However, kinetic models of polymer dynamics may serve as a starting point for the derivation of constitutive equations. Derivations are not straightforward but require approximations to the underlying kinetic model. The need for so-called closure approximations occurs also in other branches of statistical physics and several suggestions for such approximations have been proposed in the literature (see e.g. [96] and references therein). The frameworks 'reduced description' and 'invariant manifolds' have been developed to efficiently obtain an approximate solution for FP equations for FENE dumbbells and liquid crystals [97] and of the types to be discussed later in this review. In Ref. [98] the authors give a compact non-technical presentation of two basic principles for reducing the description of nonequilibrium systems based on the quasiequilibrium approximation. These two principles are: Construction of invariant manifolds for the dissipative microscopic dynamics, and coarse-graining for the entropy-conserving microscopic dynamics. It had been demonstrated in general and illustrated how canonical distribution functions are obtained from the maximum entropy principle, how macroscopic and constitutive equations are derived therefrom and how these constitutive equations can be implemented numerically [99,97]. A measure for the accuracy of the quasiequilibrium approximation had been proposed that can be evaluated while integrating the constitutive equations. Within the framework of reduced description, equations of change for the 'dual' variables appearing in an ansatz for the distribution function play a major role. The method has been further applied to ferrofluids in Ref. [100]. Constructive methods of invariant manifolds for kinetic problems are going to be reviewed elsewhere [4]. A closely related approach using projectors will be shortly discussed in Section 8.7.

3. FENE chain in dilute solution including hydrodynamic interactions

Various experimental observations reveal an important aspect of the behavior of polymer solutions which is not captured by FENE dumbbell models. When the experimental data for high molecular weight systems is plotted in terms of appropriately normalized coordinates, the most noticeable feature is the exhibition of universal behavior. By this it is meant that curves for different values of a parameter, such as the molecular weight, the temperature, or even for different types of monomers can be superposed onto a single curve. For example, when the reduced intrinsic viscosity is plotted as a function of the reduced shear rate, the curves for polystyrene in different types of good solvents at various temperatures collapse onto a single curve [6]. There is, however, an important point that must be noted. While polymers dissolved in both theta solvents and good solvents show universal behavior, the universal behavior is different in the two cases. An example of this is the observed scaling behavior of various quantities with molecular weight. The scaling is universal within the context of a particular type of solvent. The term universality class is used to describe the set of

systems that exhibit common universal behavior [101]. Thus theta and good solvents belong to different universality classes.

As pointed out in 1948 [102], the perturbation of the solvent flow field induced by suspended spherical particles ('beads') leads to an additional interaction between beads, the so-called HI. Incorporation of this effect into the classical Rouse model for dilute polymer solutions makes the resulting model equations—containing a HI matrix—nonlinear. Predictions for some material properties were found to become much more realistic when HI is accounted for [6,68,72,73,15,103,104]. In the usual discussion of HI, one linearizes the Navier–Stokes equation (NSE) and assumes that the propagation of solvent flow perturbations is infinitely fast. If the beads are point particles one obtains for the perturbation of the flow at position $\boldsymbol{r}$: $\Delta\boldsymbol{v}(\boldsymbol{r}) = \boldsymbol{\Omega}(\boldsymbol{r}-\boldsymbol{r}')\cdot\boldsymbol{F}(\boldsymbol{r}')$, where $\boldsymbol{F}(\boldsymbol{r}')$ is the force exerted by a bead at point $\boldsymbol{r}'$ on the solvent, and $\boldsymbol{\Omega}(\boldsymbol{r})$ is the Green's function of the time-dependent linearized NSE, known as Oseen–Burgers tensor (one has to require $\boldsymbol{\Omega}(\boldsymbol{0}) = \boldsymbol{0}$ in order to avoid hydrodynamic self-interactions).

There appear to be two routes by which the universal predictions of models with HI have been obtained so far, namely, by extrapolating finite chain length results to the limit of infinite chain length where the model predictions become parameter free, and by using renormalization group theory methods. In the former method, there are two essential requirements. The first is that rheological data for finite chains must be generated for large enough values of N so as to be able to extrapolate reliably, i.e., with small enough error, to the limit $N \to \infty$. The second is that some knowledge of the leading order corrections to the infinite chain length limit must be obtained in order to carry out the extrapolation in an efficient manner. It is possible to obtain universal ratios in the zero shear rate limit in all the cases [68].

The diffusion equation, sometimes referred to as FP equation, for the configurational distribution function $\psi(t,\boldsymbol{r}_1,\boldsymbol{r}_2,\ldots,\boldsymbol{r}_N)$ for a chain with N beads reads [105,68] subject to homogeneous flows ($\boldsymbol{\kappa}$ was defined in Section 2)

$$\frac{\partial\psi}{\partial t} = -\sum_{i=1}^{N}\frac{\partial}{\partial\boldsymbol{r}_i}\cdot\left(\boldsymbol{\kappa}\cdot\boldsymbol{r}_i + \frac{1}{\zeta}\sum_j \boldsymbol{H}_{ij}\cdot\boldsymbol{F}_j\right)\psi + \frac{k_BT}{\zeta}\sum_{i,j}\frac{\partial}{\partial\boldsymbol{r}_i}\cdot\boldsymbol{H}_{ij}\cdot\frac{\partial}{\partial\boldsymbol{r}_j}\psi \tag{15}$$

with the HI matrix $\boldsymbol{H}_{ij} \equiv \boldsymbol{H}(\boldsymbol{r}_{ij}) = \delta_{ij}\boldsymbol{1} + \zeta\,\boldsymbol{\Omega}(\boldsymbol{r}_{ij})$. In the Itô approach, the stochastic differential (Langevin) equations of motions for bead positions equivalent to the FP equation (15) are

$$d\boldsymbol{r}_i = \left(\boldsymbol{\kappa}\cdot\boldsymbol{r}_i + \frac{1}{\zeta}\sum_{j}^{N}\boldsymbol{H}_{ij}\cdot\boldsymbol{F}_j\right)\mathrm{d}t + \sqrt{\frac{2k_BT}{\zeta}}\,\mathrm{d}\boldsymbol{S}_i\ , \tag{16}$$

where $\mathrm{d}\boldsymbol{S}_i \equiv \sum_j \boldsymbol{B}_{ij}\cdot\mathrm{d}\boldsymbol{W}_j(t)$; $\boldsymbol{W}$ denotes a Wiener process (Gaussian white noise vector); $\boldsymbol{B}$ is related to the HI matrix through the fluctuation–dissipation theorem $\boldsymbol{H}_{ij} = \sum_k^N \boldsymbol{B}_{ik}\cdot\boldsymbol{B}_{jk}^{\mathrm{T}}$ and $\boldsymbol{F}_j$ denotes the sum of (other than HI, i.e. spring) forces on bead j. Eq. (16) is the starting point for a NEBD computer simulation, the only tool available for treating chains with HI rigorously. There are two possibilities for restoring a positive-semidefinite diffusion term when the assumption of point particles fails (one implicitly introduces a bead radius through Stokes monomer friction coefficient ζ): one can prevent the beads from overlapping, or one can modify the Oseen–Burgers HI tensor. In the following application we will use $\boldsymbol{\Omega}$ according to the regularization proposed by Rotne et al. [106]. The Langevin equation (16) cannot be solved in closed form. In order to obtain a tractable

form, in 1956 Zimm replaced the random variables $\boldsymbol{\Omega}_{\boldsymbol{r}_{ij}}$ by their equilibrium (isotropic) averages, i.e., $\boldsymbol{H}_{ij} \to H_{ij}\mathbf{1}$ with the $N \times N$ matrix $H_{ij} = \delta_{ij} + h^*(1-\delta_{ij})(2/|i-j|)^{1/2}$ and a HI parameter [107]

$$h^* \equiv \frac{\zeta}{6\pi\eta_s}\sqrt{\frac{H}{\pi k_B T}}\ , \tag{17}$$

where H denotes the harmonic bead–spring coefficient. The parameter h^* can be expressed as $h^* = a_b/(\pi k_B T/H)^{1/2}$ which is roughly the bead radius a_b over the root-mean-square distance between two beads connected by a spring at equilibrium, hence $0 < h^* < 1/2$. For analytical and experimental estimates of h^* see [105,108,6]. For the Zimm model $h^* = 1/4$ minimizes the effect of chain length and the very short and long chain limits can be elaborated analytically.

3.1. Long chain limit, Cholesky decomposition

For several reasons, the long chain limit is important. It is independent of the details of the mechanical model, and hence is a general consequence of the presence of HI and equilibrium averaged HI for the Zimm model [68], respectively. For long chains it should be observed that h^* occurs only in the combination ζ/h^* in all material properties. Therefore, the parameter h^* has no observable effect on the material properties of long chains. Power law dependences of various material properties on molecular weight $M \propto N$ with universal exponents are expected (see Section 8.2.2.1 of [109]) and, from the prefactors, one can form universal ratios [68]. The universal exponents and prefactors are ideally suited for a parameter-free test of the model by means of experimental data for high molecular weight polymer solutions. We obtained estimates by extrapolation from extensive and efficient simulation.

3.2. NEBD simulation details

A coarse-grained molecular model represents the polymer molecules: the FENE bead–spring chain model, i.e., N identical beads joined by $N-1$ (anharmonic) springs. The solvent is modeled as an incompressible, isothermal Newtonian homogeneous fluid characterized by its viscosity η_s. The solution is considered to be infinitely diluted, and the problem is limited to the behavior of one single molecule. In combination with the variance reduction scheme, chain lengths comparable to real conditions (e.g., $N = 300$, cf. Section 4) are now coming within reach of simulations.

The decomposition of the diffusion matrix $\boldsymbol{H}$ to obtain a representation for $\boldsymbol{B}$ (e.g., Cholesky decomposition) for long chains is expensive and scales with N^3. A highly efficient method [110] is based on an approximation of the square root function in Chebyshev (tensor) polynomials $\boldsymbol{T}_k$ of the first kind, following the notation in [111],

$$\boldsymbol{B} = \sqrt{\boldsymbol{H}} \approx \sum_{k=1}^{L} c_k \boldsymbol{T}_{k-1}(\boldsymbol{H}) - \frac{\mathbf{1}}{2}c_1\ , \tag{18}$$

where the recursive formula

$$\boldsymbol{T}_{k+1}(\boldsymbol{H}) = 2\,\boldsymbol{H}\cdot\boldsymbol{T}_k(\boldsymbol{H}) - \boldsymbol{T}_{k-1}(\boldsymbol{H})\ , \tag{19}$$

together with $\boldsymbol{T}_0(\boldsymbol{H})=\mathbf{1}$ and $\boldsymbol{T}_1(\boldsymbol{H})=\boldsymbol{H}$ define these polynomials. For a fixed L, (18) is a polynomial in $\boldsymbol{H}$ which approximates $\boldsymbol{B}$ in the interval $[-1,1]$ (concerning the eigenvalues of $\boldsymbol{H}$), where all

the zeros of $\boldsymbol{T}_k$ are located. The sum can be truncated in a very graceful way, one that does yield the 'most accurate' approximation of degree L (in a sense which can be made precise). The convergence of the Chebyshev polynomial approximation requires that the eigenvalues of the matrix $\boldsymbol{H}$ are within the interval $[-1,1]$. Actually, this is not the case, and one introduces shift coefficients, h_a and h_b in order to apply the recursion formula to the 'shifted' matrix $\boldsymbol{H}' \equiv h_a\boldsymbol{H} + h_b\boldsymbol{1}$ whose eigenvalues should be within the desired range. This requirement is fulfilled for $h_a = 2/(\Lambda_M - \Lambda_0)$, $2\,h_b = -h_a(\Lambda_M + \Lambda_0)$, where Λ_0 and Λ_M denote the minimum and maximum eigenvalues of the original HI matrix $\boldsymbol{H}$, respectively [104]. The coefficients of the series are readily obtained by standard methods [112,111]: $c_j = L^{-1}\sum_{k=1}^{L}\alpha_{kj}^{L}\,(b_+ + b_-\cos[\pi(k-1/2)/L])^{1/2}$, with coefficients $b_+ \equiv (h_a + h_b)/2$, $b_- \equiv (h_b - h_a)/2$, and the abbreviation $\alpha_{kj}^{L} \equiv 2\cos[\pi(j-1)(k-1/2)/L]$. Instead of calculating the square root matrix first, thus implying several time consuming matrix by matrix products for the evaluation of the polynomials of the series, and afterwards its product with the random $\boldsymbol{W}$ vector, the desired vector is obtained directly as a result of a series of different vectors $\boldsymbol{V}$, recursively calculated only through less expensive matrix ($\boldsymbol{H}$) by vector ($\boldsymbol{V}$) products, i.e., one replaces $\mathrm{d}\boldsymbol{S}_i$ in Eq. (16) by $\mathrm{d}\boldsymbol{S}_i = (\sum_k^L c_k\boldsymbol{T}_{k-1}(\boldsymbol{H}') - \boldsymbol{1}\tilde{c}_1)\cdot\mathrm{d}\boldsymbol{W}_j(t) = \sum_k^L c_k\,\mathrm{d}\boldsymbol{V}_{k-1}^i - \tilde{c}_1\,\mathrm{d}\boldsymbol{W}_j$. with $\tilde{c}_1 = c_1/2$. The recursion formula for $\mathrm{d}\boldsymbol{V}_k^i \equiv \boldsymbol{T}_k(\boldsymbol{H}')\cdot\mathrm{d}\boldsymbol{W}_i$ is immediately obtained from (19). Its evaluation requires an effort $\propto N^2$ for every $k = 1,2,\ldots,L$. The overall computational demand of the method we use scales with $N^2L \propto N^{9/4}$ per time step as shown in [104]. The eigenvalue range applied in the implementation of this idea is specific for the problem under study. In general, one has to ensure that the degree of violation of the fluctuation–dissipation theorem (with respect to an eligible matrix norm) is small enough to obtain exact moments of the distribution function with a desired accuracy, e.g., along the lines indicated in [113], in order to prevent a direct calculation of eigenvalues. There is an increasing interest in using iterative schemes to decompose the HI matrix, e.g. [113–117,73,118–124,110].

In addition to this decomposition method a variance reduction simulation technique has been implemented in [104] to reduce the statistical error bars (see also Ref. [68, p. 177]). For this purpose two simulations are run in parallel, one at equilibrium, and another undergoing steady shear flow but using the same sequence of random numbers. After a certain time interval the desired magnitudes are sampled, and the chain simulated under steady shear flow is (periodically) reset to the state of the chain in equilibrium. Simulations for this model have been further performed, e.g., for the case of step shear deformation in [125]. The Cholesky decomposition has been recently applied within an accelerated Stokesian dynamics algorithm for Brownian suspensions [126] and for simulations of supercooled DNA [127].

3.3. Universal ratios

The most interesting theoretical predictions for experimentally accessible quantities are those which are independent of any physical parameters. In the limit of infinitely long chains the Zimm model predicts a diffusion coefficient $\lim_{N\to\infty} D_h = ch^*k_BT/(\zeta\sqrt{N})$, radius of gyration $\lim_{N\to\infty} R_g = (Nk_BT/2H)^{1/2}$, and spectrum of relaxation times $\lim_{N\to\infty}\lambda_j^{\mathrm{Zimm}} = c_j(N/j)^{2/3}\zeta/(4h^*H\pi^2)$ with $c_1 = 1.22$ and $c_j = 2\pi j/(2\pi j - 1)$ for $j > 1$ [138].

Having established these relationships for the Zimm model one can construct and define a number of universal ratios for experimentally accessible quantities. The universal quantity $U_{\mathrm{RD}} \equiv R_g/R_h = 6\pi\eta_s D_h R_g/(k_BT)$ is the ratio between radius of gyration and hydrodynamic radius, the latter quantity

Table 2
Analytical, experimental and numerical results for the zero shear rate limit. E.g., Fixman estimated $U_{\mathrm{RD}} = 1.42$ [134] but could not estimate $U_{\eta\mathrm{R}}$ due to the slow convergence of rheological properties η (and also $\Psi_{1,2}$)

	U_{RD}	$U_{\eta\mathrm{R}}$	$U_{\Psi\eta}$	$U_{\Psi\Psi}$	$U_{\eta\lambda}$	$U_{\Psi S}$
Theory						
Rouse [68]	$\propto N^{-1/2}$	$\propto N^{+1/2}$	0.8	0	1.645	$\propto N$
Zimm [68]	1.47934	1.66425	0.413865	0	2.39	20.1128
Consist. average [105]		1.66425	0.413865	0.010628		
Gaussian approx. [128]	—	1.213(3)	0.560(3)	−0.0226(5)	1.835(1)	14.46(1)
Twofold normal Zimm [128]	—	1.210(2)	0.5615(3)	−0.0232(1)	1.835(1)	14.42(1)
Renormalization [108]	—	1.377(1)	0.6096(1)	−0.0130(1)	—	20.29(1)
Oono et al.* [129]	1.56(1)	—	—	—	—	—
Öttinger* [130]	—	—	0.6288(1)	—	—	10.46(1)
Experiment						
Schmidt et al. [131,132]	1.27(6)	—	—	—	—	—
Miyaki et al. [133]	—	1.49(6)	—	—	—	—
Bossart et al. [71]	—	—	0.64(9)	—	—	—
Bossart et al.* [71]	—	—	0.535(40)	—	—	—
Simulation						
Fixman [134] (NEBD)	1.42(8)	—	—	—	—	—
de la Torre et al. [135] (NEBD)	1.28(11)	1.47(15)	—	—	2.0	—
Rubio et al. [136] (MC)	—	$> 1.36(5)$	—	—	—	—
Garcia Bernal et al.* [137] (NEBD)	1.48(15)	1.11(10)		—	—	—
Aust et al.* (NEMD) [56]	1.41(6)	—	—	—	—	—
Kröger et al. (NEBD) [104]	1.33(4)	1.55(6)	0.45(7)	0.05(4)	—	19(2)

The asterisk marks results obtained taking into account excluded volume. The estimates of de la Torre et al. and Bernal et al. [135,137,117] were obtained by extrapolation from their results for $h^* = 1/4$ [104].

can be actually measured experimentally in a dynamic experiment, e.g., by observing the relaxation time of the dynamic scattering function $S(q,t)$ for small momentum transfers $qR_g \ll 1$. The universal ratio $U_{\eta\mathrm{R}} \equiv \lim_{c\to 0} \eta_p/(c\eta_s(4\pi R_g^3/3))$ is a measure for the specific polymer contribution η_p to the reduced shear viscosity, $U_{\Psi\eta} \equiv \lim_{c\to 0} ck_BT\Psi_1/(\eta_p^2)$ gives the ratio between first viscometric function and squared polymer contribution to the shear viscosity, $U_{\Psi\Psi} \equiv \Psi_2/\Psi_1$ is the ratio between the second and first viscometric function, $U_{\eta\lambda} \equiv \lim_{c\to 0} \eta_p/(ck_BT\lambda_1)$ reflects the proportionality between η_p and the longest relaxation time, and $U_{\Psi S} \equiv k_BT\Psi_1/(c\eta_s^2 R_g^6)$ (also introduced in [68]) is just a combination of two of the above universal ratios. For the Zimm model one infers $U_{\eta\lambda}$ from $\eta_p/ck_BT = \sum_j \lambda_j$. From these ratios one can, for example, eliminate the unspecified proportionality coefficients in the 'blob' theory of polymer statistics [139,140].

Universal ratios are collected in Table 2. It contains results for diverse theoretical approaches such as obtained by the Zimm model, the Gaussian approximation, a consistent averaging procedure, and renormalization group calculations, together with experimental and numerical findings. The estimates for the exact long-chain limit are extrapolated from NEBD data, where the polymer contribution to the stress tensor and radius of gyration needed to analyze universal ratios are calculated directly

from bead trajectories. In particular, the monomer diffusion coefficient D and radius of gyration R_g are sampled from bead trajectories $\{\boldsymbol{r}_i(t)\}$ according to $D = \lim_{t\to\infty} (\sum_{i=1}^{N} [\boldsymbol{r}_i(t) - \boldsymbol{r}_i(0)]^2)/(6Nt)$ and $R_g^2 = \sum_i [\boldsymbol{r}_i - \boldsymbol{r}_c]^2/N$, respectively, where $\boldsymbol{r}_c$ denotes the center of mass of the molecule. The simulation reveals that the power law regime for monomer diffusion D will be obtained earlier than the one for the more 'global' R_g. By analogy to classical results for the diffusion of a sphere embedded in a Newtonian liquid the hydrodynamic radius (of the corresponding sphere) is defined by $R_h = k_B T/(6\pi\eta_s D)$. An independent discussion about relaxation times for this system, needed to determine $U_{\eta\lambda}$ can be found in [135]. As for the Zimm model, simulation results reveal that the radius of gyration converges more fast to its long chain limit than the hydrodynamic radius. In Ref. [105] the leading corrections to the limit of infinitely long chains have been estimated in the framework of a generalized Zimm model for dilute polymer solutions. They are of the following form:

$$U_i(h^*, N) = \tilde{U}_i + \frac{c_i}{\sqrt{N}} \left(\frac{1}{h_i^*} - \frac{1}{h^*} \right) , \tag{20}$$

for $i \in \{\mathrm{RD}, \eta\mathrm{R}, \mathrm{etc.}\}$. A careful analysis of the simulation data (last row of Table 2) yields the following results for the coefficients defined through (20):

$$\begin{aligned}
&\tilde{U}_{\mathrm{RD}} = 1.33 \pm 0.05, \quad c_{\mathrm{RD}} = -0.49, \quad h^*_{\mathrm{RD}} = 0.267 , \\
&\tilde{U}_{\eta\mathrm{R}} = 1.55 \pm 0.04, \quad c_{\eta\mathrm{R}} = 1.9, \quad h^*_{\eta\mathrm{R}} = 0.250 , \\
&\tilde{U}_{\Psi_\eta} = 0.29 \pm 0.1, \quad c_{\Psi_\eta} = -0.20, \quad h^*_{\Psi_\eta} = 0.261 , \\
&\tilde{U}_{\Psi\Psi} = 0.05 \pm 0.1, \quad c_{\Psi\Psi} = 0.05, \quad h^*_{\Psi\Psi} = 0.247 .
\end{aligned} \tag{21}$$

As expected from [105] the values h_i^* for which the leading order corrections are absent do not coincide for the various functions U_i. Since functions (20) for a given i and different HI parameters appear as a set of converging straight lines in the representations of raw data in Figs. 10 and 11 it is obvious, that the data for U_{RD} is represented better by the expression (20) than the data for the remaining universal ratios.

4. FENE chains in melts

A dense collection of repulsive FENE chains serves as a suitable microscopic model for both entangled and unentangled polymer melts. We will consider once more linear and monodisperse chains although FENE models are immediately applicable to polydisperse polymers with arbitrary architectures. Besides its success for the study of polymer melts at equilibrium [141–143,15], the nonlinear viscoelastic and structural properties of FENE chain models such as viscosities and scattering patterns are in accordance with experimental results for shear- and elongational flows [19,144–147,20]. Due to the computational demands caused by the strong increase of relaxation time with molecular weight (M) only recently it has been observed, that the basic model also exhibits the experimentally observed rheological crossover, certainly related to the ability of polymers to form knots (topological constraints) between macromolecules which is further discussed in [7,148–155]. The crossover manifests itself in a change of power law for the zero shear viscosity at a certain M.

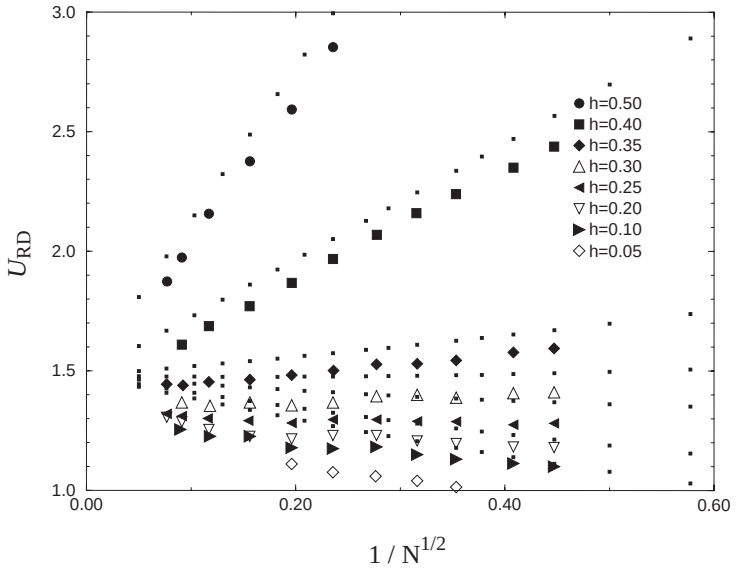

Fig. 10. The ratio U_{RD} between gyration and hydrodynamic radii vs the inverse square root of chain length for different values of the HI interaction parameter h^*. As a reference, results for the Zimm model also shown (small dots). By extrapolation to $N \to \infty$ the universal ratio is obtained (see Table 2). Apparently, U_{RD} depends linearly on $1\sqrt{N}$ [104].

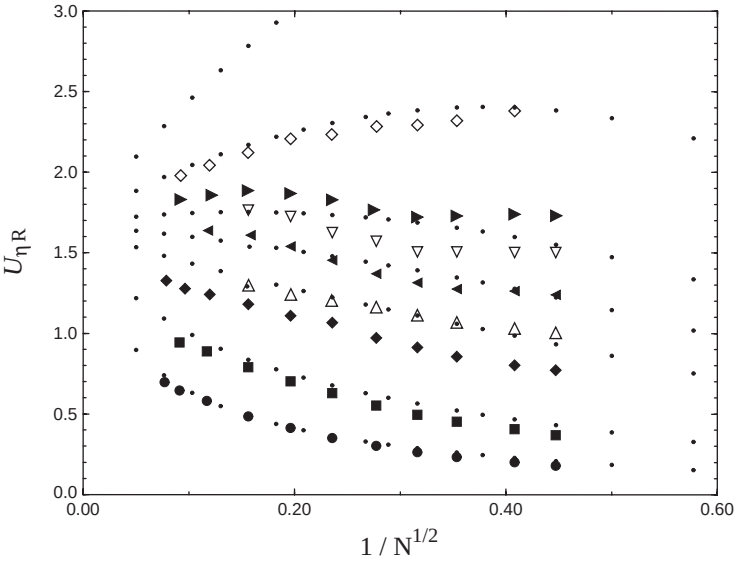

Fig. 11. The ratio U_{Ψ_η}, cf. Fig. 10 [104].

For FENE melts, FENE forces of the type (1) act between all adjacent beads (next neighbors) within chains, and the repulsive part of the radially symmetric Lennard-Jones (LJ) potential (often called WCA potential, introduced by Weeks et al. [156]) is added between ALL pairs of

beads—within cutoff distance—in order to model excluded volume,

$$\boldsymbol{F}^{(\mathrm{WCA})}(\boldsymbol{r}) = \epsilon \boldsymbol{F}^{(\mathrm{WCA})*}(\boldsymbol{r}/\sigma),$$

$$\boldsymbol{F}^{(\mathrm{WCA})*}(\boldsymbol{r}) = -\nabla_r 4(r^{-12} - r^{-6} + 1/4) = -24\left(\frac{r^6 - 2}{r^{12}}\right)\frac{\boldsymbol{r}}{r^2}, \quad r \leqslant 2^{1/6} \tag{22}$$

and $\boldsymbol{F}^{(\mathrm{WCA})*}$ $(r \geqslant 2^{1/6}) = 0$ where r denotes the distance between two interacting beads. Here and in the following all dimensionless quantities which are reduced to the usual LJ-units of [157–159] are denoted by an asterisk *only if* otherwise ambiguities could arise. We refer to Ref. [160] for the discussion of an alternative short range potential, and to Section 4.3 for the reduced units appearing in Eq. (22).

4.1. NEMD simulation method

The total radially symmetric force $\boldsymbol{F}$ between pairs of beads for the FENE multichain system is $\boldsymbol{F} = \boldsymbol{F}^{(\mathrm{WCA})} + \boldsymbol{F}^{(\mathrm{FENE})}$ and $\boldsymbol{F} = \boldsymbol{F}^{(\mathrm{WCA})}$ for adjacent and non-adjacent beads, respectively. As in [141,142,19] for melts the FENE spring coefficients $H = 30$ and $Q_0 = 1.5$ (at temperature $T = 1$, LJ units) chosen strong enough to make bond crossings energetically infeasible and small enough to choose a reasonable integration time step during the NEMD simulation, which integrates Newton's equation of motion for this system via a velocity Verlet algorithm (conc. the application reviewed in this section). The simulated systems presented in the next section consist of 3×10^5 beads arranged in chains with $N = 4$–400 beads each. A stationary, planar Couette flow in x-direction (gradient in y-direction) with shear rate $\dot{\gamma}$ will be imposed [19]. Neighbor lists, Lees–Edwards boundary conditions [157], and layered link cells [161] are used to optimize the computer routines, In contrast to the standard procedure for equilibrium simulations we update the list of pair dependencies on an upper limit for the increase of the relative separation of these pairs, not on the absolute motion of individual particles. Temperature is kept constant by rescaling the magnitude of the peculiar particle velocities which corresponds to the Gaussian constraint of constant kinetic energy [159] for small integration time steps. Alternative constraint mechanisms (configurational, Nose–Hoover thermostats, etc.) have been extensively discussed elsewhere, and are still under discussion. Since simulation runs are CPU time consuming it should be mentioned that the generation of well quasiequilibrated dense samples for simulations is of particular relevance. Several codes have been developed which attempt to reach pre-equilibration (at given density) using Monte Carlo, tree-based, fuzzy logic, neural network strategies, to mention a few. The NEMD simulation method is—in principle—independent of the choice for a particular FENE model. Some of the codes are also available in the literature [34,162], or can be obtained from the author.

4.2. Stress tensor

The stress tensor $\boldsymbol{\sigma}$ (equals the negative friction pressure tensor), a sum of kinetic and potential parts, is calculated from its tensorial virial expression

$$\boldsymbol{\sigma} = -\frac{1}{V}\left\langle \sum_{i=1}^{N_b} \boldsymbol{c}^{(i)}\boldsymbol{c}^{(i)} + \frac{1}{2}\sum_{i=1}^{N_b}\sum_{j=1}^{N_b} \boldsymbol{r}^{(ij)}\,\boldsymbol{F}(\boldsymbol{r}^{(ij)}) \right\rangle , \tag{23}$$

where V is the volume of the simulation cell, N_b is the total number of beads, $\boldsymbol{r}^{(i)}$ and $\boldsymbol{c}^{(i)}$ are the spatial coordinate and the peculiar velocity of bead i within a polymer chain, respectively, $\boldsymbol{r}^{(ij)} \equiv \boldsymbol{r}^{(i)} - \boldsymbol{r}^{(j)}$, and $\boldsymbol{F}$ is the pair force. The stress tensor is accessible as time average from the calculated bead trajectories. For dense fluids, the main contribution to the rheological properties stems from the potential part of the stress tensor, except for the case of highly aligned samples. Material function such as viscosities and shear moduli are defined in terms of the stress tensor and flow parameters [6]. The official nomenclature is periodically published by the Journal of Rheology.

4.3. Lennard-Jones (LJ) units

For any measurable quantity A with dimension $\mathrm{kg}^{\alpha}\,\mathrm{m}^{\beta}\,\mathrm{s}^{\gamma}$ one has $A = A_{\mathrm{dimless}} A_{\mathrm{ref}}$ and $A_{\mathrm{ref}} = m^{\alpha+\gamma/2} r_0^{\beta+\gamma} \epsilon^{-\gamma/2}$, where σ, ϵ provide the length and energy scales via the LJ potential and the monomeric mass m via Newton's equations of motion. Specifically, the reference quantities for density, temperature, time and viscosity are $n_{\mathrm{ref}} = \sigma^{-3}$, $T_{\mathrm{ref}} = \epsilon/k_B$, $t_{\mathrm{ref}} = \sigma\sqrt{m\epsilon}$, $\eta_{\mathrm{ref}} = \sigma^{-2}\sqrt{m\epsilon}$. We therefore have to deal exclusively with $\epsilon = \sigma = 1$ in (22). See Section 4.7 for a comment on how to interpret dimensionless simulation numbers.

4.4. Flow curve and dynamical crossover

For the FENE chain melt, rheological properties were extracted for various shear rates over eight decades from $\dot{\gamma} = 10^{-8}$ to $\dot{\gamma} = 1$ for $N = 4$–400 [163,144]. For the short chains ($N < 20$) a weak shear dilatancy is detected. With increasing shear rate the trace of the pressure tensor decreases due to the intramolecular bond stretching. The non-Newtonian viscosity $\eta \equiv \sigma_{xy}/\dot{\gamma}$ is shown for different chain lengths and rates in Fig. 12. The FENE chain melt is shear thinning, and approaches a power law curve $\eta \propto \dot{\gamma}^{-\alpha}$ independent of M with the exponent $\alpha = 0.5 \pm 0.2$. From the non-Newtonian viscosity η in Fig. 12 the zero rate viscosity η_0 [6] can be estimated. This quantity clearly exhibits a crossover from a Rouse-type regime $\eta_0 \propto N^1$ to $\eta_0 \propto N^{\nu \geqslant 3}$ (inset of Fig. 12) It is well represented by the expression $\eta_0 = 0.7\,N(1 + Z^{\nu-1})$ with a number of 'rheologically relevant' entanglements per chain $Z \equiv N/N_c$ and exponent $\nu = 3.3 \pm 0.2$. The zero rate first viscometric function $\Psi_1 \propto (\sigma_{yy} - \sigma_{xx})/\dot{\gamma}^2$ [6] is found to exhibit a crossover at the same critical chain length.

Elliptical contours in the structure factor of single chains and their rotation against flow gradient direction have been analyzed and plotted against wave number in order to visualize the (different) degree of orientation on different length scales inside a polymer during shear flow, see also Fig. 13 for a schematic drawing.

4.5. Characteristic lengths and times

For the characteristic relaxation times τ_N defined from the onset of shear thinning at shear rate $\dot{\gamma} = \dot{\gamma}_N \equiv 1/\tau_N$ we obtain from the NEMD simulations: $\tau_N \propto N^{\approx 2}$ for short chains, in accordance with the Rouse model predictions. Based on careful measurements of monomer diffusion coefficients and further properties for the FENE chain melt obtained from MD simulations [141,142] with up to $N = 400$ beads per chain a 'dynamical' crossover has been observed. A characteristic length was found which marks the crossover between 'Rouse' to 'reptation' diffusion regimes, for which the diffusion coefficients ideally scale as $D \propto 1/N$ and $D \propto 1/N^2$, respectively. The plateau modulus G_N^0,

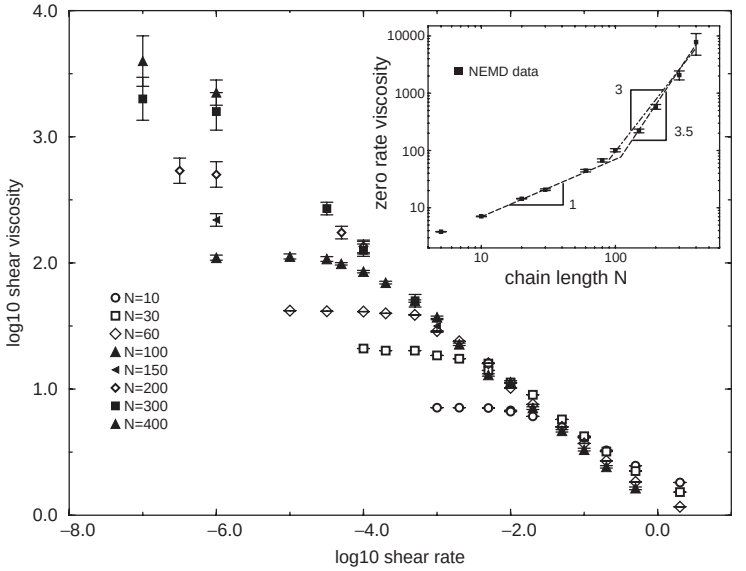

Fig. 12. Non-Newtonian shear viscosity η of the FENE model vs shear $\dot{\gamma}$ (LJ units) for different chain lengths N. Inset: Zero rate shear viscosity η_0 vs chain length. Adapted from Ref. [163].

from which the entanglement M_e can be rigorously deduced [165] has been reported for the FENE chain melt in Ref. [166] for chains up to $N = 10^4$ from the shear stress plateau during relaxation after step strain. The reported value for N_e is about a factor 2.3 larger than the one reported for the dynamical crossover in [141], and thus rather close to the critical weight $N_c = 100 \pm 10$ obtained via NEMD in [163].

The commonly experimentally accessible quantities characterizing a polymer melt at certain temperature are its monomer density ρ, average M, monomer mass m, squared end-to-end distance per monomer $b^2 \equiv \langle R^2/N \rangle$, the critical and entanglement weights, $M_c = mN_c$ and $M_e = mN_e$, respectively, and the Kuhn length b_K. These quantities are related to the bond length $b_0 = b^2/b_K$, the characteristic ratio $C_\infty = b_K/b_0$, and the so-called tube diameter $d_T = b\sqrt{N_e}$. It has been suggested recently [167] that both N_e and N_c can be calculated from ρ, b^2 and a fixed length $p \approx 10^{-9}$ m. In order to compare with the simulation results one has to rewrite this finding in dimensionless form, which is actually only possible for N_e and then states: $N_e \propto \rho p^3$ with a packing length $p \equiv 1/[\rho \langle R^2/M \rangle] = 1/(nb^2)$. This definition is rewritten as (compare second last column of Table 3)

$$N_e \propto C_\infty (p/b_K)^2 = [1/(nb^3)]^2 \ , \tag{24}$$

or $nd_T b^2 = c_e$ with a proportionality coefficient $c_e = 21 \pm 2$, where n denotes monomer number density.

A corresponding relationship for M_c was also proposed [163] (compare last column of Table 3)

$$N_c \propto C_\infty^{3/2} (p/b_K) = 1/(nb_0^2 b) \ , \tag{25}$$

in agreement with the simulation data, and a proportionality coefficient of about $c_e^2/5$ such that $C_\infty \sqrt{N_e} \approx 4N_c$. Thus, one is led to the prediction $N_e n b_0^3 > N_c$ for very flexible chains with

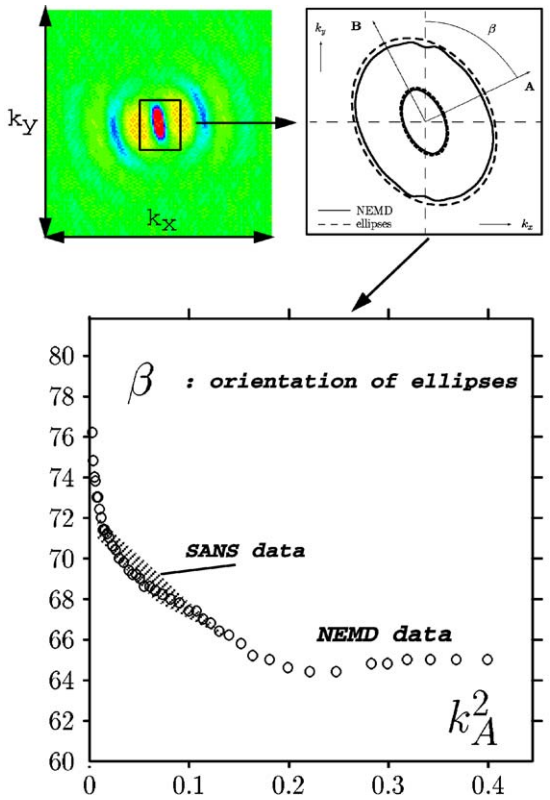

Fig. 13. Differences between local and global order of polymeric FENE chains under shear flow conditions are revealed via the NEMD structure factor of single chains, (top left) Structure factor extracted by NEMD, projected to shear plane, (top right) Contour fit allows to extract the half axes (half wave numbers) of ellipses and the rotation angle β. (bottom) Rotation angle vs wave number. Experimental results by [164] serve as a reference.

$C_\infty < 1.9$. Predictions are summarized in Fig. 14. The possibility for the existence of materials with $N_c < N_e$ has been proposed earlier by Fetters et al. [167]. Statement (25) has the advantage upon the one in [167] that it exclusively contains dimensionless quantities, and thus allows for a verification by computer simulation. Eqs. (24), (25) imply, that N_c is inversely proportional to the number of monomers in the volume bb_0^2, whereas $\sqrt{N_e}$ is inversely proportional to the number of monomers in the volume b^3. Under equilibrium conditions the simulated FENE chains exhibit an average bond length $b_0 = 0.97$, $b = 1.34b_0$, hence $C_\infty = b^2/b_0^2 = 1.79$ and $p/b_K = 0.404$. Relationship (24) predicts a simulation value $N_e \approx 120$ which is slightly above the one reported for N_c, a factor of 3–4 above the one reported for a dynamical crossover in [141,142], and just by a factor of 1.5 above the one reported from direct measurements of the relaxation modulus [166] (Fig. 15).

The reported findings underline the relevance of the FENE model in predicting static, dynamic and flow behaviors of real polymers for arbitrary weights. Beside the investigation of rheological behaviors of FENE melts the simulation of bead trajectories allows to analyze, for example, the degree of flow-induced orientation of chain segments, the validity of the so-called ‘stress-optic rule’,

Table 3
The table contains representative experimental data and the simulation data (FENE model) in dimensionless form

Polymer	T	ρ	b_0 [Å]	d_T [Å]	C_∞	$\frac{N_c}{100}$	$pn^{1/3}$	p/b_K	$\frac{\sqrt{N_e}}{N_c C_\infty}$	$\frac{N_e}{C_\infty}\left(\frac{b_K}{p}\right)^2$	$\frac{N_c}{C_\infty^{3/2}}\left(\frac{b_K}{p}\right)$
PE	443 K	0.78	1.45	40.0	7.6	3.0	0.60	0.17	0.25	453	84
PS	490 K	0.92	1.51	88.6	9.9	7.0	0.92	0.29	0.26	454	81
PαMS	459 K	1.04	1.57	76.7	10.5	6.9	0.80	0.22	0.27	451	85
PIB	490 K	0.82	1.62	73.4	5.8	6.1	0.97	0.40	0.18	384	109
PDMS	298 K	0.97	1.70	74.6	6.0	6.6	0.92	0.36	0.17	417	119
FENE	ϵ/k_B	$0.84\frac{m}{\sigma^3}$	0.97σ	$1.3\sigma\sqrt{N_e}$	1.79	1	0.66	0.40	$0.018\sqrt{N_e}$	$3.4\ N_e$	103

All experimental quantities listed are obtained from literature data for (i) the ratio between squared end-to-end distance and M, (ii) the mass of a repeating unit m, (iii) the critical (from shear flow) and entanglement weights (from plateau modulus), and (iv) bond length b_0 (or C_∞) at temperature T, monomer density ρ (in g/cm^3), monomer number density $n = \rho/m$, packing length p (see text part). The last three columns contain universal numbers, if the proposed scalings (24), (25) are valid.

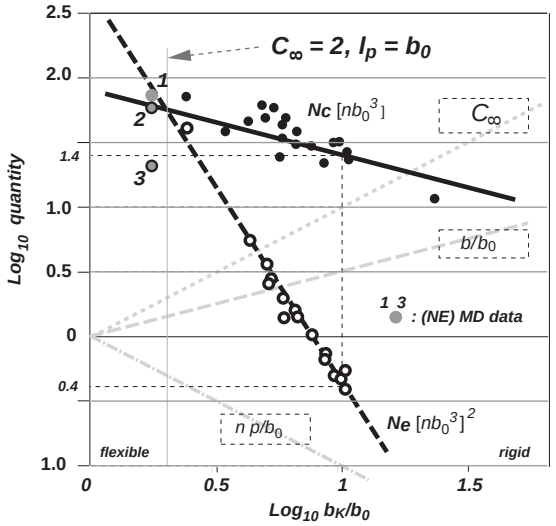

Fig. 14. Scaling behavior of crossover and entanglement molecular weights according to Eqs. (24), (25). The figure contains the predicted behavior (lines) as well as experimental (full symbols) and simulation results (open symbols, symbol 1 for N_c [163], 2 for N_e [166], 3 for N_e [142]).

the degree of entanglement [169] anisotropic tube renewal, and therefore renders possible the test of coarse-grained descriptions in later sections.

4.6. Origin of the stress-optic rule (SOR) and its failures

Shear flow together with elongational flows are essential for the understanding of the flow properties of fluids in complex flows [8,170–172,146,20]. We wish to further demonstrate the impact

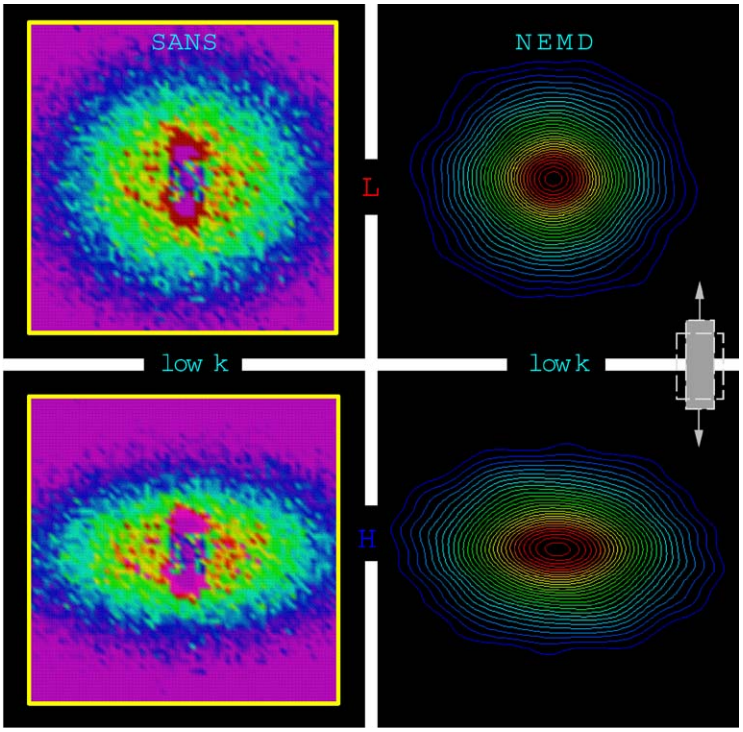

Fig. 15. The single chain structure factor for stretched samples with equal values of flow birefringence for samples fulfilling (bottom) or not (top) the SOR. The figure compares data from SANS experiments (left) [168] and NEMD simulation (right). Due to the fact, that orientational relaxation is fast on a local scale, the overall extension of the polymer has to be much larger for samples fulfilling the SOR, i.e., at high temperatures or low rates, in order to exhibit the same local alignment.

of the FENE chain melt model for the investigation of the microscopic origins of experimentally observable transport and optical phenomena. One of the aspects of practical relevance (in particular for rheooptics) concerns the validity of the stress-optic rule (SOR), a proportionality between stress and alignment tensors, which is fulfilled for polymer melts under 'usual' conditions. Along with the spirit of this review, we focus on studies in the nontrivial regime, where the proportionality is known to be at least partially lost, i.e., at temperatures close to the glass transition temperature T_g or at high elongation rates. To this end we discuss results obtained during constant rate uniaxial elongational flow followed by relaxation after reaching a constant stretching ratio [146]. Experimentally measured rate dependencies of the stress-optical behavior of amorphous polymers undergoing elongational flow at temperatures close above T_g are reported in Fig. 16. For the lowest rates only small deviations from the 'equilibrium curve' have been detected, where the SOR is valid. For the higher elongation rates the curves exhibit a stress overshoot, and a stress offset σ_{off} for which approximate values vs the reduced elongation rate $a_T\dot{\epsilon}$ are given in Fig. 16b. The phenomenological description of the viscoelastic behavior of amorphous polymers in the region where deviations of the SOR appear has been adjusted many times within the last decades, cf. [52,146] and references cited herein.

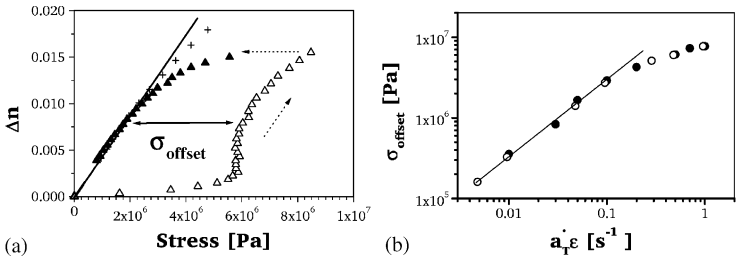

Fig. 16. (Left) Experimental data taken from for birefringence (Δn) vs tensile stress for a commercial polystyrene subjected to uniaxial elongational flow (open symbols, at $T = 102.7°C$, rate $\dot{\epsilon} = 0.2\ s^{-1}$) and subsequent relaxation (filled symbols). The crosses represent the behavior at high temperatures ('equilibrium curve' [164]). A 'stress-offset' and thus a failure of the stress-optic rule is evident and interpreted through NEMD results for FENE chains in the text part. (Right) Corresponding stress offset values vs the reduced elongation rate $\dot{\epsilon} a_T$. Adapted from Ref. [146].

In the NEMD simulation, a time-dependent uniaxial isochoric homogeneous elongational flow in x-direction with elongation rate $\dot{\epsilon} = \partial v_x/\partial x$ is imposed via rescaling of the dimension of the central box [173,20]. Rheological information under uniaxial flow is contained in the 'uniaxial' component of the stress tensor (23) or 'tensile stress': $\sigma \equiv \sigma_{xx} - (\sigma_{yy} + \sigma_{zz})/2$. The (2nd rank) alignment tensor, the anisotropic second moment of the orientation distribution function of segments [6],

$$\boldsymbol{a} \equiv \langle \boldsymbol{uu} \rangle - \frac{1}{3}\boldsymbol{I}\ , \tag{26}$$

is extracted directly as an ensemble average from the dyadic constructed of the normalized segment vectors between beads (adjacent beads accordingly labeled) $\boldsymbol{u}^{(i)} \equiv \boldsymbol{r}^{(i+1)} - \boldsymbol{r}^{(i)}$ tangential to the chains contour. The alignment tensor is considered being proportional to the refractive index tensor of the fluid [174,52] whose relevant information for the case of uniaxial elongational flow in x-direction we denote by $\triangle n \equiv a_{xx} - (a_{yy} + a_{zz})/2$. The stress-alignment diagram, obtained by NEMD in [146] compared very well with the experimental data, cf. Fig. 16a, and thus motivated to investigate microscopic origin of the observed behavior. In particular, results for diverse (intra/intermolecular, kinetic/potential, attractive/repulsive, non/nearest neighbor) contributions to the stress tensor as revealed in Figs. 5 and 6 of Ref. [146] and also results for shear flow [19] imply that the stress tensor $\boldsymbol{\sigma}$ for the FENE chain melts can be written essentially as the superposition of three terms

$$\boldsymbol{\sigma} \approx \boldsymbol{\sigma}_{\text{bonded}} + \underbrace{C^{-1}\boldsymbol{a} + \tilde{\boldsymbol{\sigma}}_{\text{simple}}}_{\boldsymbol{\sigma}_{\text{nonbonded}}}\ , \tag{27}$$

where $\boldsymbol{\sigma}_{\text{bonded}}$ denotes the stress contribution from nearest neighbors within polymer chains (bond pushing/stretching and/or bond orientation), C is the linear stress-optic coefficient for the regime where the SOR is valid, and $\tilde{\boldsymbol{\sigma}}_{\text{simple}}$ is proportional to the stress which is measured for a corresponding simple fluid by removing all bonds (i.e. FENE springs) within the system. A value $C = 0.32$ has been independently confirmed from NEMD simulation on weak shear flow in Refs. [19,146]. See Fig. 17 for a schematic drawing. For 'small' flow rates and/or temperatures large compared with the 'bonded' ('intra', nonsignificant stretch) and 'simple' (proportional to flow rate) contributions become small compared to the SOR contribution such that—according to (27) the validity of the SOR is expected in these regimes. The nonbonded stress hence originates the SOR for the microscopic FENE model.

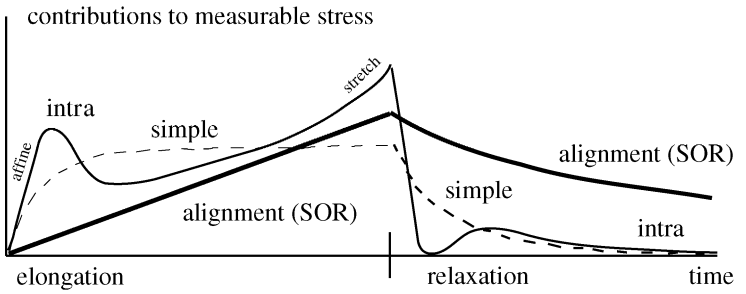

Fig. 17. Schematic drawing clarifying the origin of hysteretic behavior (deviations from the stress-optic rule SOR) in the stress-optic diagram for uniaxial elongational flow of FENE polymer melts according to Ref. [146]. The measured (total, tensile) stress is the sum of bonded (intra) and nonbonded interactions, where the nonbonded interactions appear to carry a part which is proportional to alignment (i.e. fulfilling the SOR) and another one, which is behaving like the one for a corresponding simple 'Newtonian' fluid (FENE bonds removed). The simple and intra stresses become increasingly relevant with decreasing temperature (or increasing rate due to the time temperature superposition principle). The intra-stress dominates if bond stretch (due to finite extensibility of chains) comes into play.

This finding has been further discussed in [145,146]. In this context one should notice, that the splitting (27) is qualitatively different from the one into stresses of predominantly entropy–elastic and energy–elastic origin as discussed in [175,176].

Eq. (27) offers a crude but useful approximation to the stress in polymer melts. It allows to predict rheological properties for the many chain FENE model, based on a single chain model.

In Ref. [146] the degree of stretch and orientation of the polymer chains on different length scales (and 'collective' deformations) have been also measured and analyzed in order to allow for a critical test of alternative pictures which were proposed earlier to describe deviations from the SOR. Upon these models (which have been ruled out) are those which assume stretching of few selected segments, thus leaving the measured anisotropy of chains largely unchanged. Just at a late stage of elongation when segmental stretching leads to a strong increase in σ_{bonded}, local inhomogeneities in bond stretchings/contractions are observed while expression (27) remains valid.

Experimentally, flow induced alignment on different length scales is measured via the single chain structure factor S_{sc} (from deuterated samples, definition provided by Eq. (46)) and flow birefringence or infrared dichroism. While the latter quantities measure the alignment tensor (Eq. (26), probing the anisotropy of segments), at small wave numbers (Guinier regime), S_{sc} resolves the gyration tensor. cf. Figs. 15 for both experimental and FENE chain data for an elongated polymer melt.

4.7. Interpretation of dimensionless simulation numbers

A word of caution concerning the interpretation of dimensionless results is in order. Simulation has to deal with quantities in terms of reference units for mass, length and energy. These have to be obtained by comparing experiment with simulation and provide the basic length (σ) and energy (ϵ) scale of the LJ potential as well as the mass (m) of a bead in solving Newton's equation. Although some freedom exists in how to adjust three dimensionless units, an accepted one is to obtain the reference energy from the measured temperature $\epsilon_{\text{ref}} = Tk_B$, the bead mass from the real N_c divided by the simulated one, and σ^2 from the ratio between measured and simulated end-to-end-distances.

Sample data such as reported in Table 3 motivates obtaining reference units for any simulated quantity for the study of particular materials. For polyethylene (polystyrene), e.g., we deduce a reference length $\sigma = 5.3(9.7)$ Å, a reference mass $m = 42.3(364)$ g/mol, and a reference energy $\epsilon/k_B = 443(490)$ K. From m, σ, ϵ one immediately obtains reference values for any other quantity such as viscosity, time, stress etc. by dimension analysis: $\sqrt{m\epsilon}/\sigma^2 = 0.07(0.07)$ m Pa s, $\sigma\sqrt{m/\epsilon} = 1.8(9) \times 10^{-12}$ s, 40(7.5) MPa, 0.46(0.67) g/cm^3, 553(109) GHz. Corresponding reference values for other polymers are obtained along this procedure. Care has to be taken when predicting quantities which are sensitive to the ratio between the systems longest and shortest relaxation time (τ_{N_c}/τ_1) such as the shear viscosity (proportional) and the shear rate at the onset of shear thinning (inversely proportional). To illustrate this, for polystyrene the simulation predicts the correct zero shear viscosity $\eta_0 = \sqrt{m\epsilon}/\sigma^2 \Gamma \eta_0^* = 68$ Pa s (at $N = N_c$) for a factor $\Gamma = 10^4$ which happens to be equal to the ratio of relaxation times $\tau_{N_c}/\tau_1 = 10^4$. Accordingly, from the onset of shear thinning at shear rate $\dot{\gamma} = 10^{-4}$ obtained for the FENE chain melt at $N = N_c$ (see Fig. 12) we predict for the real shear rate (for polystyrene) $\dot{\gamma}_c = \dot{\gamma}^*(\sigma/\Gamma)^{-1}\sqrt{\epsilon/m} = 1100\ \mathrm{s}^{-1}$ which is again in agreement with experimental findings [165]. As a result, the shear stress at onset of shear thinning is correctly reproduced without adjustment by Γ, i.e., $(\eta_c\dot{\gamma}_c)/(\eta_c^*\dot{\gamma}_c^*) = 7.5$ MPa for polystyrene.

5. FENE-CB chains

In order to be prepared for the analysis of the flexible FENE-C (FENE model which allows for scission/recombination), FENE-B (which allows for bending stiffness) and FENE-CB fluids (both bending stiffness and scission) to be discussed below, we summarize results for the configurational statistics of wormlike chains (WLC) in external fields by using the method of functional integrals (FI) in quasimomentum space. From the correlation functions, statistical properties of WLCs, such as gyration radius and scattering functions can be obtained. By varying the bending rigidity the WLC exhibits a crossover from an ideal Gaussian chain to a rodlike chain. Simulations on the WLC model are widely available, see e.g. Refs. [177–180].

In 1960 Edwards [181] proposed a continuum model for polymer chains. For the ideal Gaussian chain, the FI can be solved exactly, and after taking excluded volume into account, a perturbation expansion as well as the renormalization group method are used to study the configurational statistics of polymer solutions [182–186].

5.1. Conformational statistics of wormlike chains (WLC)

The wormlike chain (WLC) model was first proposed by Kratky and Porod [187] and extended to the continuum level in [188,183]. It is described by a statistical weighting factor p for a polymer contour path $\boldsymbol{r}(s)$ with contour position s (imaged as time) $0 \leqslant s \leqslant L$:

$$p^{\mathrm{WLC}}(\boldsymbol{r}(s)) \propto \exp\left(-\frac{3}{2l}\int_0^L \boldsymbol{u}^2(s)\,\mathrm{d}s - \frac{\kappa}{2}\int_0^L \dot{\boldsymbol{u}}^2(s)\,\mathrm{d}s\right), \tag{28}$$

where L is the contour length of the chain, κ the bending elastic coefficient, $\boldsymbol{u}(s) \equiv \partial\boldsymbol{r}(s)/\partial s$ the differential (tangent) of the curve, and $\dot{\boldsymbol{u}} \equiv \partial\boldsymbol{u}/\partial s$. Using the constraint $|\boldsymbol{u}(s)| = 1$ a series solution

for the tangent distribution (Green's function) $G(\boldsymbol{u},\boldsymbol{u}';L,0)$ has been derived in [188]. Releasing the constraint and considering stretchable chains, end-to-end distances and the tangent distribution have been derived by using the method of Feynman [189,183]. Later it turned out that functionals in momentum space often used in field theories are a convenient method of studying properties of WLCs [33]. For a uniform system, the configurational statistics of WLCs can be accessed by considering the correlation function

$$\begin{aligned} C(\boldsymbol{R}_1,\boldsymbol{r}_2;s_1,s_2) &\propto \langle \delta(\boldsymbol{r}(s_1)-\boldsymbol{R}_1)\delta(\boldsymbol{r}(s_2)-\boldsymbol{R}_2)\rangle \\ &\propto \langle \delta(\boldsymbol{r}(s_1)-\boldsymbol{r}(s_2)-\boldsymbol{R})\rangle \propto C(\boldsymbol{R};s)\ , \end{aligned} \tag{29}$$

where $\boldsymbol{R}=\boldsymbol{R}_1-\boldsymbol{R}_2$, $s=s_1-s_2$, $0\leqslant s_1,\ s_2\leqslant L$ and $\langle..\rangle$ denotes a statistical average over various configurations of the chain by FI. The correlation function (29) is actually more fundamental than the end-to-end functions for WLCs [190], caused by chain end effects, except in the limit of Gaussian chains ($\kappa\to 0$).

5.1.1. Functional integrals for WLCs

We consider a polymer chain which is described by a three-dimensional curve $\boldsymbol{r}(s)$ with $0\leqslant s\leqslant L$. For convenience, the infinite long chain limit is taken then the normal mode coordinate, i.e., the Fourier transformation of $\boldsymbol{r}(s)$ is obtained as [191] $\boldsymbol{r}(s)=1/\sqrt{2\pi}\hat{\boldsymbol{r}}(k)e^{\mathrm{i}ks}\,\mathrm{d}k$, satisfying $\hat{\boldsymbol{r}}(k)=\hat{\boldsymbol{r}}^*(-k)$ because $\boldsymbol{r}(s)$ is real. The statistical weighting factor $p^{\mathrm{WLC}}[\hat{\boldsymbol{r}}(k)]$ for the WLC is, according to (28),

$$p^{\mathrm{WLC}}[\hat{\boldsymbol{r}}(k)] \propto \exp\left(-\frac{3}{2l}\int k^2\hat{\boldsymbol{r}}^2(k)\,\mathrm{d}k-\frac{\kappa}{2}\int k^4\hat{\boldsymbol{r}}^2(k)\,\mathrm{d}k\right)\ . \tag{30}$$

Physical properties X are obtained by FI in the quasimomentum space:

$$X=\int \mathscr{D}[\hat{\boldsymbol{r}}(k)]X[\hat{\boldsymbol{r}}(k)]\,p[\hat{\boldsymbol{r}}(k)]\ , \tag{31}$$

where $\int\mathscr{D}[\hat{\boldsymbol{r}}(k)]$ denotes the FI [192]. With regard to the correlation function (29) one has

$$\begin{aligned} &\delta((\boldsymbol{r}(s)-\boldsymbol{r}(0))-\boldsymbol{R}) \\ &\quad=\left(\frac{1}{2\pi}\right)^{3/2}\int_{-\infty}^{\infty}\exp\left(\mathrm{i}\boldsymbol{w}\cdot\left[\frac{1}{\sqrt{2\pi}}\int_{-\infty}^{\infty}\hat{\boldsymbol{r}}(k)(e^{\mathrm{i}ks}-1)\,\mathrm{d}k-\boldsymbol{R}\right]\right)\mathrm{d}^3w \end{aligned} \tag{32}$$

and the tangent of the curve at contour position s reads $\boldsymbol{u}(s)=(\sqrt{2\pi})^{-1}\int_{-\infty}^{\infty}\mathrm{i}k\hat{\boldsymbol{r}}(k)\exp^{\mathrm{i}ks}\,\mathrm{d}k$. Using standard methods [191,193], one obtains for the correlation function (29) for WLC from (30)

$$C(\boldsymbol{R},\boldsymbol{0};s,0)=\int\mathscr{D}[\hat{\boldsymbol{r}}(k)]\delta((\boldsymbol{r}(s)-\boldsymbol{r}(0))-\boldsymbol{R})\,p^{\mathrm{WLC}}\propto\exp(-R^2/4\Gamma_1)\ , \tag{33}$$

where $\Gamma_1=l\{s-\alpha^{-1}(1-e^{-s\alpha})\}/6$, $\alpha^2\equiv 3/(\kappa l)$, and therefore (33) simplifies to the expression $\exp\{-3R^2/(2ls)\}$ for ideal Gaussian chains. There is a variety of related correlation functions which have been discussed [33]. For example, one may consider the adsorption on a surface where the polymer has a fixed orientation $\boldsymbol{U}_0$ at $\boldsymbol{r}(0)$. The orientation distribution function of the tangent $\boldsymbol{U}$ at

position s becomes

$$C(\boldsymbol{U};s)=\int \mathscr{D}[\hat{\boldsymbol{r}}(k)]\delta(\boldsymbol{U}(s)-\boldsymbol{U})\,p^{\mathrm{WLC}}[\hat{\boldsymbol{r}}(k)]\propto \exp[-U^2/4\Gamma_2]\ , \tag{34}$$

independent of s due to translational invariance.

5.1.2. Properties of WLCs, persistence length, radius of gyration

From (33) we calculate the average monomer–monomer distance (MMD) separated by the contour distance s for WLC

$$\langle R^2\rangle(s)=l\left(s-\frac{1}{\alpha}[1-\boldsymbol{e}^{-s\alpha}]\right),\quad \langle R^4\rangle(s)=\frac{5}{3}l^2\left(s-\frac{1}{\alpha}[1-\boldsymbol{e}^{-s\alpha}]\right)^2\ . \tag{35}$$

Equations (35) are also obtained in [191,190] and differentiate from the average end-to-end distance obtained in [183]: $\langle R^2\rangle(L)=l\{L-(2\alpha)^{-1}\tanh(L\alpha)\}$, which demonstrates the difference between basic end-to-end and correlation functions through an end-effect. In order to patch up the difference, an additional term describing the end effect has been added to the Hamiltonian in [190]. For Gaussian chains, i.e., $\alpha\to\infty$, one recovers from (35): $\langle R^2\rangle=lL$, and for the opposite limit of rodlike chains, i.e., $\kappa\to\infty$, $\alpha->\infty$ the WLC at first glance give incorrect results and in order to make the model valid, an additional condition of the average length of the chain being L should be used, i.e., as discussed in detail by Freed [183], let $\int_0^L \mathrm{d}\tilde{s}=\int_0^L\langle(\boldsymbol{u}(s)\cdot\boldsymbol{u}(s))^{1/2}\rangle\,\mathrm{d}s=L$, where $\mathrm{d}\tilde{s}$ is differential arc length. Then we will obtain constraint on the parameters, l and κ, by Eq. (34) $\langle u^2\rangle=(\int u^2\,G(\boldsymbol{u};L)\mathrm{d}\boldsymbol{u})/(\int G(\boldsymbol{u};L)\,\mathrm{d}\boldsymbol{u})=6\Gamma_2=3l/(4\kappa)=1$, being equivalent to $l=4\kappa/3$. For example, if κ is selected as the independent parameter l will depend on κ and will have a meaning of an effective monomer length Kuhn length!. Another reasonable constraint can be obtained from $\langle|\boldsymbol{u}|\rangle=1$ which leads to $l=3\pi^2\kappa/16$. A different is derived by Freed [183] ($l=\kappa/3$ obtained from the end to end tangent distribution function, and in Ref. [190]), $l=(4/3)\kappa$ is derived by taking a limit on Eq. (33). Substituting $l=4\kappa/3$ into (35) we have $\langle R^2\rangle=l\{L-l(1-\boldsymbol{e}^{-2L/l})/2\}$, and l is proportional to persistence length (see below). For $\kappa\to\infty$ we now properly obtain the result for a rodlike polymer $\langle R^2\rangle=L^2$.

The persistence length l_p for finite contour length is obtained along the same line using the definition: $l_p\equiv\int R\cos\vartheta C(\boldsymbol{R},\boldsymbol{0},\boldsymbol{U}_0;s,0)\,\mathrm{d}^3R\,\mathrm{d}^3U_0/(\int C(\boldsymbol{R},\boldsymbol{0},\boldsymbol{U}_0;s,0)\,\mathrm{d}^3R\,\mathrm{d}^3U_0)$, i.e., $l_p=\phi_1\langle|\boldsymbol{U}_0|\rangle\Gamma_2^{-1}$ and therefore $l_p=[1-\exp(-s\alpha)]/\alpha$, where α is given after Eq. (33), which is similar to the result of Porod–Kratky [188]. For $s\to\infty$ one has $l_p=\alpha^{-1}=(2/3)\kappa=l/2$. For the radius of gyration, defined as $R_G^2=(1/2L^2)\int_0^L\mathrm{d}s\int_0^L\mathrm{d}s'\langle(R(s)-R(s'))^2\rangle$, we obtain, by making use of (35)

$$R_G^2=\frac{lL}{6}-\frac{l^2}{4}+\frac{l^3}{4L^2}\left[L-\frac{l}{2}(1-\boldsymbol{e}^{-2L/l})\right]\ . \tag{36}$$

For $\alpha\to\infty$ Eq. (36) becomes $R_G^2=lL/6$, which is just the ideal Gaussian chain radius of gyration. When $\alpha\to0$, using $l=4\kappa/3$ we have $R_G^2=\alpha lL^2/24=L^2/12$ which is just the expected result for a rodlike polymer. But there is notable peculiarity in the statistics when approaching the rodlike limit, as will be seen from the scattering function.

5.1.3. Scattering functions

In order to compare the result for the WLC with the ones for ideal Gaussian chains and rodlike chain, let us write down the corresponding isotropic scattering functions, for the Gaussian chain

$I(x) = N(2/x^2)(x - 1 + e^{-x})$, where $x \equiv k^2 R_G^2$, and for the rodlike polymer $I(x) = L^2(1/6x)\{2\sqrt{3x}\mathrm{Si}(2\sqrt{3x}) + \cos(2\sqrt{3x}) - 1\}$, where $\mathrm{Si}(x) = \int_0^x (\sin(t)/t)\,\mathrm{d}t$.

The scattering function for WLC is obtained from the Fourier transform of the correlation function $C(\boldsymbol{k}, \boldsymbol{U}, \boldsymbol{U}_0; L)$ and gives $I(k) = 2N/(L^2)\int_0^L (L - s)\exp\{-k^2 l[s - (1 - \exp(-s\alpha)/\alpha]/6\}\,\mathrm{d}s$. If we let $\kappa \to 0$, we see that the Gaussian limit is reobtained. But if we let $\kappa \to \infty$, this does not lead to the above $I(x)$ for rodlike chains. For that reason, the demonstrated approach leads to a so-called Gaussian rodlike polymer for $\kappa \to \infty$. Properties of the presented model have been also worked out for the case of WLC in external fields [33]. Finally, we mention a difference between the approaches discussed here and the one by Saito et al. [188]. We obtain $\langle \boldsymbol{u}(s) \cdot \boldsymbol{u}(s')\rangle \approx 1 - a^{-1} \approx \exp(-2|s - s'|/3l_p)$ for $|s - s'| \ll l_p$ and $a^{-1}/3 \approx \exp(-|s - s'|/l_p)$ for $|s - s'| \gg l_p$. which means, that for two segments far from each other these two models are consistent.

For molecules whose intrinsic rigidity against twist is important to interpret results the statistics to be presented for WLC had been extended to chiral ribbons [194].

5.2. FENE-C wormlike micelles

Aqueous surfactant solutions are known to form wormlike micelles under certain thermodynamic conditions, characterized by surfactant concentration, salinity or temperature. In the semi-dilute solution regime these linear and flexible particles, with persistence lengths varying from 15 to 150 nm form an entangled viscoelastic network. In equilibrium their behavior is analogous to that of polymer solutions and their properties obey the scaling laws predicted for the semi-dilute range [195]. See Ref. [196] for the prediction of more general surfactant microstructures (such as bilayers), their shapes, and shape fluctuations. In contrast to ordinary polymers, wormlike micelles can break and recombine within a characteristic time (breaking time) and their length distribution is strongly affected by flow. Phenomena such as shear banding structures, the variety of phase transitions and thixotropy are not completely understood [197]. This section contributes to this debate with a mesoscopic concept. There is huge number of both macroscopic and microscopic models available which deals with the prediction of the wormlike micellar phase, or a full phase diagram, changes in topology, etc. To summarize these works is certainly outside the scope of this review (see, e.g. the book by Gelbart et al. [29]). For a review on simulations of self-assembly see Ref. [30].

Wormlike micelles, with certain similarities to equilibrium polymers [198] can be modeled on a mesoscopic scale which disregards amphiphilic molecules and their chemistry by a modified version of the FENE potential which allows for scissions and recombinations of worms, the so-called 'FENE-C'(ut) for which the connector force between adjacent beads is parameterized by Q_C: $\boldsymbol{F}^{(\text{FENE-C})}(r) = \boldsymbol{F}^{(\text{FENE})}(r)$ for $r \leqslant Q_C$ and $\boldsymbol{F}^{(\text{FENE-C})} = 0$ for $r \geqslant Q_C$ with a rather irrelevant smooth interpolation at Q_C [199–201]. FENE-C reduces to FENE for $Q_C = Q_0$ and Q_C is trivially related to the scission energy (energy barrier for scission). In this section we will analyze this model both numerically (via NEMD) and analytically. The analytic model is based on an expression for the free energy of Gaussian chains, modified by a term which takes into account a finite scission energy in order to describe micelles, and extended to flow situations. In equilibrium, the length distribution then depends on two parameters, namely the micellar concentration and the scission energy. The shape of this distribution has a significant influence on flow alignment and the rheological behavior of linear micelles. The analytic approach to be discussed first exhibits similarities to the calculation of products in polymerization kinetics and to association theory [202,203,6]. Results will be

compared with the exact numerical solution in Section 5.2.3. The example in the next section has been chosen for illustrative purpose. Shear thickening rather than thinning occurs for a wide range of micellar systems, cf. [204,205] which is also obtained via a modified FENE-C which includes bending stiffness (FENE-CB models) and allows for the formation of networks.

5.2.1. Flow-induced orientation and degradation

Consider an ideal solution of linear chains (micelles) being modeled as bead–spring chains. We assume that each bead can have two bonds and we exclude ring formation. We consider a total number of N_b beads at (micellar) concentration c, where a bead represents a number of chemical units as already discussed in this review. Let $N_M \equiv cN_b$ denote the number of beads able to form linear chains ('M-beads') and which can associate and dissociate, and $N_S \equiv (1-c)N_b$ the number of solvent particles ('S-beads'). The system is then characterized by the number n_i of micellar chains made of i beads and c. At equilibrium the distribution of chains results from the grand canonical partition function $\Xi = \sum_{n_1=0}^{\infty} \dots \sum_{n_N=0}^{\infty} (q_1\lambda_1)^{n_1}(n_1!)^{-1} \dots (q_N\lambda_N)^{n_N}(n_N!)^{-1} = \prod_{i=1}^{N} \exp(q_i\lambda_i)$, where q_i and μ_i are the partition function and activity, respectively, of an i-chain ('subsystem' i), $\lambda_i = \exp(\beta\mu_i)$, and $\beta = 1/(k_BT)$. For the average number of i-chains one has $\langle n_i\rangle = \lambda_i \partial(\ln \Xi)/\partial\lambda_i = \lambda_i q_i$. Let us require that the various subsystems are in a chemical equilibrium with each other, i.e., $\mu_i = i\mu_1$. Thus, with $\lambda \equiv \lambda_1$, we have $\langle n_i\rangle = \lambda^i q_i$. For an i-chain the Hamiltonian $\mathscr{H}$ is formulated in terms of momentum and space coordinate of the center of mass, $\boldsymbol{p}_c$ and $\boldsymbol{r}_c$, respectively, and $i-1$ internal momenta and coordinates $\boldsymbol{P}_k, \boldsymbol{Q}_k$ with $(k = 1, \dots, i-1)$. We choose the internal coordinates such that $\boldsymbol{Q}_k$ denotes the kth bond vector between beads k and $k+1$. Carrying out the integration over momenta (Maxwell distribution) and coordinates yields $\int \exp(-\beta\mathscr{H})\, \mathrm{d}\boldsymbol{p}_c\, \mathrm{d}\boldsymbol{P}^{i-1}\, \mathrm{d}\boldsymbol{r}_c\, \mathrm{d}\boldsymbol{Q}^{i-1} = (2\pi m k_B T)^{3i/2} V q_i^{\mathrm{int}}$, where m is the mass of a single bead and V is the total volume of the solution, q_i^{int} denotes the internal configurational integral, and we can write $q_i = V q_i^{\mathrm{int}} \Lambda^{-3i}$, with the thermal de Broglie wavelength of a bead Λ. In order to simplify the structure of the following equations we equal the masses of M- and S-beads. For the calculation of the configurational integral we introduce a configurational distribution function ψ. The configurational integral is related to the free energy via $q_i^{\mathrm{int}} = \exp(-\beta A_i^{\mathrm{int}})$, with $A_i^{\mathrm{int}} = \int \mathrm{d}\boldsymbol{Q}^{i-1}\, \psi_i(k_BT \ln \psi_i + U_i)$, where U_i denotes the internal energy of an i-chain.

In order to keep this example simple, we assume Gaussian distributions, i.e.

$$\psi_i(\boldsymbol{Q}^{[i-1]}) = \frac{1}{(2\pi)^{3(i-1)/2}} \frac{1}{|\boldsymbol{C}_{i-1}^{-1}|^{1/2}} \times \exp\left(-\frac{1}{2}\, \boldsymbol{Q}^{[i-1]} \cdot \boldsymbol{C}_{i-1}^{\mathrm{T}} \cdot \boldsymbol{Q}^{[i-1]}\right) , \tag{37}$$

with $\boldsymbol{Q}^{[i-1]} \equiv (\boldsymbol{Q}_1, \boldsymbol{Q}_2, \dots, \boldsymbol{Q}_{i-1})$. The $3(i-1)\times 3(i-1)$ matrix of covariances is given by $\boldsymbol{C}_{i-1}^{-1} = \langle \boldsymbol{B}_i \rangle$ with $(\boldsymbol{B}_i)_{\mu\nu} \equiv \boldsymbol{Q}_\mu \boldsymbol{Q}_\nu$ $(\mu, \nu = 1, \dots, i-1)$ and $|\cdots|$ denoting a determinant. The tensor $\boldsymbol{B}_i$ becomes anisotropic under flow conditions. In the 'slow reaction limit' in which changes in micellar size occur on a time scale long compared to orientational diffusion of the segments in presence of flow, one can assert that the deformation energy can be added to the micellar free energy [206]. The internal energy of i-chains is then given by

$$U = -(i-1)E_{\mathrm{sc}} + \frac{1}{2} \sum_{j=1}^{i-1} H \langle Q_j^2 \rangle , \tag{38}$$

where E_{sc} is the scission energy, i.e. E_{sc} is the energy required to break a chain (independent of its length, for a more general case see [207]). For the moment we consider in (38) the FENE-regime

where bond stretching is not relevant which is especially reasonable for FENE-C chains for which Q_C is considerably smaller than Q_0. Inserting Eqs. (37) and (38) into the above integral expression for the free energy and performing the integration yields

$$A_i^{\text{int}} = -\frac{3}{2}(i-1)k_BT(1+\ln(2\pi)) - \frac{1}{2}k_BT\ln|\langle \boldsymbol{B}_i\rangle| - (i-1)E_{\text{sc}} + \frac{H}{2}\sum_{j=1}^{i-1}\langle Q_j^2\rangle \tag{39}$$

and, as such, is similar to an expression given by Booij [208]. Note that the last term on the rhs is proportional to the trace of the pressure tensor for an i-chain within the Rouse model, $H\sum_{j=1}^{i-1}\langle Q_j^2\rangle = V\text{Tr}(\boldsymbol{P}_i)$. Strict usage of the above relationships leads to

$$\langle n_i\rangle = V\left(\frac{\lambda}{\Lambda^3}\right)^i (2\pi)^{3(i-1)/2}|\langle \boldsymbol{B}_i\rangle|^{1/2} \times \exp\left((i-1)\left(\beta E_{\text{sc}} + \frac{3}{2}\right) - \beta\frac{V}{2}\text{Tr}(\boldsymbol{P}_i)\right) . \tag{40}$$

This expression provides a basis to analyze the length distribution for both equilibrium and nonequilibrium states. One can evaluate (40) in equilibrium by making use of expressions resulting from the Rouse model [6,209–211]. The number of i-chains is then given by $\langle n_i\rangle_0 = V(\lambda/\Lambda^3)^i z^{i-1}$, where

$$z \equiv (2\pi)^{3/2}|\langle \boldsymbol{QQ}\rangle_0|^{1/2}\exp(\beta E_{\text{sc}}) = \left(\frac{2\pi a^2}{3}\right)^{3/2}\exp(\beta E_{\text{sc}}) , \tag{41}$$

inherits the scission energy and represents an apparent volume of a bead. For the number density of micellar i-chains $\rho_i \equiv \langle n_i\rangle_0/V$ we arrive at $\rho_i = \rho_1^i z^{i-1}$. Through the constraint of conserved total density of beads $\rho = N_b/V$ the density ρ_1 of 1-chains can be expressed in terms of the concentration c and z in (41) by using rules for geometric series as

$$\rho c \equiv \sum_{i=1}^{N} i\rho_i = \rho_1/\{(1-\rho_1 z)^2\} . \tag{42}$$

5.2.2. Length distribution

The length distribution in equilibrium is thus determined by the scission energy and concentration and may also be rewritten in exponential form, $\langle n_i\rangle_0/\langle n_{i-1}\rangle_0 = \rho_i/\rho_{i-1} = \rho_1 z$. The normalized equilibrium distribution function $C_0(L)$ of L-chains is then equivalent to the expression derived by Cates [212] and reads

$$C_0(L) = \frac{1}{\langle L\rangle_0}\exp\left(-\frac{L}{\langle L\rangle_0}\right) . \tag{43}$$

From $\rho_i = \rho_1^i z^{i-1}$ we obtain the average equilibrium length (number of beads) of the micelles $\langle L\rangle_0 \equiv \sum_{i=1}^{N} i\rho_i/(\sum_{i=1}^{N}\rho_i) = (1-\rho_1 z)^{-1}$. Solving for ρ_1 leads to the relation $\langle L\rangle_0^2 - \langle L\rangle_0 = z\rho c$, which—itself—is solved (for positive lengths L) by

$$\langle L\rangle_0 = \frac{1}{2} + \left(\frac{1}{4} + z\rho c\right)^{1/2} . \tag{44}$$

For a simple fluid which is, within this framework, modeled by an infinitely large negative scission energy (FENE limit) we obtain the correct result $\langle L\rangle_0 = 1$ which we call a generalization of the square

root dependence obtained earlier. The generalization is important in reproducing the results from the microscopic model as well as to describe experimental results, for which at low concentrations the dependence of the micellar length on concentration seems to be quite weak.

For the case of FENE-C chains with Q_c close to Q_0 expressions become slightly more complicated, cf. [32]. More precisely, the ratio ρ_i/ρ_{i-1} increases weakly with i and therefore the length distribution $C_0(L)$ decreases weaker than exponentially with L. The concentration dependence of the average micellar length $\langle L\rangle_0$ is more pronounced than the square root behavior given in (22). The formalism presented also allows, for FENE-C chains, to calculate the variation of the length distribution with the flow rate, but the treatment becomes considerably more lengthy due to correlations between the bond vectors and the dependence of the pressure tensor on flow parameters.

Results presented in the figures have been obtained numerically using the above 'algorithm' (an extended version can be found in [32]). The second moment $\langle \boldsymbol{QQ}\rangle$ becomes anisotropic, the covariance matrix $|\langle \boldsymbol{B}_i\rangle|$ represents the shear induced orientation of segments. The concentration c is obtained numerically by the summation in (20). Varying the shear rate a maximum in the distribution of micellar lengths $C(L)$ occurs, which shifts to shorter chain length with increasing shear rate. Additionally the distribution becomes less broad with increasing rate. The flow alignment angle χ is expressed through the viscosities (assuming validity of the SOR) by $\chi = \pi/4 + \tan^{-1}[\dot\gamma\Psi_1/(2\eta)]$. We evaluate the material quantities such as the shear viscosity η from expressions involving $|\langle \boldsymbol{B}_i\rangle|/|\langle \boldsymbol{B}_i\rangle_0|$ and $\rho_1(\dot\gamma)$ [32]. It turns out that even for high scission energies the alignment angle does not decrease with increasing shear rate towards zero, because, in opposite to 'classical' polymers, here the average length of chains decreases implying a flow alignment angle which is just moderately decreasing.

A simplified approach to the analytic treatment of the FENE-C model subjected to flow may neglect the variation of the determinant of the covariance matrix with the shear rate, as done in [6,208] for (classical=nonbreakable) polymers, The approximation is justified by the fact that the determinant is of the order of $\dot\gamma^{1/2}$ which is small compared with the exponential of the trace of the pressure tensor. From the approximation follows an increase of the scalar pressure $p = \mathrm{Tr}(\boldsymbol{P}_i)/3$ with shear rate $\dot\gamma$, i.e. $\partial p/\partial\dot\gamma > 0$ which influences the given result (40) as if one would decrease the scission energy (see Eqs. (39), (40)). A decrease of that energy is connected with a decrease of the average length according to (41), (44) and hence with a decrease of the viscosity [6].

5.2.3. FENE-C theory vs simulation, rheology, flow alignment

Let us now compare the predictions of the nonsimplified analytic model described in the foregoing sections with NEMD simulation results for the full FENE-C model (temperature is kept constant at $k_BT/\epsilon = 1$, cutoff radius of the FENE-C potential chosen as $R_0 = 1.13\sigma$ implying $E_{\mathrm{sc}} = 8.09$, bead number density $n = 0.84$). Results can be compared without any remaining adjustable parameter, see Figs. 18–20. As can be seen clearly from Fig. 19 only the dependence of average length $\langle L\rangle$ divided by E_{sc} (representation motivated by Eq. (44)) on concentration is not in ideal agreement, but a tendency to a small slope at low concentrations is obvious. The slope at high concentrations is around 0.8 for the systems studied here. All other—nonequilibrium–quantities shown in Figs. 21–24 are described well.

Through (40) a phase separation between the short chain and long chain systems can be expected if the sign of $\partial p/\partial\dot\gamma$ depends on the length of chains as it has been detected for the microscopic FENE chain melt in [19]. Various hints for such a phase separation exist, e.g., under shear, a shear

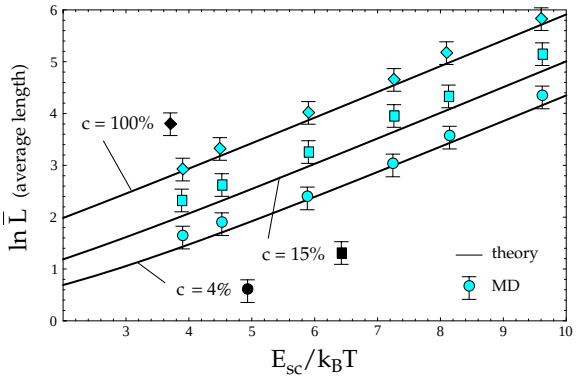

Fig. 18. MD results for average micellar length $\langle L\rangle_0$ vs the scission energy βE_{sc} for FENE-C micellar solutions (from 4% to 100%) in equilibrium. Lines: the mesoscopic result Eq. (44), The fit is parameter-free.

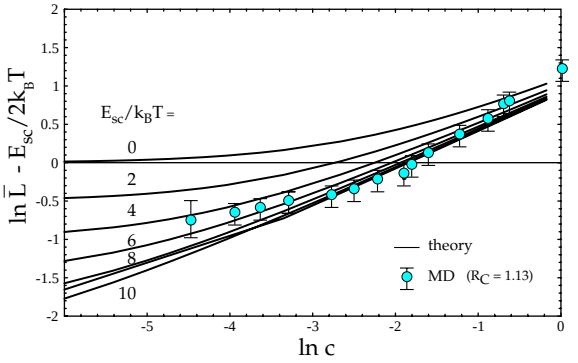

Fig. 19. MD results for the average micellar length $\langle L\rangle_0$ (reduced form) vs concentration c as compared with the mesoscopic result (Eq. (44)). The expression of Cates [212] predicts a constant slope in this representation.

banding structure has been observed by one of us [213]. Theoretical studies on the latter phenomenon have been already performed [214–216].

5.3. FENE-B semiflexible chains, actin filaments

Polymerized actin (F-actin) plays an essential role in cell mechanics and cell mobility, and is an attractive model for studying the fundamental physical properties of semiflexible polymers. Monomeric actin (G-actin, relative molecular mass $M_r = 42,000$) polymerizes in physiological salt solutions (pH 7.5, 2 mM $MgCl_2$, 150 mM KCl) to double-stranded filaments (F-actin). The F-actin solutions usually exhibit a polydisperse length distribution of 4–70 μm with a mean length of 22 μm. F-actin filaments have been extensively studied by Sackmann et al. Details about its physics and biological function can be obtained from [217,218], its role as model polymer for semiflexible chains in dilute, semidilute, liquid crystalline solutions [219] and also gels [220] has been recently discussed. Bio-molecular dynamics simulations have been also reviewed by Berendsen [221].

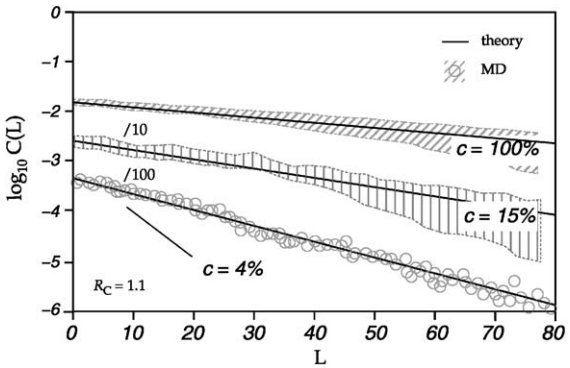

Fig. 20. MD results for the normalized equilibrium distribution of micellar length $C_0(L)$ for three samples at different concentrations c. Lines: the mesoscopic result (43) with same parameters as for the microscopic model.

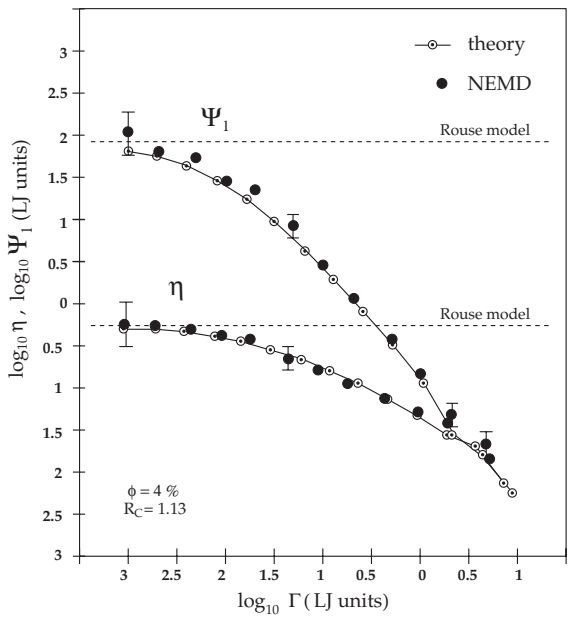

Fig. 21. Both NEMD and mesoscopic results for the non-Newtonian shear viscosity η, the viscometric function Ψ_1 vs the dimensionless shear rate Γ. All quantities are given in Lennard-Jones (LJ) units.

Our goal is to demonstrate, that the simple FENE-B model defined through its intramolecular bending (47) and FENE (1) potential (with $R_C = R_0$ in order to prevent chain breaking) plus the WCA potential for interactions between all beads allows for a rather efficient study of semiflexible model actin filaments at arbitrary concentrations and subjected to external fields on a coarse-grained level, i.e. in particular simple compared with dynamic rigid-rod models and atomistic MD. This is so since it is impossible to keep constraints exactly within a numerical approach, and approximative methods are ‘expensive’. Moreover, even actin filaments are stretchable, and conformations of FENE

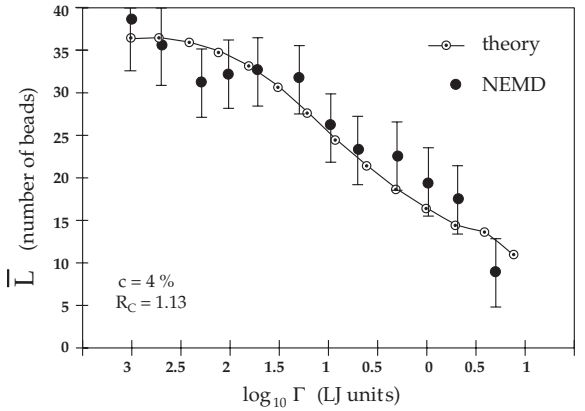

Fig. 22. Both NEMD and mesoscopic results for the average length of micelles $\langle L \rangle$ vs dimensionless shear rate Γ (LJ units).

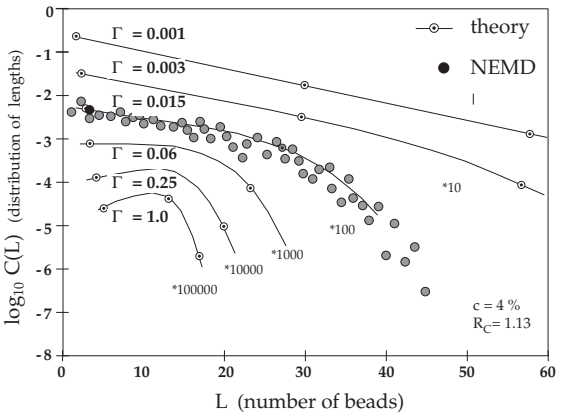

Fig. 23. Both NEMD and mesoscopic results for the length distribution $C(L)$ under shear (the shear rate is given in *LJ* units, the distribution function is normalized to unity and shifted for reasons of clarity).

chains share a fractal dimension $d_f = 1$ with nonstretchable (line) models. Gaussian chains and random walk conformation, in the opposite, are inappropriate models for actin since they belong to a class of fractal dimension $d_f = 2$.

If the model is restricted to the formation of linear molecules, the model serves to study linear actin filaments, if this restriction is released, we are going to model semiflexible networks. Notice also similarities with the case of flexible (linear and branched) micelles, for which FENE-C and FENE-CB models are used in the study of linear and branched micelles, respectively. For reviews discussing the relevant aspects in the formation of flexible and stiff networks and their mechanical properties we refer to Refs. [222–224,219]. Semiflexible block copolymers have been studied for a FENE model in [225].

Actin filaments can be regarded as classical wormlike chains which are shorter or comparable in length with their persistence length. Further to Section 5.1 we mention the result for the radial

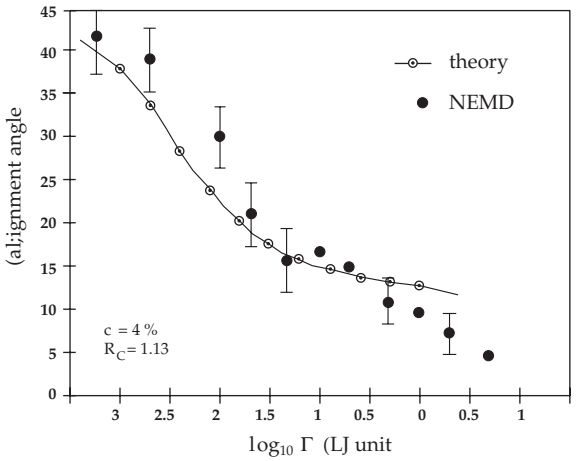

Fig. 24. Both NEMD and mesoscopic results for the flow alignment angle χ vs shear rate (LJ units).

distribution function $C(\boldsymbol{R}_{\rm ee};L)$ of the end-to-end vector [226,33] in the extreme limit of relatively stiff filaments: $C(\boldsymbol{R}_{\rm ee};L)\approx \ell_p(AL^2)^{-1}f(\ell_p\{1-\|\boldsymbol{R}_{\rm ee}\|/L\}/L)$, with $f(x)=(\pi/2)\exp(-\pi^2x)$ for $x>0.2$, and $f(x)=(1/x-2)(8\pi^{3/2}x^{3/2})^{-1}\exp(-1/4x)$ for $x\leqslant 0.2$. and a normalization factor A close to 1 according to [226]. The result is valid for $L\leqslant 2\ell_p, x\leqslant 0.5$ and (space dimension) $d=3$.

For actin filaments, concentration c is usually given in units of mass per volume, whereas theoretical and simulation studies prefer to deal with concentrations $\tilde{c}$ in units of length per volume. The relevant regime is $c\approx 1$ mg/ml. Since for the weight of actin one has 370×43 kD/μm $=2.64\times 10^{-11}$ μg/μm, a solution with the desired concentration c contains 3.8×10^{10} μm/ml $=38$ μm/μm^3, i.e., we are interested in systems with $\tilde{c}\approx 10$–100 μm/μm^3. For simplicity, considering a cubic (equidistant) lattice with lattice spacing ξ_l we have: $\xi_l=\sqrt{3/\tilde{c}}\approx\sqrt{0.1}\approx 0.3$ μm. A minimum estimate for the length of a segment of the multibead FENE-B chain a should be $\xi_l\approx 5a$, and the segment (or bead number) concentration n to be used in the simulation of FENE-B filaments is $n=\tilde{c}/a\approx 5\tilde{c}/\xi_l=5\tilde{c}^{3/2}/\sqrt{3}$. Concerning the system size, if we need to study a realistic regime, where the length L of filaments is $L\approx 5$ μm, and the box size is twice the contour length, the total number of beads is $40L^3\tilde{c}^{3/2}/\sqrt{3}$. For the desired concentration of about 1 mg/ml, we arrive at a large number. The system should contain $8\times 125\times 5\times 135\approx 7\times 10^5$ beads. The situation is better—from the viewpoint of number of particles—for a minimum (still relevant) concentration of 0.1 mg/ml, for which 20,000 beads are sufficient.

Restrictions for the chain dynamics within an entangled polymer solution can be demonstrated by comparing the transient contours of a free actin filament with the ones of an actin filament embedded in semidilute solution. A decrease of the amplitudes for the thermally excited undulations is measured for the embedded filament, see Fig. 25 for an animation of our NEMD computer simulation result. The restricted chain motion can be understood in terms of the undulations of a filament in a tube formed by the surrounding entangled filaments, and allows to determine its local diameter by measuring the maximum flicker amplitudes: Let y_i denote the local axes of the tube at the two ends ($i=1,2$). The reptation diffusion coefficient along the tube, $D_\parallel$, according to [218], can be determined by evaluating the random fingering motion of the chain ends. If the chain end positions (x_i, y_i), with

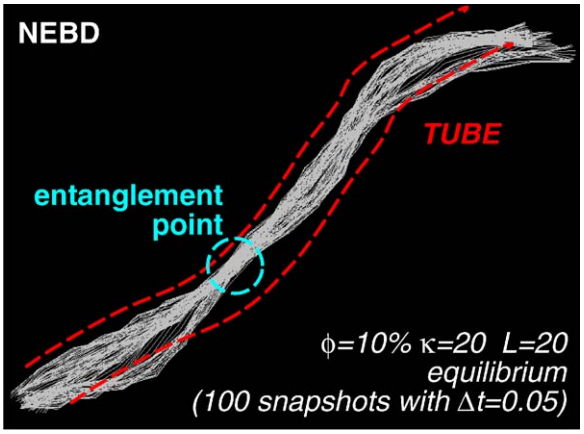

Fig. 25. Transient contours of a single FENE-B actin filament with 100 beads embedded in a semidilute solution.

respect to a local coordinate system with y-axes parallel to the tube axes at the ends are recorded at fixed time intervals $\triangle t$, $D_{\|}$ is determined as the arithmetic mean of the diffusion coefficients parallel to the tube at both ends according to $D_{\|} = (A \triangle t)^{-1} \sum_{i=2}^{N_{\text{steps}}} (y_1^i - y_1^{i-1})^2 + (y_2^i - y_2^{i-1})^2$, where $A \equiv 4(N_{\text{steps}} - 1)$, and N_{steps} is the number of steps. In Ref. [218], projections of the filament contour to a plane $(x - y)$ were analyzed from experiment.

In order to extract the corresponding reptation diffusion coefficient from the bead trajectories of the FENE-B model, embedded in 3D space, one has to precise the above definition, i.e., we hereby define the orientation of a tube on the basis of the temporary end-to-end vector of the semiflexible chain: $\boldsymbol{R}_{\text{ee}}(T) \equiv T^{-1} \int_0^T [\boldsymbol{r}_N(t) - \boldsymbol{r}_1(t)]\,\mathrm{d}t$, which depends on the chosen time interval T. Let $\boldsymbol{n}_T$ denote the normalized quantity $\boldsymbol{n}_T \equiv \boldsymbol{R}_{\text{ee}}(T)/\|\boldsymbol{R}_{\text{ee}}(T)\|$, then the diffusion coefficient of a single bead parallel to 'its' tube is $D_T^{\text{k}} \equiv (2T)^{-1} \langle (\boldsymbol{n}_T \cdot [\boldsymbol{r}_k(T) - \boldsymbol{r}_k(0)])^2 \rangle$, where $\langle \ldots \rangle$ represents a time average. The reptation diffusion coefficient along the tube of the polymer with N beads is then expressed as $D_{\|} \equiv (D_T^{\text{1}} + D_T^{\text{N}})/2$. For rods the expected result is $D_{\|} = k_B T \ln(L/b)/(2\pi\eta_s L)$, where L is the contour length, b the diameter of the filament, k_B is Boltzmann constant, T is the temperature and η_s is the viscosity of the solvent. In addition, we need to have a formula to extract the orientation diffusion coefficient $D_{\text{or.}}$ and a tube width a, based on the time evolution of the end bead coordinates of the semiflexible chain. The concept has physical meaning for semiflexible or stiff chains, but is obviously meaningless for ideal chains. Now, let $\boldsymbol{r}_1(t)$ and $\boldsymbol{r}_N(t)$ denote the coordinates of the end beads of a representative chain, separated by $\boldsymbol{R}_{\text{ee}} \equiv \boldsymbol{r}_N(t) - \boldsymbol{r}_1(t)$. The natural choice for a definition of the orientational diffusion coefficient is $D_{\text{or}}(T) \equiv (4T)^{-1}(\boldsymbol{n}_T - \boldsymbol{n}_0)^2$, to be extracted in a range where $D_{\text{or}} \ll 1/T$. In this range, $D_{\text{or}}(T)$ should be independent of T. For rods the theoretical result is $D_{\text{or}} = 3k_B T\,(\ln(L/b) - \gamma)/(\pi\eta_s L^3)$, where $\gamma \approx 0.8$, but slightly dependent on L/b [209]. Finally, based on the trajectories of all the three beads we estimate a perpendicular diffusion coefficient as follows

$$D_{\perp}(T) \equiv \frac{1}{2T} \int_0^T \left(\frac{\boldsymbol{R}_{\text{ee}}(T)}{\|\boldsymbol{R}_{\text{ee}}(T)\|} \times \frac{\mathrm{d}\boldsymbol{r}_C(t)}{\mathrm{d}t} \right)^2 \mathrm{d}t\,. \tag{45}$$

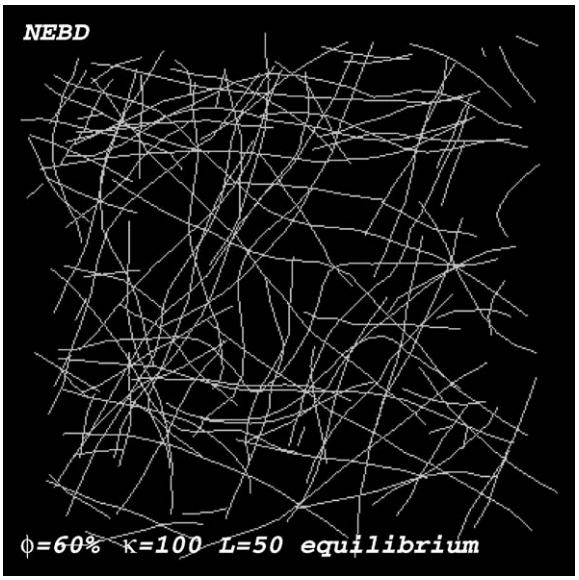

Fig. 26. Equilibrium high density semiflexible FENE-B chains (48) for system parameters given in the figure.

For rods, the theoretical result is $D_\perp = D_\parallel/2$, and the so-called 'disentanglement time' can be related to $D_\parallel$ through $\tau_d = L^2/D_\parallel$, a 'tube radius' a can be defined by $a^2 \equiv L^2 D_{\rm or}\tau_d = L^4 D_{\rm or}/D_\parallel$, and the center of mass diffusion is obtained via $D_{\rm cm} = (D_\parallel + 2D_\perp)/3$. Experimentally, thermal undulations of the filament (visible by microscopy) have been used to define the tube diameter; it is estimated as the maximum deflection along the contour, at sufficiently large concentrations, within a limited time interval.

Figs. 26, 27 provide snapshots of FENE-B model actin filaments in equilibrium as well as in a nonequilibrium situation. Our preliminary results (which should be improved in the near future) for the reptation and orientational diffusion coefficients defined in the previous section are summarized in Table 4. The effect of concentration on the end-to-end distribution function of FENE-B actin filaments is demonstrated by Fig. 28, for the diffusion coefficient $D_\parallel$ vs chain length see Fig. 29. A solutions of actin filaments exhibits pronounced shear thinning, non-Newtonian rheological behavior of the FENE-B model is reported in Fig. 30. The simulation of dilute and semidilute solutions of actin filaments remains a challenge for computer simulation due to the stiffness of filaments which requires large samples in order to prevent finite size effects.

To give an impression for possible further applications of the presented FENE-C and FENE-CB models, we end up this section with few snapshots. Figs. 31, 32 show FENE-CB3 networks with different rigidities, whereas Fig. 33 has been obtained for an extended version of the FENE-CB∞ model, for which the bending potential (47) has been modified such that in-plane scissions between more than three beads (at branching points) are preferred (see Table 1 conc. nomenclature).

The incorporation of f-branching into the FENE-C model, which carries a single scission energy $E_{\rm sc}$ (since $f = 1$ in its simplest form) generally introduces f independent parameters characterizing scissions and recombinations.

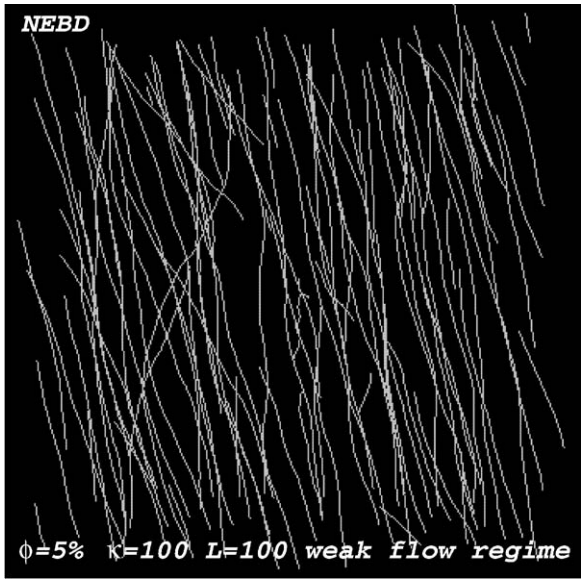

Fig. 27. Flow-aligned FENE-B chains for system parameters given in the figure.

Table 4
Preliminary simulation result for the scaling behavior of various diffusion coefficients (see text part) for semidilute solutions of the FENE-B model actin filaments

	D_{mon}	D_{or}	$D_{\parallel}$	$D_{\perp}$
$\propto c^{-\alpha}$ with $\alpha=$	0.6(1)	0.7(2)	0.5(1)	0.6(1)
$\propto \kappa^{-\beta}$ with $\beta=$	0.3(1)	0.3(2)	0.3(1)	0.3(1)
$\propto L^{-\gamma}$ with $\gamma=$	0.5(4)	2.1(2)	0.5(5)	0.3(2)

The scaling exponents have been estimated in the concentration regime (5–60%), relative bending rigidities $\kappa/L=0.5$–2.

5.4. FENE-B liquid crystalline polymers

Thermotropic liquid crystals form mesophases intermediate between a solid phase at low temperatures and an isotropic liquid phase at high temperatures [227–229]. Nematic liquid crystals possess an orientational order of the molecular axes but no long range positional order. Smectic liquid crystals, in particular those referred to as SmA and SmC have a nematic like orientational order and in addition their centers of mass are confined to layers. Previous computational studies on the phase behavior of model liquid crystals by MD and Monte Carlo (MC) simulations have been performed on various levels of simplification of the molecular interactions [230,231,201]. Simulations of the Lebwohl–Lasher lattice model [232,233] gave hints on the basic features of the phase transitions. The simplest approach where the dynamics of the centers of mass of the particles are properly taken into account

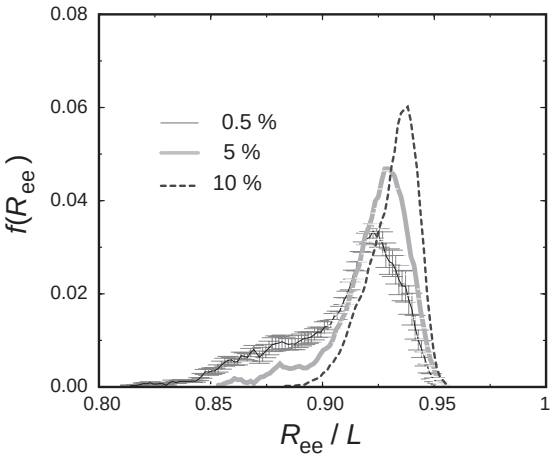

Fig. 28. Effect of concentration c on the end-to-end distribution function $f(\boldsymbol{R}_{ee})$ vs $\boldsymbol{R}_{ee}/L$ of FENE-B actin filaments ($\kappa = 200$, $L = 100$). For the curve with $c = 0.5\%$, error bars are shown.

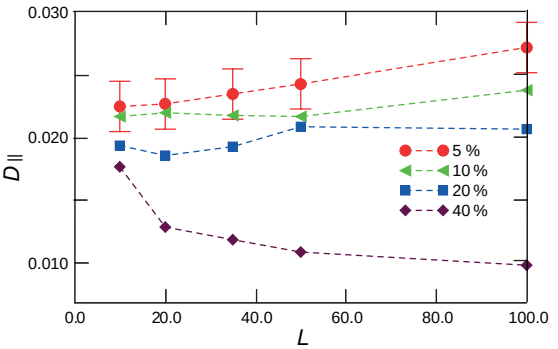

Fig. 29. Diffusion coefficient parallel to the tubes vs chain length L for the FENE-B model actin filaments at various concentrations.

is to treat molecules as stiff non-spherical particles like ellipsoids or spherocylinders, or to consider particles interacting by a Gay–Berne potential [234–236]. Going further the internal configuration has been taken into account by treating the molecules as being composed of interaction sites (monomers) connected by formulating constraints or binding forces. Both Monte Carlo [237–240,201] and MD methods [241–243] were applied to study the static and dynamic properties, respectively. Extremely huge compounds such as lipids in the liquid crystalline phase have been simulated as well [244,245]. The effect of semiflexibility and stiffness of macromolecules on the phase behavior of liquid crystals has been extensively discussed on analytic grounds by Odijk and others [36,246]. However from a physical point of view the construction of model interactions remains in question [247,248], and from the technical point of view, the development of efficient implementations [249–252] is challenging

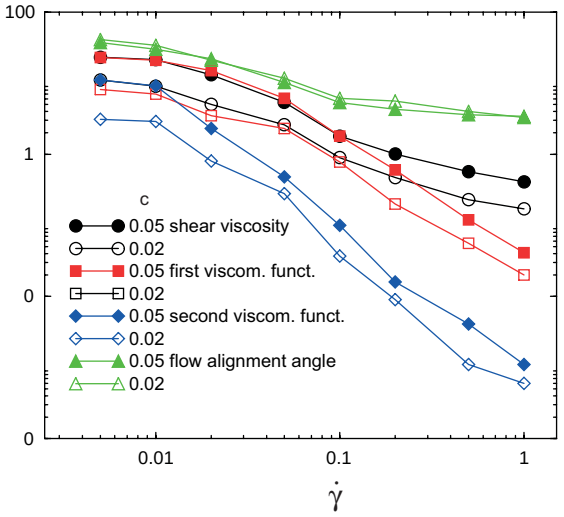

Fig. 30. Viscosity coefficients and flow alignment angle vs shear rate for both, 2% and 5% solutions of FENE-B actin filaments ($\kappa = 100, L = 100$).

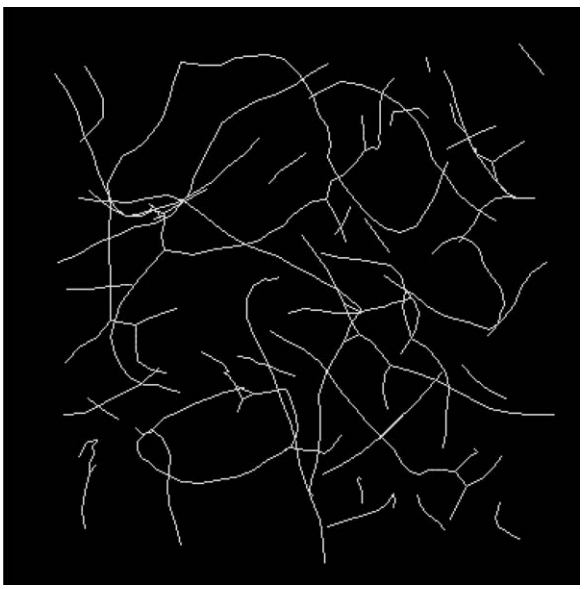

Fig. 31. Sample snapshot of a realization of a system made of FENE-CB6 chains (47). Beside scissions/recombinations of chains (parameterized through a scission energy E_{sc}) the model allows for the formation of branchings and carries a parameter for the (in plane) stiffness of chains. The concentration is $c = 5\%$. Result obtained via BD.

due the complexity of detailed models which involve long range electrostatic forces or many body potentials.

This section reviews a simple microscopic model for a 'representative' thermotropic liquid crystals composed of partially stiff, partially flexible molecules. Our system is composed of intramolecularly

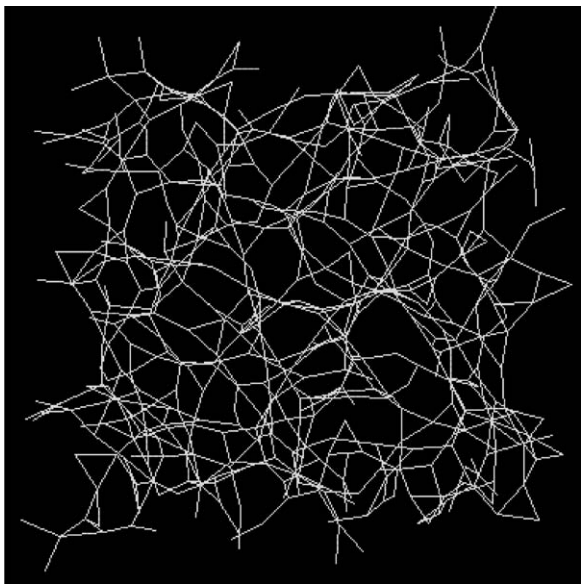

Fig. 32. Same system as in Fig. 31 at concentration $c = 20\%$. Result obtained via BD.

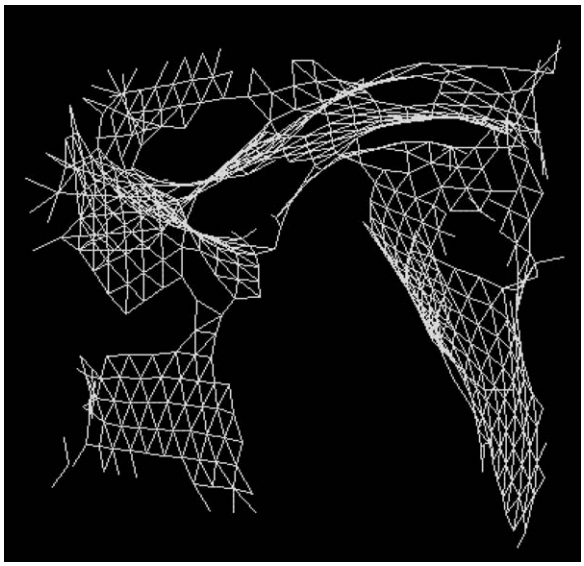

Fig. 33. Sample snapshot of a realization of a system made of semiflexible FENE-CB chains. Beside scissions/recombinations of chains (parameterized through a scission energy E_{sc}) the model potential naturally allows for the formation of branchings and carries a parameter for the stiffness of chains.

inhomogeneous FENE-B chains, interacting via a LJ potential, and the attractive part of the LJ potential is taken into account only between their stiff parts. This model has been introduced in [35]. The model system is composed of n_c multibead chains with N beads per chain. Each chain,

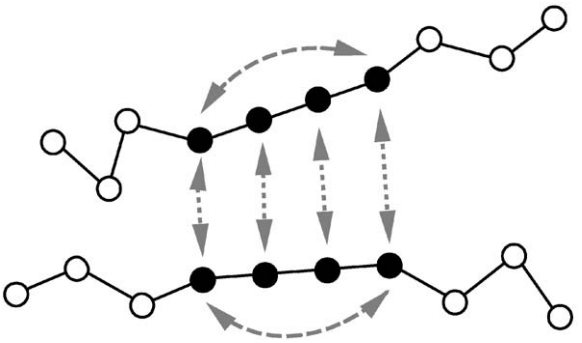

Fig. 34. The bead–bead interactions. In addition to the interactions indicated in this figure, there are also a FENE interaction between all connected beads in chains and a repulsive Lennard-Jones between all beads of the system [35].

as shown in Fig. 34 is made of two identical terminal flexible parts (N_{flex} beads) and a central stiff part (N_{stiff} beads) where $N_{\text{stiff}} + 2 \times N_{\text{flex}} = N$. The notation ($N_{\text{flex}} - N_{\text{stiff}} - N_{\text{flex}}$) had been used to characterize the different systems. For example, $(3-4-3)$ means that the chains in this system are composed of a central stiff part of 4 beads and two terminal flexible parts of 3 beads. Simulations are performed in the NVT ensemble. Results to be reported below were obtained for a system of $n_c = 288$ chains of length $N = 10$ at bead number density $n = 0.8$. All beads are interacting with a WCA potential. Adjacent (connected) beads within chains interact via a FENE force. The central part of each chain is kept stiff with a strong (large κ) FENE-B interaction. Additionally, corresponding beads within the stiff parts of different chains interact via the attractive part of the LJ potential ('smectic' biased) producing an effectively anisotropic interaction between stiff parts. The strength of the attractive interaction is adjustable by a depth parameter ϵ_{att}.

5.4.1. Static structure factor

The static structure factor of the multibead fluid where each bead is assumed to act as a 'scatterer' can be written as a product between inter- and intramolecular structure factors $S(\boldsymbol{k}) = S_{\text{sc}}(\boldsymbol{k}) S_{\text{inter}}(\boldsymbol{k})$. The single chain static structure factor representing the intramolecular correlations is defined as

$$S_{\text{sc}}(\boldsymbol{k}) = \frac{1}{n_c N} \sum_{\alpha=1}^{n_c} \left\langle \left| \sum_{j=1}^{N} \exp(\mathrm{i}\boldsymbol{k} \cdot \boldsymbol{x}_j^{(\alpha)}) \right|^2 \right\rangle . \tag{46}$$

Here $\boldsymbol{x}_j^{(\alpha)}$ denotes position of bead j within chain α, $\boldsymbol{k}$ the wave vector transfer, and $n_c N$ the total number of beads. The static structure factor $S(\boldsymbol{k})$ is restricted to $k = |\boldsymbol{k}| = 2\pi p / L_b$ (p integer, L_b simulation box length). The single chain static structure $S_{\text{sc}}(\boldsymbol{k})$ is not subject to this restriction for k because it can be calculated from the unfolded chains, independent of the size of the basic simulation box. A long range positional is revealed by Bragg like peaks in another static structure factor $S_{\text{cm}}(\boldsymbol{k})$ where the centers of mass of the molecules are taken as scatterer. For ideal crystals the height of the Bragg peaks approaches n_c, the number of molecules in the scattering volume. For a layered (smectic) structure with a separation distance d between layers a peak occurs at $k = 2\pi/d$. Its height divided by n_c provides a convenient measure for the degree of positional order σ, i.e., we have

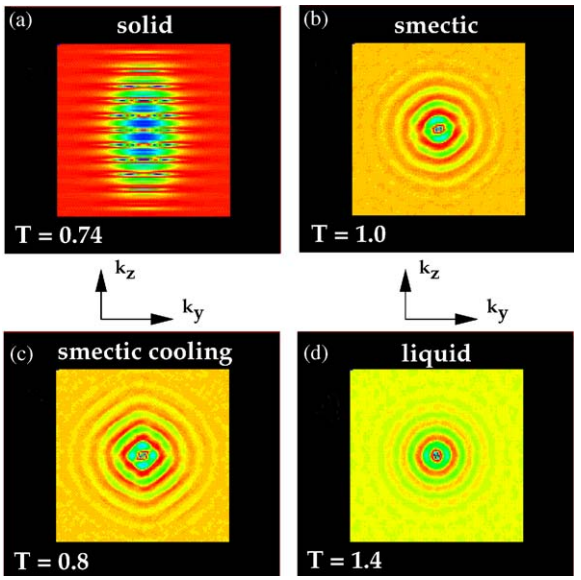

Fig. 35. Single chain static structure factor S_{sc} as projected onto the x-plane ($k_x = 0$) at different temperatures: $T = 0.74$ (a), $T = 1.00$ (b), $T = 0.80$ (c), and $T = 1.40$ (d) for the *3–4–3* system. Adapted from Ref. [35].

Table 5
Influence of the ratio between stiff and overall length of the special FENE-B molecules on their melting and clearing temperatures [35]

$n_{flex} - n_{stiff} - n_{flex}$	3–4–3	3–5–3	0–10–0
$(n_{stiff} - 1)/n_b$	0.34	0.40	1.00
Melting temperature	0.75	0.90	3.0
Clearing temperature	1.2	2.0	>5.0

$\sigma \equiv |\langle n_c^{-1} \sum_{\alpha=1}^{n_c} \exp(2i\pi z^{(\alpha)}/d)\rangle|$, where $z^{(\alpha)}$ is a center of mass coordinate of chain α with respect to a symmetry-adapted coordinate system, and $\langle..\rangle$ denotes a time average Fig. 35.

For a number of these semiflexible systems it had been observed that a smectic phase is well defined over a wide range of temperatures whereas the nematic phase is too narrow in temperature to be seen clearly. The smectic phase becomes increasingly disordered upon decreasing the strength of attraction (parameter ϵ_{att}). The effect of architecture (amount stiff/flexible) has been studied to a certain extend in [35]. According to Table 5 clearing temperatures as well as melting temperatures increase for this model upon increasing the length of the stiff part. This in qualitative agreement with experiments. Some snapshots and results for order parameters are given in Figs. 36 and 37.

To our best knowledge, the nematic phase has not been studied via computer simulation for this model as long as flexible parts are present. Of course, for stiff molecules [253], the nematic phase is pronounced in a broad temperature regime in contradistinction to the smectic phase which appears in a small temperature interval (Figs. 38 and 39). An expected phase diagram for the system is

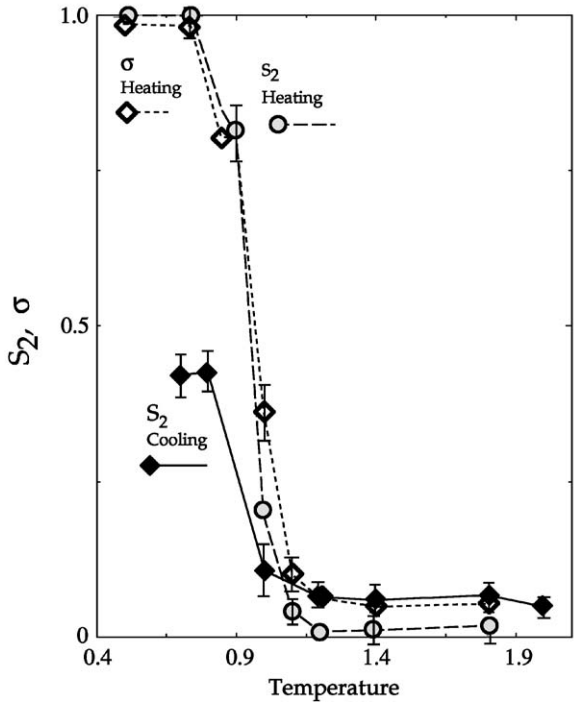

Fig. 36. Orientational order parameter S_2 and positional order parameter σ vs. temperature for the *3–4–3* FENE-B system, observed during heating (from an ideal fcc structure) and (subsequent) cooling [35].

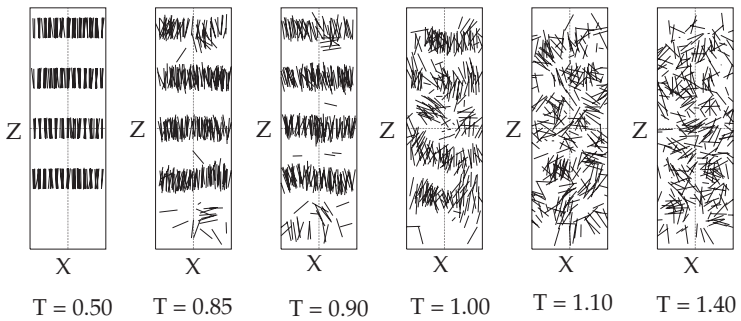

Fig. 37. During heating: Snapshots of the stiff central parts of molecules at different temperature T (increasing from left to right). For the 2–4–3 FENE-B system [35].

shown in Fig. 40. A nematic phase should be favored for longer chains with $N \gg 10$, and also for nonsymmetric molecules.

5.5. *FENE-CB transient semiflexible networks, ring formation*

Both the analytic and numerical tools for linear wormlike micelles reviewed in the foregoing sections can be used to predict the extent of loop formation as function of the micellar concentration,

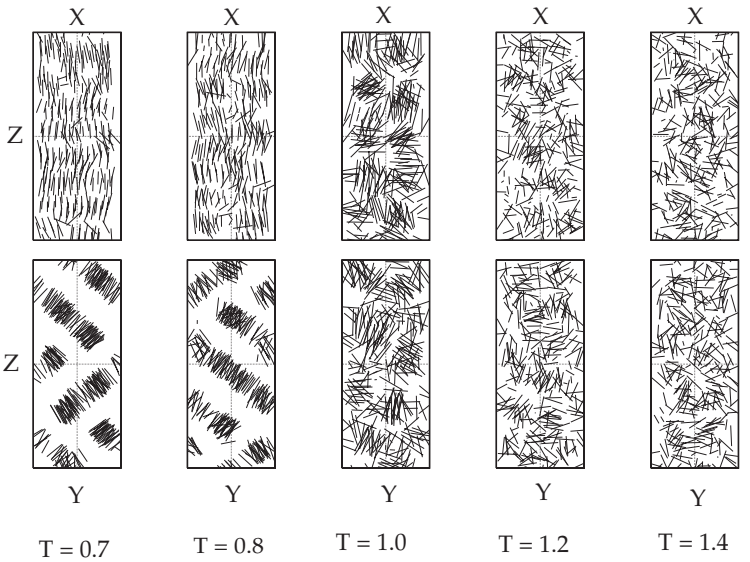

Fig. 38. During cooling (compare with Fig. 37). Snapshots of the stiff parts of the molecules in two orthogonal projections *3*–4–*3* FENE-B system [35].

the end-cap energy and the flexibility of linear micelles. As a matter of fact, even if loop formation is unfavorable under many conditions, e.g., for stiff micelles and low end-cap energies, they have to be treated correctly in any statistical approach to their behavior, since their presence can significantly affect the relaxation time spectrum, the rheological behavior and correlation function of various types. Analytic considerations on the statistics of ring formation are available in Ref. [255].

We recall that the FENE-C (or FENE-C2) potential acts between all pairs of beads (whose spatial distance is below a certain threshold value Q_C) as long as both beads have only one or two interacting neighbors. Such a transient bond between connected beads defines the chain itself as well as its contour and it breaks if any bond length exceeds the threshold value. In order to also account for stiffness (which disfavors, or better, prevents ring formation) the FENE-B (classical semiflexible linear polymers) and FENE-CB model (including scission and recombination) are introduced as follows:

$$U^{\text{FENE-CB}}(r,\vartheta) = U^{\text{FENE-C}}(r) + U^{\text{B}}(\vartheta)\,, \tag{47}$$

$$U^{\text{B}}(\vartheta) = \kappa(1-\cos\vartheta)\,, \tag{48}$$

where κ is the bending coefficient and ϑ is the angle between connected bonds, such that $\vartheta = 0$ for a stretched chain. Note, that the bending potential is a three-body potential, whereas the FENE potential is a two-body potential, and the notation in (47) is a formal one. According to Table 1 the FENE-B*n* model is the natural extension of the FENE-B allowing for maximum functionality *n* (classical saturated and unsaturated networks for small and large bending stiffness, respectively). The FENE-CB and FENE-B models have not yet been characterized in an exhaustive fashion. Flexible FENE-*n* networks also known as 'finitely extensible network strand (FENS)' [256] models have been used to investigate strain hardening behavior for associating polymeric systems in [257], overshoot

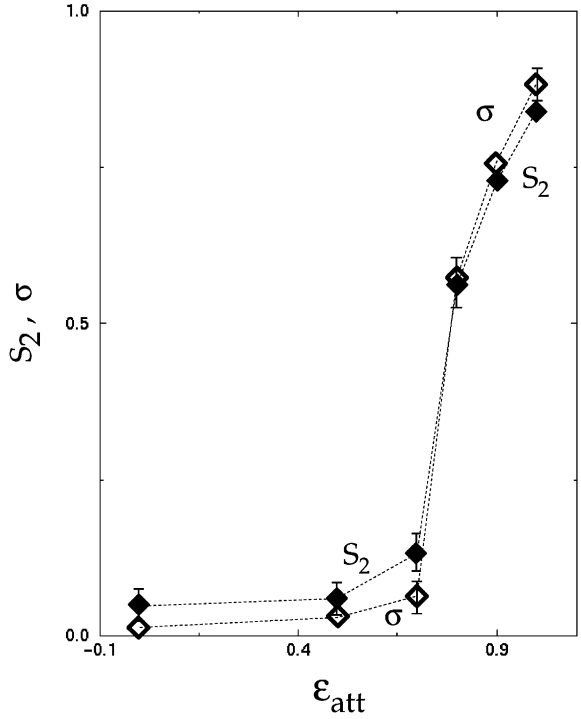

Fig. 39. The order parameters S_2 (nematic) and σ (smectic) as function of ϵ_{att} at the temperature $T = 0.8$ for the *3–4–3* FENE-B system [35].

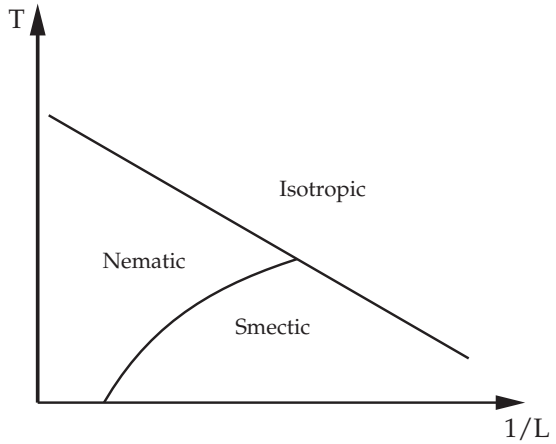

Fig. 40. Typical experimental phase diagram where L is length of the chains and T denotes temperature [254].

in the shear stress growth function and strand extensibility in [258]. Remarkable progress has been made in the understanding of polymer gels [259] where 'equilibrium' properties of a FENE-C type network model were studied in detail via MC. The authors artificially prohibit association of direct

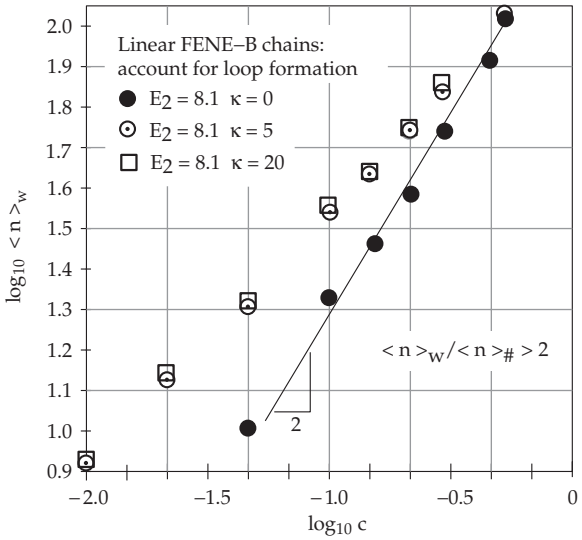

Fig. 41. The average weight size for linear FENE-CB chains vs concentration for different bending coefficients κ. Results obtained via BD.

neighbors but it seems that agreement between experiments and FENE model predictions can be further improved by taking bending stiffness into account (FENE-CB). At the same this article provides an excellent review on continuum and molecular theories of stress–strain relations for networks (including classical network theory, nonaffine deformation theory, scaling model, rod and coil model). To get a feeling on the power of FENE-CB network models and their range of application we present a tiny result obtained in a preliminary study. The model exhibits characteristic behaviors as those shown in Figs. 41 and 42 when solving the FENE-CB model via BD. With increasing concentration the probability of loop formation decreases resulting from the increase of average length of micelles. With increasing scission energy loop formation becomes favorable, but increasing stiffness decreases the tendency of ring formation. At large concentrations and large values for the bending stiffness parameter κ there are deviations from the square root behavior $\langle n\rangle_{\#} \propto \sqrt{c}$ which are expected when a mean-field approach is used to describe the effect of concentration. A snapshot is given in Fig. 43.

6. Primitive paths

Having discussed the range of applicability for various FENE chain models mostly listed in the upper part of Table 1 one may expect that we also review the FENE models in the lower part of this table. Fortunately, several reviews exist summarizing the constitutive equations following from the approximations involved in the FENE-P.. and FENE-L. models, cf. [37,6,74] such there is no need to summarize them—and there usefulness in micro–macro applications—here. Rather, we turn to simple low dimensional models depicted in the upper part of Fig. 2, i.e. tube models and elongated particle models for the description of complex fluids. One may ask how these levels of descriptions are related. This will be discussed in Section 8.8.

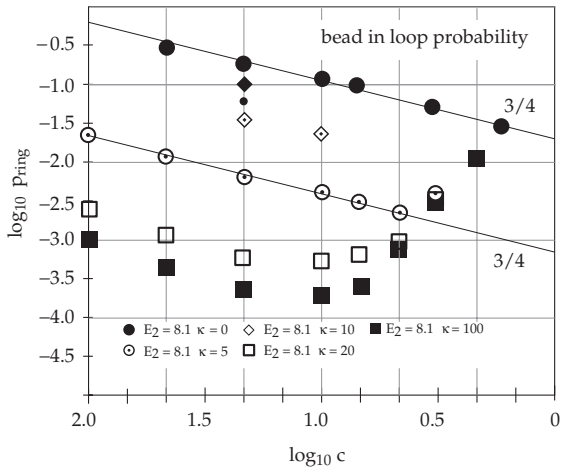

Fig. 42. Probability to find a bead inside a loop for different bending coefficients κ and concentrations c. Model system as for Fig. 41.

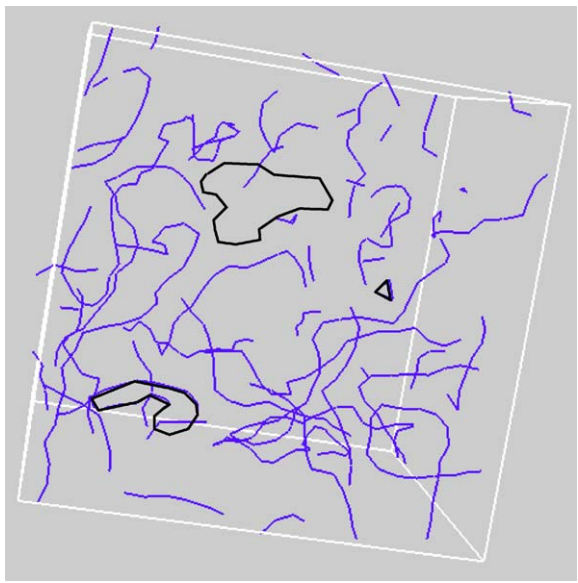

Fig. 43. Snapshot of a BD computer simulation configuration of FENE-C wormlike micelles with parameters $c = 0.02$, $\kappa = 5$ and $E_2 = 4$. Here, a small system size, containing 1000 beads, was chosen for reasons of clarity.

6.1. Doi–Edwards tube model and its improvements

A molecular model for polymer melts was elaborated by Doi and Edwards (DE) [209] who extended the reptation idea introduced by de Gennes [154] to a tube idea in order to describe the viscoelastic behavior of entangled polymers in the presence of 'obstacles'. Within the tube and

reptation pictures, the complex entanglement interaction between polymer chains has been treated in a rather direct approach, i.e. each chain in the polymer system is equivalent to a chain restricted to one dimensional motion (so-called 'reptation') in a confining tube, except for its two ends which can move in any possible direction. In addition to the reptation mechanism, DE originally assumed instantaneous and complete chain retraction, affine tube deformation by the flow, and independent alignment of tube segments. By doing so, they obtained a closed-form constitutive equation which only involves the second moment of the orientation vector for a tube segment. For highly entangled, linear polymers, the original DE model has been extended to incorporate chain contour length fluctuations [260,261] and constraint release due to the motion of the surrounding chains (so-called 'double reptation') [262,263]. The combination of these two effects lead to a refined description of the linear viscoelastic properties [264], however, the model is much less successful for the nonlinear properties. The major experimental observations that the original DE theory fails to describe in the nonlinear regime are the following [265,266]: (A) There exist irreversible effects in double-step strain experiments with flow reversal, (B) Over a wide range of shear rates $\dot{\gamma}$ above the inverse disentanglement time $1/\tau_d$ the steady shear stress is nearly constant for very highly entangled melts or solutions or increases slowly with shear rate for less highly entangled ones. The first normal stress difference N_1 increases more rapidly with shear rate than does the shear stress over the same range of shear rates. The slope of N_1 versus $\dot{\gamma}$ increases as the molecular weight decreases, (C) The steady-state shear viscosity of different molecular weights merge into a single curve in the high shear rate, power-law regime, (D) The shear stress shows transient overshoots in the start-up of steady shear flow at low shear rates. The strain at which the maximum in the overshoot occurs increases with shear rate at high rates, (E) The first normal stress difference exhibits transient overshoots in the start-up of steady shear flow at moderate shear rates, (F) The rate of stress relaxation following cessation of steady shear flow is shear rate dependent, (G) The steady-state extinction angle decreases more gradually with shear rate than predicted by the DE model, (H) The transient extinction angle shows an undershoot at the start-up of steady shear at high shear rates; it also shows an immediate undershoot when the shear rate is suddenly decreased after a steady state has been reached, finally it reaches a higher steady-state value [267], (I) Steady-state values of the dimensionless uniaxial extensional viscosity are non-monotonic functions of extension rate.

In order to improve the situation, many attempts of modifying the original DE model have been made during the last years and been reviewed in [7]. Several physical effects have been found to be important for more realistic modeling of nonlinear properties of entangled polymers. Upon these the most important are avoiding the independent alignment (IA) approximation, double reptation, chain stretching, convective constraint release (CCR), and anisotropic tube cross sections. For a review on these effects, their influence on the quality of predictions for rheological quantities a good reference might be Ref. [265]. Recently, reptation models incorporating all the well established phenomena (except for anisotropic tube cross sections) have been formulated based on a full-chain stochastic approach suitable for computer simulations [268–270,149]; on a full-chain, temporary network model with sliplinks, chain-length fluctuations, chain connectivity and chain stretching [271]; on coupled integral-differential equations [272]; and a reptation model including anisotropic tube cross sections, chain stretching, double reptation, and CCR, while avoiding the IA approximation [273,265]. The predictive power of the Jacobi identity has been demonstrated for the latter model which is thermodynamically admissible, i.e., compatible with the GENERIC framework (Section 8.3). It is encouraging that these reptation models can quite successfully reproduce the

experimentally observed rheological behavior in a large number of flow situations. Very recently, Doi merged together the network model of Green and Tobolsky, and the tube model of Edwards and de Gennes. The resulting model, called the dual slip-link model, can be handled by computer simulation, and it can predict the linear and nonlinear rheological behaviors of linear and star polymers with arbitrary molecular weight distribution [274]. Unified stress–strain models for polymers, including polymer networks have been presented by Wagner [275,276]. Rather than going into further detail with these models for polymer melts, and in order to go into detail with any of the established models, we take an illustrative example from our own research, where the original tube model is subject to a very minor modification. This will allow us to discuss an analytic expression for the dynamic viscosities, a decoupling approximation used to evaluate nonlinear elastic behaviors, and Galerkin's method to solve the underlying FP equation efficiently.

6.2. Refined tube model with anisotropic flow-induced tube renewal

Point of departure are classical kinetic equations for the orientational distribution function of polymer segments in melts. In the DE tube model the macromolecules of a polymeric liquid are idealized as freely jointed primitive paths characterized by the orientation of a segment $\boldsymbol{u}$ at contour label s (we use $0 \leqslant s \leqslant 1$). The orientation of the segment at the 'position' s is determined by the orientational distribution function $\psi = \psi(t,s,\boldsymbol{u})$ which, in general, also depends on the time. The kinetic equation for $\psi = \psi(t,s,\boldsymbol{u})$ is written as

$$\frac{\partial\psi}{\partial t} = -\boldsymbol{\omega}\cdot\mathscr{L}\psi - \mathscr{L}\cdot(\boldsymbol{T}_{\text{flow}}\psi) + \mathscr{D}_{\text{rep}}(\psi) + \mathscr{D}_{\text{or}}(\psi), \quad \boldsymbol{T}_{\text{flow}} \equiv \frac{1}{2}B\mathscr{L}(\overline{\boldsymbol{uu}} : \boldsymbol{\gamma}), \tag{49}$$

with angular operator $\mathscr{L} \equiv \boldsymbol{u}\times\partial/\partial\boldsymbol{u}$, vorticity $\boldsymbol{\omega} \equiv (\boldsymbol{\nabla}\times\boldsymbol{v})/2$ associated with the (macroscopic) flow field $\boldsymbol{v}$, $\boldsymbol{\gamma} \equiv (\boldsymbol{\kappa}+\boldsymbol{\kappa}^{\dagger})/2$ with $\boldsymbol{\kappa} \equiv (\nabla\boldsymbol{v})^{\dagger}$, and $\boldsymbol{T}_{\text{flow}}$ is the orienting torque exerted by the flow. The kinetic equation of Peterlin and Stuart [277] for solutions of rod-like particles (where the variable s is not needed) is of the form (49) with $\mathscr{D}_{\text{or}}(\psi) \equiv w\mathscr{L}^2\psi$, where w stands for the orientational diffusion coefficient. Often the corresponding relaxation time $\tau \equiv (6w)^{-1}$ is used to discuss results. The (reptation) diffusion term of DE can be written as $\mathscr{D}_{\text{rep}} \equiv \lambda^{-1}\partial^2/\partial s^2\psi$, with a relaxation time $\lambda = L^2/D$, which is connected with a disentanglement time via $\tau_d = \lambda\pi^{-2}$. The $\mathscr{D}$-terms describe the 'damping', which guarantees that ψ approaches the isotropic distribution $\psi_0 = (4\pi)^{-1}$ in the absence of orienting torques. With an additional torque caused by a mean field taken into account in (49), such a kinetic equation will be applied below to the flow alignment of liquid crystals [81]. Here we consider both diffusion mechanisms. For the case of rodlike segments ($B = 1$) the FP equation (49) is equivalent with the diffusion equation in [6,278].

With the normalization $\int\psi\,\mathrm{d}^2\boldsymbol{u} = 1$ for the orientational distribution function $\psi = \psi(t,s,\boldsymbol{u})$ (time t) the average $\langle\psi\rangle$ of a function $\Psi = \Psi(\boldsymbol{u})$ is given $\langle\Psi\rangle = \int\Psi\psi\,\mathrm{d}^2\boldsymbol{u}$ and depends on t and s. Here, the (2nd rank) alignment tensor (26) $\boldsymbol{a} = \boldsymbol{a}(s,t) = \langle\overline{\boldsymbol{uu}}\rangle = \langle\boldsymbol{uu} - \boldsymbol{I}/3\rangle$ is once more of particular importance. The symbol $\overline{\ }$ denotes the symmetric traceless part of a tensor, and $\boldsymbol{I}$ is the unit tensor. Considering a planar Couette flow in x-direction, gradient in y-direction, the shear rate $\dot{\gamma}$ for the macroscopic velocity profile $\boldsymbol{v}$ is $\dot{\gamma} \equiv \partial v_x/\partial y$. For this geometry, only 3 of the 5 independent components of the alignment tensor do not vanish. In the spirit of Section 2.1 we abbreviate—for

the present purpose—as follows:

$$a_+ \equiv \langle u_x u_y \rangle, \quad a_- \equiv \frac{1}{2}\langle u_x^2 - u_y^2 \rangle, \quad a_0 \equiv \frac{3}{4}\left\langle u_z^2 - \frac{1}{3} \right\rangle, \quad \text{and } \tilde{\boldsymbol{a}} \equiv (a_+, a_-, a_0)^{\mathrm{T}} . \tag{50}$$

A viscous flow gives rise to a flow alignment [277,279] which can be detected optically via its ensuing birefringence. The alignment, in turn, affects the viscous flow [279,280] and consequently the stress tensor $\boldsymbol{\sigma}$ contains a contribution associated with the alignment, more specifically, $\boldsymbol{\sigma} = 2\eta_{\mathrm{iso}}\boldsymbol{\gamma} + \boldsymbol{\sigma}_a$, and $\boldsymbol{\sigma}_a = 3n_p k_B T R \int_0^1 \boldsymbol{a}(t,s)\,\mathrm{d}s$, where η_{iso} is the 'isotropic' viscosity for $\boldsymbol{a} = \tilde{\boldsymbol{a}} = 0$. n_p and T are the molecule number density and the temperature of the liquid. The relation between $\boldsymbol{\sigma}_a$ and $\boldsymbol{a}$ (SOR, discussed in Section 4.6) which has been derived by Giesekus [280] and used by DE is a limiting expression for long and thin segments corresponding to $B = 1$. In general the factor B is the ratio of two transport coefficients [279,81]. Curtiss and Bird [6] replaced $3B$ by 1 and presented additional viscous contributions associated with the 'link tension'. These terms are disregarded here.

6.2.1. Linear viscoelasticity of melts and concentrated solutions

Multiplication of (49) with $\overline{\boldsymbol{u}\boldsymbol{u}}$ and integration over the unit sphere yields

$$\left(\frac{\partial}{\partial t} + \tau^{-1} - \lambda^{-1}\frac{\partial^2}{\partial s^2}\right)\boldsymbol{a} = \frac{2}{5}B\boldsymbol{\gamma} + \cdots , \tag{51}$$

with $\tau = (6w)^{-1}$. The dots stand for terms involving products of $\boldsymbol{a}$ with the vorticity $\boldsymbol{\omega}$ and $\boldsymbol{\gamma}$, as well a term which couples $\boldsymbol{a}$ with an alignment tensors of rank 4. These terms can be inferred from [81], they are of importance for the non-Newtonian viscosity and the normal pressure differences (see next section). For an analysis of the frequency dependence of the viscosity in the Newtonian regime, these terms can be disregarded, i.e. we consider the only nonvanishing component a_+ of $\boldsymbol{a}$.

The complex viscosity $\eta^* = \eta' - i\eta''$ of a viscoelastic medium can be determined by measurements under oscillatory shear flow (or deformation) $\boldsymbol{\gamma} \sim \mathrm{e}^{-\mathrm{i}\omega t}$. The relaxation of the material causes a phase-shift δ between (complex) stress and deformation which is related to the complex viscosity ($\tan\delta \equiv \eta'/\eta''$), or alternatively, to the storage G' and loss modulus G'' via $G^* = G' + \mathrm{i}G'' \equiv \mathrm{i}\omega\eta^*$. With the ansatz $\boldsymbol{a} = 2B\boldsymbol{\gamma}C/5$ the scalar function $C(\omega, s)$ with dimension of time obeys $(\tau^{-1} - \mathrm{i}\omega)C - \lambda^{-1}(\partial^2/\partial s^2)C = 1$. The boundary condition proposed by DE are random orientations for the chain ends, $\forall_t \psi(s=0,\boldsymbol{u}) = \text{const}$. This implies $\forall_\omega C(\omega, s=0) = 0$. We wish to take into account the property of chain ends to participate in the flow alignment of the complete chain, or equivalently, anisotropic (flow-induced) tube-renewal. Working out this modification, we set $C(\omega, s=0) = \tau_{\mathrm{end}}$, in order to introduce an additional relaxation time τ_{end} for this process. The solution reads

$$C(\omega, s) = \lambda\left[\frac{1}{z^2} + \left(\frac{1}{z^2} - g\right)\left(\frac{\tanh(z/2)}{\sinh^{-1}(sz)} - \cosh(sz)\right)\right], \quad z \equiv \sqrt{\tau^{-1}\lambda - \mathrm{i}\omega\lambda}\,, \tag{52}$$

with $g \equiv \tau_{\mathrm{end}}\lambda^{-1}$ being a dimensionless 'order' parameter for the chain ends. From the above relations alone we immediately obtain an analytic expression for the complex viscosity:

$$\eta^*(\omega) = G_a\lambda\left[\frac{1}{z^2} + \left(g - \frac{1}{z^2}\right)\left(\frac{2\tanh(z/2)}{z}\right)\right], \tag{53}$$

with a shear modulus $G_a = 3B^2 n_p k_B T/5$. A Maxwell model type expression is obtained if $\tau \ll \lambda$. For polymer melts and highly concentrated solutions where the reorientational motion is strongly hindered, one expects the opposite situation, viz. $\tau \gg \lambda$. The pure reptation model considered by DE

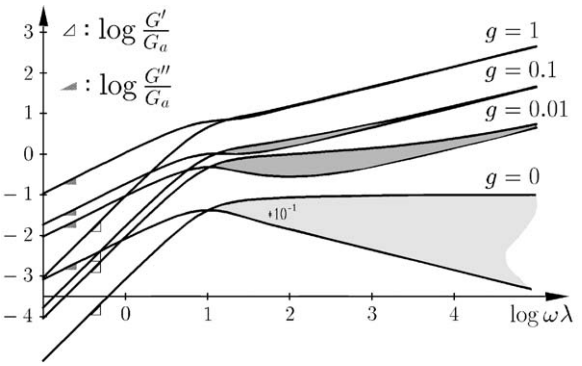

Fig. 44. Shear moduli G' and G'' vs frequency ω for various values of the parameters g for anisotropic tube renewal. Adapted from Ref. [278].

corresponds to $\tau^{-1}\lambda \to 0$ and consequently $z \to y$ with $y \equiv (-\mathrm{i}\omega\lambda)^{1/2} = (1-\mathrm{i})\Omega^{1/2}$, and $\Omega \equiv \omega\lambda/2$. In this case (53) reduces to $\eta^*(\omega) = \eta_{\mathrm{DE}}[H^*_{\mathrm{DE}}(\omega) + H^*_{\mathrm{end}}(\omega)]$ with the DE viscosity $\eta_{\mathrm{DE}} = G_a\lambda/12 = n_p k_B T\lambda/20$, and dimensionless (complex) damping functions $H^*_{\mathrm{DE}} = 12y^{-2}\{1 - 2y^{-1}\tanh(y/2)\}$, and $H^*_{\mathrm{end}} = g\,24y^{-1}\tanh(y/2)$. The index 'end' labels a term, which vanishes for $g=0$ and represents the influence of anisotropic tube renewal on the frequency behavior of the viscosity. Some of deficiencies of the DE model have been overcome by inclusion of anisotropic chain ends. By NEMD simulation of a FENE melt in [278] we found strong support for implementing this modification. Moreover, the expected scalings $\tau_{\mathrm{end}} \propto \eta_{\mathrm{Rouse}} \propto L$ and $\lambda \propto \eta_{\mathrm{DE}} \propto L^{3.4}$ and therefore $g \sim L^{-2.4}$ (L is proportional to the molecular weight) allow to predict—in good agreement with experiments—the effect of chain length on the dynamics viscosities, and in particular on the width of the plateau regime.

In distinction to the DE theory ($g=0$), for high frequencies the presented modification predicts one region, where both moduli display the same characteristics, independent of g, and another (plateau) region, where the storage modulus is nearly constant within a g-dependent frequency range. For a plot of the dynamic viscosities see Fig. 44. Notice that the moduli tend to overlap with increasing values for the shear frequency. The positive slope of G' and G'' at high frequencies ω follows here without the recourse to 'glassy relaxation modes', as suggested by Ferry [165]. To complete the discussion we mention the explicit result for the shear relaxation modulus $G(t) \equiv \int_0^\infty \eta'(\omega)\cos(\omega t)\,\mathrm{d}\omega$. We obtain $G(t) = 8G_a \sum_{\alpha,\mathrm{odd}}((\pi\alpha)^{-2} + g)\exp(-t/\lambda_\alpha)$ with $\lambda_\alpha = \lambda/(\pi\alpha)^2 = \tau_d\alpha^{-2}$, thus reducing to the DE result for vanishing g. For short chains, i.e., large g one obtains an expression $G_R(t)$—by the way quite similar to the one of the Rouse model— which satisfies $G_R(t) = -g\lambda\tau^{-1}\,\mathrm{d}G/\mathrm{d}t$. For a comparison between predictions, Eq. (53), and experimental data see Figs. 45 and 46.

6.3. Nonlinear viscoelasticity, particular closure

Multiplication of (49) with $\overline{\boldsymbol{uu}}$ and subsequent integration over the unit sphere, considering further the equation of change for the fourth rank alignment tensor and neglecting the anisotropic alignment tensor of rank 6, which is equivalent to a specific 'decoupling approximation', a closed equation of change is obtained (compare with previous section):

$$\left(\frac{\partial}{\partial t} + \tau^{-1} - \lambda^{-1}\frac{\partial^2}{\partial s^2}\right)\boldsymbol{a} = \frac{2}{5}B\boldsymbol{\gamma} + \frac{6B}{7}\,\overline{\boldsymbol{\gamma}\cdot\boldsymbol{a}} + 2\,\overline{\boldsymbol{\omega}\times\boldsymbol{a}}\ , \tag{54}$$

where $\overline{\boldsymbol{\omega}\times\boldsymbol{a}}_{ij} = \overline{\epsilon_{ikl}\omega_k a_{lj}} = (\epsilon_{ikl}\omega_k a_{lj} + \epsilon_{jkl}\omega_k a_{li})/2$ if rewritten in components (using Einstein summation convention). In terms of the components $\tilde{\boldsymbol{a}}$ of the alignment tensor (defined in Eq. (50)) we can rewrite Eq. (54) for stationary of time-dependent simple shear flow as

$$\underbrace{\mathscr{D}\begin{pmatrix} a_+ \\ a_- \\ a_0 \end{pmatrix}}_{\equiv\tilde{\boldsymbol{a}}} = \underbrace{\begin{pmatrix} \varsigma & \Gamma & \Upsilon \\ -\Gamma & \varsigma & 0 \\ \Xi & 0 & \varsigma \end{pmatrix}}_{\equiv\boldsymbol{M}} \cdot \tilde{\boldsymbol{a}} + \underbrace{\begin{pmatrix} -\Theta \\ 0 \\ 0 \end{pmatrix}}_{\equiv\boldsymbol{\Theta}}, \quad \text{with} \begin{pmatrix} \Upsilon \\ \Xi \\ \Theta \end{pmatrix} \equiv B\Gamma \begin{pmatrix} 2/7 \\ 3/14 \\ 1/5 \end{pmatrix}, \tag{55}$$

i.e., $\mathscr{D}\tilde{\boldsymbol{a}} = \boldsymbol{M}\cdot\tilde{\boldsymbol{a}} + \boldsymbol{\Theta}$ with the differential operator $\mathscr{D}$, a matrix $\boldsymbol{M}$ and inhomogeneity (vector) $\boldsymbol{\Theta}$, dimensionless shear rate $\Gamma = \dot{\gamma}\lambda$, ratio between reptation and orientational relaxation times $\varsigma = \lambda/\tau = \pi^2\tau_d/\tau$ and dimensionless coefficients Υ, Ξ, Θ defined in (55). The solution is $\tilde{\boldsymbol{a}}$ as function of s, t, and $\dot{\gamma}(t)$. Usually the rheological quantities can be expressed in terms of the integral $\int \tilde{\boldsymbol{a}}(s,t)\,\mathrm{d}s$. An example will be given below. A weighted average had been considered in [6].

6.3.1. Example: refined tube model, stationary shear flow

For the refined tube model (with anisotropic tube renewal, both reptation and orientational damping, closure approximation, Eq. (54)) we need to solve the corresponding matrix equation with $\mathscr{D} = \partial^2/\partial s^2$. The analytic solution for $\tilde{\boldsymbol{a}}(\sigma)$ can be immediately written down. The result is determined by the real part $k^R = \{(\sqrt{\Delta+\varsigma^2} - \varsigma)/2\}^{1/2}$ and imaginary part $k^I = \sqrt{\Delta}/(2k^R)$ of a complex wave vector. For the mean alignment (vector) $\tilde{\boldsymbol{a}} \equiv \int_0^1 \tilde{\boldsymbol{a}}(\sigma)\,\mathrm{d}\sigma$ we obtain by performing a simple integration an explicit result for the alignment in terms of shear rate, reptation and orientational relaxation times, shape factor B, and parameterized tube renewal:

$$\begin{pmatrix} a_+ \\ a_- \\ a_0 \end{pmatrix} = \frac{\Theta}{(\Delta+\varsigma^2)}\begin{pmatrix} \varsigma \\ \Gamma \\ -\Xi \end{pmatrix} + \frac{1}{\sqrt{\Delta(\Delta+\varsigma^2)}}\begin{pmatrix} \sqrt{\Delta}\cap & \sqrt{\Delta}\cup \\ \Gamma\cup & -\Gamma\cap \\ -\Xi\cup & \Xi\cap \end{pmatrix} \cdot \begin{pmatrix} k^R & k^I \\ k^I & -k^R \end{pmatrix} \cdot \begin{pmatrix} \sin\dfrac{k^R}{2}\cosh\dfrac{k^I}{2} \\ \cos\dfrac{k^R}{2}\sinh\dfrac{k^I}{2} \end{pmatrix}, \tag{56}$$

where all symbols except $\cap, \cup, V, \Lambda$ being related to the parametric (tube renewal) boundary conditions $a_\pm^{\mathrm{end}} \equiv a_\pm(s=0)$ were introduced in terms of dimensionless shear rate, shape factor B, and ratio ς just above. We have $(\cap,\cup) \equiv (\cos k^R + \cosh k^I)^{-1}\ ((\Lambda,-V),(V,\Lambda))\cdot(\cos(k^R/2)\cosh(k^I/2), \sin(k^R/2)\sinh(k^I/2))$. with $\Lambda \equiv a_+^{\mathrm{end}} - \varsigma\Theta/(\Delta+\varsigma^2)$ and $V \equiv \Gamma^{-1}\sqrt{\Delta}(a_-^{\mathrm{end}} - \Gamma\Theta/(\Delta+\varsigma^2))$. Assuming the SOR, the non-Newtonian shear viscosity η is obtained from $\tilde{\boldsymbol{a}}$ through $\eta = 2C^{-1}\dot{\gamma}^{-1}a_+$ with a stress-optic coefficient C discussed earlier. The same applies to the normal stress differences (captured by a_-, a_0).

6.3.2. Example: transient viscosities for rigid polymers

For this example we evaluate (54) without reptation ($\lambda^{-1} = 0$) and the differential operator is identified to be $\mathscr{D} = -\lambda\partial/\partial t$ (just formally, λ drops out in the result). The analytic solution for the

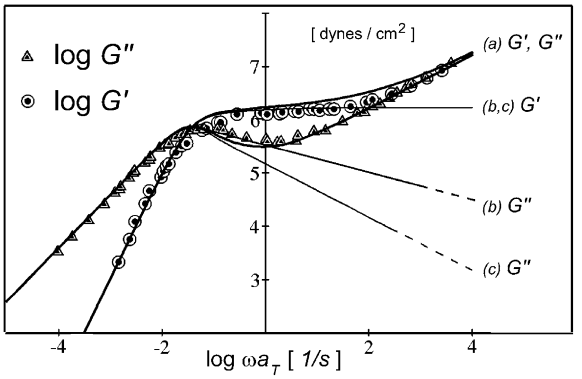

Fig. 45. Comparison between theory and experiment for the loss and storage moduli, Eq. (53). Experiments (symbols) are for on a monodisperse polysterene melt ($M_\omega = 215,000$) [281]. The moduli are functions of shear rate reduced to a reference temperature of $T^{\text{red}} = 160°\text{C}$ by a factor a_T. (a) The two upper solid lines (for G' an G'') pertain to the theoretical parameters $G_a = 1.7 * 10^6$ dynes cm^{-2}, $\lambda = 260$ s and $\tau_{\text{end}} = g\lambda = 1$ s. (b) The theoretical curves for $g = 0$ corresponding to the result of Doi and Edwards [209], Curtiss and Bird [6], de Gennes [195] are also shown. (c) The calculation of Doi [260] takes into account fluctuations in the length of 'primitive chain'. Adapted from Ref. [278].

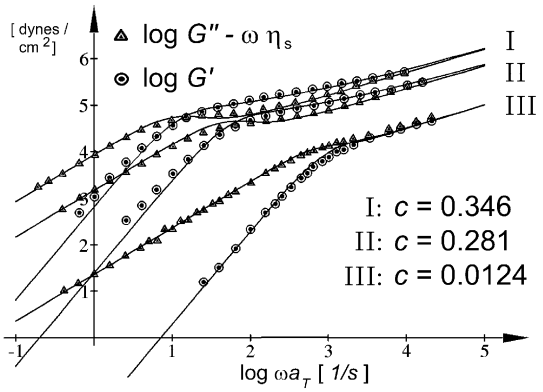

Fig. 46. Comparison between theory (Eq. (53)) and experiment (symbols) for the loss and storage moduli vs frequency for polysterene of molecular weight 267,000 dissolved in chlorinated diphenyl at the concentrations c shown (in g/cm^3) [19,282].

time-dependent alignment vector reads $\tilde{\boldsymbol{a}}(t) = \boldsymbol{C} \cdot [\tilde{\boldsymbol{a}}(t_0) + \boldsymbol{c}] - \boldsymbol{c}$ with $\boldsymbol{C} = \exp\{-\boldsymbol{M}(t - t_0)/\lambda\}$ and $\boldsymbol{c} = \boldsymbol{M}^{-1} \cdot \boldsymbol{\Theta}$. The solution can be rewritten in terms of the eigensystem of $\boldsymbol{M}$. For a case of isotropic rods, $B = 1$ at time $t_0 = 0$, the time evolution of $\tilde{\boldsymbol{a}}(t)$ is plotted in Fig. 47.

6.3.3. Example: Doi–Edwards model as a special case

We should notice, that the analytic solution (56) for isotropic chain ends ($a_{\pm}^{\text{end}} = 0$) and without orientational damping ($\tau^{-1} = 0$) provides an analytical approximation for the numerical result of the

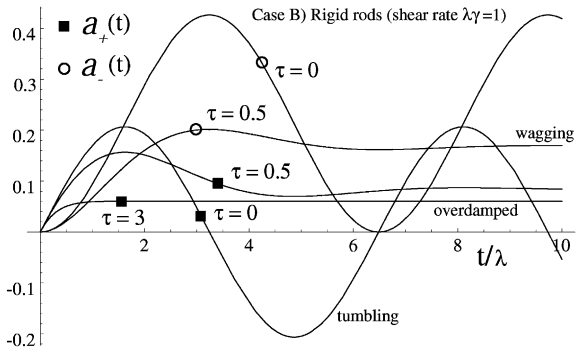

Fig. 47. A particular case of the presented analytical solution of Eq. (54) for the alignment tensor components $\boldsymbol{a}_{\pm}(t)$ of initial isotropically distributed rigid rods subjected to shear.

DE model [209,68]. Using (56) we arrive—for steady shear—at

$$a_{+} = \frac{1}{10}\dot{\gamma}\lambda B\left(\frac{\sinh x - \sin x}{\cosh x + \cos x}\right)x^{-3}, \quad x \equiv \frac{1}{\sqrt{2}}(\dot{\gamma}\lambda)^{1/2}\left(1 - \frac{3}{49}B^{2}\right)^{1/4}, \tag{57}$$

As can be seen from this expression, for low shear rates the shear alignment a_{+} increases linearly with shear rate $\dot{\gamma}$, for high rates $a_{+} \sim \dot{\gamma}^{-1/2}$ in agreement with [209]. Using the SOR, $\eta \sim a_{+}\dot{\gamma}^{-1}$ is the shear viscosity, and $\Psi_1 \sim -2a_{-}\dot{\gamma}^{-2}$ and $\Psi_2 \sim (2a_0 + a_{-})\dot{\gamma}^{-2}$ are the viscometric functions [6]. In the DE limit our approximate model yields $\Psi_2 = \Psi_1 \lim_{\dot{\gamma}\to 0}\Psi_2/\Psi_1$ and $\lim_{\dot{\gamma}\to 0}\Psi_2/\Psi_1 = 3B/14 - 1/2$, showing that Ψ_1 and Ψ_2 possess the same characteristic dependence on shear rate. The original DE model considers rod-like segments, i.e. $B = 1$, for which recover the expected and famous result $\Psi_2/\Psi_1 = -2/7$. If both the orientational diffusion constant and anisotropic tube renewal are taken into account, different power laws appear which can be used to classify the systems rheological behavior [6,209,278]. A consistent procedure is still missing to calculate the tube renewal parameter $a_{\pm}^{\text{end}}$. Fig. 48 suggests $a_{\pm}^{\text{end}}/a_{\pm}^{\text{center}} \propto \dot{\gamma}$.

6.4. Nonlinear viscoelasticity without closure, Galerkin's principle

For the three examples just discussed we started from a closed, approximate equation of change for the second rank alignment tensor, Eq. (54). We want to shortly summarize on how the underlying FP equation (49) including the effect of anisotropic tube renewal had been solved to within given precision in [283] using Galerkin's principle [6]. The same methodology had been recently used in [284] to improve on an efficient realization of the micro–macro CONNFFESSIT [285] approach for the case where a low-dimensional FP equation carrying the recommended ingredients (double reptation, convective constraint release, etc., cf. Section 6.1) is available. There are several alternative strategies. One of them is BD which we already used in the first sections (see also Section 8.5), and which should be the preferred method for solving non-trivial high dimensional FP equations [68].

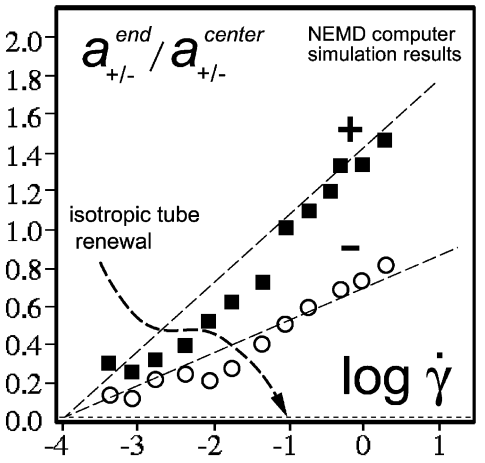

Fig. 48. A stationary, planar Couette flow with shear $\dot{\gamma}$ has been applied to a FENE model polymer melt via NEMD. The finite alignment of the end segments of polymer chains relative to the alignment of the centers of chains is shown for two components of the alignment tensor. Note that for a_+ (being closely related to the shear viscosity) the alignment of the chain ends is more pronounced than the alignment of the centers of chains at sufficiently high shear rates. The effect on the rheological quantities is important, and quantified in this paragraph.

The idea is to solve the FP equation (49) by expanding $\psi(\boldsymbol{u},\sigma)$ in spherical harmonics ψ and even Euler polynomials E [286]

$$\psi^{(M,I)}(\boldsymbol{u},\sigma) = \sum_{k=0}^{1}\sum_{n=0}^{M}\sum_{m=0}^{n}\sum_{i=0}^{I} A^i_{knm}\psi^m_{kn}(\boldsymbol{u})E_{2i}(\sigma)\,, \tag{58}$$

with $\psi^m_{0n} = P^m_n(\cos\theta)\cos\phi, \psi^m_{1n} = P^m_n(\sin\theta)\sin\phi$. Inserting the series $\psi^{(M,I)}$ into (49) and applying Galerkin's principle $\int \mathrm{d}\phi \int \mathrm{d}\theta \int \mathrm{d}\sigma\, \hat{D}[\psi^{(M,I)}]\psi^p_{lq}E_j \sin\theta = 0$, for $l = 0..1$, $q = 0..M$, $p = 0..q$, $j = 0..I$ leads to coupled linear equations for the coefficients A^i_{knm} as function of the dimensionless ratio $\varsigma = \lambda/(6\tau)$ and the dimensionless shear rate $\Gamma = \dot{\gamma}\tau$. These equations were derived in [283].

A finite bending of ψ at the chain ends (anisotropic tube renewal) is captured through a coefficient

$$x \equiv \partial^2/\partial\sigma^2 \int \psi(\boldsymbol{u},\sigma)\,\mathrm{d}^2\boldsymbol{u}|_{\sigma=0,\sigma=1} = A^2_{000}, \tag{59}$$

while we allow the integral $\int \psi(\boldsymbol{u},\sigma)\,\mathrm{d}^2\boldsymbol{u}$ to depend on σ. The normalization for ψ reads $\sum_{i=0}^{I} A^i_{000}$ $N_E(i,0)=1$, with $N_E(i,f) \equiv \int_0^1 \mathrm{d}\sigma\, E_iE_f = \alpha_{if}((i+f+2)!)^{-1}B_{i+f+2}$, involving the Bernoulli numbers B [286] and $\alpha_{if} \equiv 4(-1)^i(2^{i+f+2}-1)i!f!$. The coefficients $\forall_{n,i}A^i_{10n}$ are left undetermined in the ansatz (58). Finally there is an equal number of $(M/2+1)^2(I/2+1)$ nontrivial equations and unknowns to solve for given parameters Γ, ς and x.

The rheological behavior is inferred from the moments (or weighted moments, cf. the parameter ϵ used by Bird et al. [6] for additional 'viscous' contributions) of ψ, and had been also discussed in [283]. The effect of ratio of relaxation times ς on the alignment tensor components $a_\pm$ (for a fixed value for x), together with the corresponding components of the viscous contribution proposed by Bird et al. [6] and denoted as $k_\pm$ are shown in Fig. 49. A plateau (undershoot) in a_+ appears with

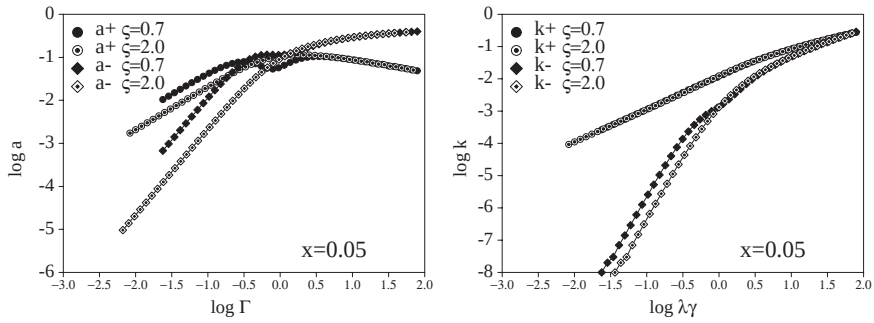

Fig. 49. Components of the dimensionless alignment quantities (left) $a_{\pm} = \langle \boldsymbol{uu} \rangle_{\pm}$ (relevant for rheological properties if the SOR is valid) and (right) $\kappa_{\pm}$ denoting a corresponding contributions to the viscous part [6] of the stress tensor $\boldsymbol{\kappa} : \langle \boldsymbol{uuuu} \rangle_{\pm}$ for selected ratios ς between orientational and reptation diffusion coefficients, and with boundary condition for the chain end $x = 0.05$ vs dimensionless shear rate $\Gamma = \dot{\gamma}\tau$.

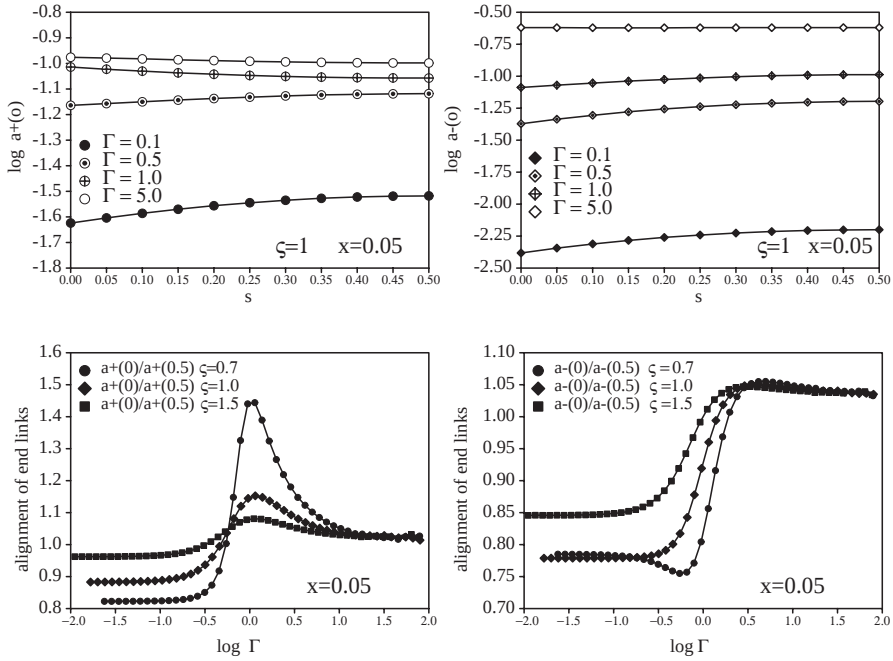

Fig. 50. The flow-alignment of segments (top left) $\log a_{+}(s)$ and (top right) $\log a_{-}(s)$ at position s within the chain and the ratios (bottom left) $a_{+}(0)/a_{+}(0.5)$ and (bottom right) $a_{-}(0)/a_{-}(0.5)$, describing the relative strength of the alignment of chain ends.

decreasing ς, and $k_{\pm}$ dominates at very high rates. The latter term can be actually used to predict a wide range of power law behaviors for the shear viscosity vs rate by varying ς. The influence of the finite bending of ψ at the chain ends, i.e. $x \neq 0$, on the alignment of segments is shown in Fig. 50. Perhaps surprising is the result for the dependence of a_{+} on the contour position. At vanishing shear rates the components $a_{\pm}$ of the symmetric traceless 2nd rank alignment tensor

vanish. At high rates the component a_+ at the ends is larger than a_+ at the chain's center, while the component a_- monotonously increases with rate—for all contour positions. The centers of the chains are more aligned in direction of flow (characterized by a_-) than the outer parts. Since the a_+-component must rise and fall with shear rate and has a maximum at a certain characteristic shear rate, the chain end will follow this behavior—just shifted to larger rates. These predictions are in very good agreement with results from NEMD of polymer melts described in Sections 4 and 6, and also illustrate why the effect of anisotropic tube renewal has an important effect on the shear viscosity (which is connected with a_+ but not with a_-).

7. Elongated particles

In [287] we provided a statistical interpretation of the director theory of Ericksen and Leslie (EL) [288–290] for nematic liquid crystals. Starting from a FP equation of the type (49) supplemented by a mean-field plus external potential, and using an expression for the stress tensor derived for structural theories of suspensions, we interpreted the EL viscosity coefficients and molecular fields in terms of the parameters characterizing a suspension, i.e., particle geometry, particle concentration, degree of alignment, solvent viscosity, and the potential. It turned out that the theory of Kuzuu and Doi [80] for concentrated suspensions of rod-like polymers, the affine transformation model by Hess and Baalss [291], the results by Hand [292] and Sin-Doo Lee [293], were contained as special cases. In distinction to Kuzuu and Doi in [287] we also obtained an expression for the tumbling parameter in terms of order parameters and particle shape, which had been confirmed independently by Archer and Larson [294]. Here, in order to review the highly coarse-grained models depicted at the top of Fig. 2 we summarize the macroscopic framework developed by EL. We give an example on how the microscopic quantities such as an anisotropic gyration tensor for polymeric chains, or the shape of suspended ellipsoidal (colloidal) particles enter the anisotropic viscosities.

There are various approaches in the literature to modeling fluids with microstructure. For example, equations for suspensions of rigid particles have been calculated by averaging the detailed motion of the individual particles in a Newtonian fluid. In particular, the solution for the motion of a single ellipsoid of revolution in a steady shear [60] can be used to determine the governing equations for the slow flow of a dilute suspension of non-interacting particles. For more concentrated systems, various approximations to the particle motions have been used. This approach, based upon a detailed analysis of the microstructure, has been called 'structural' by Hinch and Leal (HL) [61]. Alternatively, 'phenomenological' continuum theories for anisotropic fluids have been postulated. They tend to be quite general, being based upon a small number of assumptions about invariance, perhaps the most successful and well known example being the EL director theory for uniaxial nematic liquid crystals [288,289]. Additionally, numerous models have been developed and discussed in terms of symmetric second- and higher-order tensorial measures of the alignment [227,295–299,209,228,300].

Given these diverse methods of derivation and apparently diverse domains of application, one may ask, however, if and how such diverse approaches may be interrelated. Several comparisons have already been made. In particular, Hand [292] obtained the governing equations for dilute suspensions of ellipsoids of revolution without rotary diffusion and subject to no potential (thus perfectly aligned), showed that they could be modeled also by the simpler EL director theory for transversely isotropic fluids [301], and calculated the corresponding viscosities in terms of the suspension parameters.

Furthermore Marrucci [302], Semonov [303], and Kuzuu and Doi [80] related the EL theory to a dynamical mean-field theory for concentrated suspensions of rigid rods and thereby calculated the Leslie and Miesowicz viscosity coefficients in terms of the suspension parameters.

7.1. Director theory

The traditional EL theory of anisotropic fluids [288,304] assumes that there is a unit vector field $\boldsymbol{n}(\boldsymbol{x},t)$ (called the director) representing the average alignment at each point of the fluid. The extension [290] also introduces a variable degree of alignment represented by the scalar field $S(\boldsymbol{x},t)$, where $-1/2 \leqslant S \leqslant 1$. The extended EL (also denoted by EL in the following) constitutive relation for the hydrodynamic stress tensor $\boldsymbol{\sigma}$ of an incompressible anisotropic fluid with velocity $\boldsymbol{v}$ is given by the following expression linear in the nonequilibrium variables $\dot{S}, \boldsymbol{\gamma}$, and $\boldsymbol{N}$:

$$\boldsymbol{\sigma} = (\alpha_1 \boldsymbol{nn} : \boldsymbol{\gamma} + \beta_1 \dot{S})\boldsymbol{nn} + \alpha_2 \boldsymbol{nN} + \alpha_3 \boldsymbol{Nn} + \alpha_4 \boldsymbol{\gamma} + \alpha_5 \boldsymbol{nn} \cdot \boldsymbol{\gamma} + \alpha_6 \boldsymbol{\gamma} \cdot \boldsymbol{nn} \ , \tag{60}$$

where $\boldsymbol{N} \equiv \dot{\boldsymbol{n}} - \boldsymbol{\Omega} \cdot \boldsymbol{n}$, $\boldsymbol{\gamma} \equiv (\boldsymbol{\kappa} + \boldsymbol{\kappa}^\dagger)/2 = \boldsymbol{\gamma}^{\mathrm{T}}$, and $\boldsymbol{\Omega} \equiv (\boldsymbol{\kappa} - \boldsymbol{\kappa}^\dagger)/2 = -\boldsymbol{\Omega}^{\mathrm{T}}$, with $\boldsymbol{\kappa} = (\nabla \boldsymbol{v})^\dagger$. In addition to the usual balance of momentum, $\rho \dot{\boldsymbol{v}} = -\nabla_{\boldsymbol{x}} p + \nabla_{\boldsymbol{x}} \cdot \boldsymbol{\sigma}^{\mathrm{T}}$, there are two additional equations governing the microstructure: (i) a vector equation for the director $\boldsymbol{n}$ (here we neglect director inertia)

$$\boldsymbol{0} = \boldsymbol{n} \times (\boldsymbol{h}_n - \gamma_1 \boldsymbol{N} - \gamma_2 \boldsymbol{\gamma} \cdot \boldsymbol{n}) \ , \tag{61}$$

or equivalently, $\boldsymbol{0} = (\boldsymbol{1} - \boldsymbol{nn}) \cdot (\boldsymbol{h}_n - \gamma_1 \boldsymbol{N} - \gamma_2 \boldsymbol{\gamma} \cdot \boldsymbol{n})$, where $\boldsymbol{h}_n$ is the vector molecular field (which is indeterminate to a scalar multiple of $\boldsymbol{n}$); (ii) a scalar equation for the degree of alignment S (again neglecting inertia)

$$0 = h_S - \beta_2 \dot{S} - \beta_3 \boldsymbol{nn} : \boldsymbol{\gamma} \ , \tag{62}$$

where h_S is the scalar molecular field. The α_i are commonly called Leslie viscosity coefficients. The β_i were recently introduced in by Ericksen [290] for the case of variable degree of alignment. Furthermore the coefficients γ_i are related to the α_i by $\gamma_1 = \alpha_3 - \alpha_2$, $\gamma_2 = \alpha_6 - \alpha_5$. There are also two restrictions (Onsager relations) that follow from the existence of a dissipation potential: $\alpha_2 + \alpha_3 = \alpha_6 - \alpha_5$ (Parodi's relation [227]), and $\beta_1 = \beta_3$ (proposed by Ericksen). Dissipation arguments lead to the following restrictions on the coefficients [290]: $\alpha_4 \geqslant 0, \gamma_1 \geqslant 0, \beta_2 \geqslant 0, \alpha_1 + 3\alpha_4/2 + \alpha_5 + \alpha_6 - \beta_1^2/\beta_2 \geqslant 0, 2\alpha_4 + \alpha_5 + \alpha_6 - \gamma_2^2/\gamma_1 \geqslant 0$. Particular micro-based realizations of the 'macroscopic' equations will be presented next.

7.2. Structural theories of suspensions

Consider a dilute suspension of neutrally buoyant, rigid ellipsoids of revolution dispersed in an incompressible Newtonian fluid at thermal equilibrium. The governing equations can be determined from Jeffery's [60] solution for the motion of a single ellipsoid in a homogeneous shear flow. In terms of the notation of Brenner and Condiff [305], we have for the dynamic stress tensor

$$\boldsymbol{\sigma} = 2\mu_0 \boldsymbol{\gamma} + 5\mu_0 \phi \langle \boldsymbol{A} \rangle - \frac{n}{2} \epsilon \cdot \langle \boldsymbol{L} \rangle + O(\phi^2) \ , \tag{63}$$

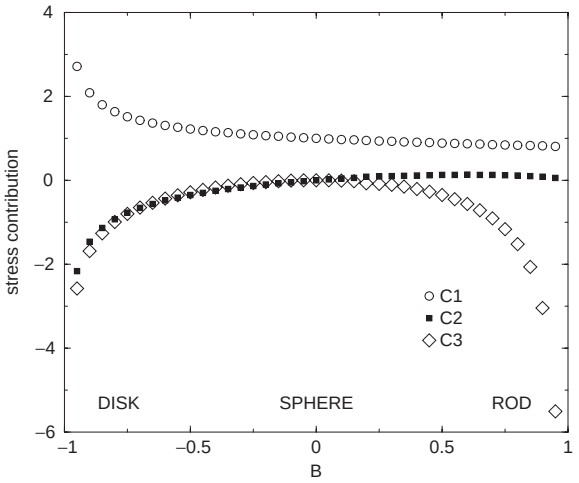

Fig. 51. Effect of particle shape on the relevance of the stress contributions for suspensions of ellipsoids of revolution, Eq. (63).

where $\boldsymbol{A}$ is the stresslet and $\boldsymbol{L}$ is the applied couple on each particle. They are given by

$$\langle \boldsymbol{A} \rangle = C_1 \boldsymbol{\gamma} + C_2(\boldsymbol{\gamma} \cdot \langle \boldsymbol{uu} \rangle + \langle \boldsymbol{uu} \rangle \cdot \boldsymbol{\gamma}) - C_3 \boldsymbol{\gamma} : \langle \boldsymbol{uuuu} \rangle + N D_r \left[\langle \boldsymbol{u} \nabla_{\boldsymbol{u}} U \rangle + \langle \nabla_{\boldsymbol{u}} U \boldsymbol{u} \rangle \right],$$

$$\langle \boldsymbol{L} \rangle = -\langle \boldsymbol{u} \times \nabla_{\boldsymbol{u}} V \rangle \ , \tag{64}$$

with the 'Brownian potential' $U \equiv \log \psi + V/k_B T$. Here, μ_0 is the Newtonian shear viscosity of the solvent, ϕ is the volume fraction of ellipsoids, n is the number density of ellipsoids, $\boldsymbol{u}$ is a unit vector along the ellipsoid axis, $\psi(\boldsymbol{u}, t)$ is the orientation distribution function, $\langle \cdot \rangle$ is the orientational average, V is an arbitrary potential, D_r is the rotary diffusion coefficient of a single ellipsoid, $B \equiv (r^2-1)/(r^2+1)$ with the axis ratio $r = a/b$ (length/width in the cross-section) of an uniaxial ellipsoid, N and $C_{..}$ (plotted in Fig. 51) are geometric coefficients as function of particle shape given in [287]. The constitutive relation (63), (64) is derived assuming a homogeneous shear flow. It can also be expected to apply for inhomogeneous flows [306]. There is also a convection–diffusion equation (of the FP type) for the orientation distribution function ψ, which allows for the calculation of the evolution of the moments of the alignment, i.e., Eq. (49) with an orienting torque due to external fields (flow plus potential)

$$\boldsymbol{T} = \boldsymbol{T}_{\text{flow}} - \frac{D_r}{k_B T} \mathscr{L} V \ . \tag{65}$$

We will make use only of the equation for the rate of change of the second-moment of the alignment $\langle \boldsymbol{uu} \rangle$. It follows directly from the FP equation:

$$\frac{\partial}{\partial t} \langle \boldsymbol{uu} \rangle = 2B \boldsymbol{\gamma} : \langle \boldsymbol{uuuu} \rangle + \boldsymbol{\Omega} \cdot \langle \boldsymbol{uu} \rangle - \langle \boldsymbol{uu} \rangle \cdot \boldsymbol{\Omega} + B(\boldsymbol{\gamma} \cdot \langle \boldsymbol{uu} \rangle + \langle \boldsymbol{uu} \rangle \cdot \boldsymbol{\gamma})$$

$$-D_r [\langle \boldsymbol{u} \nabla_{\boldsymbol{u}} U + \nabla_{\boldsymbol{u}} U \boldsymbol{u} \rangle] \ . \tag{66}$$

Furthermore, we have the following relations between the coefficients [305]: $Bck_BT = 10\mu_0 \phi N D_r$, $\phi = nv_p$, where $v_p = 4\pi ab^2/3$ is the volume of an ellipsoid. The correspondence between micro- and

macroscopic equations will be presented for a special case in Section 7.2.2. A more general case had been discussed in [287].

7.2.1. Semi-dilute suspensions of elongated particles

Batchelor [307] has calculated the effect of hydrodynamic interaction of parallel elongated particles (without Brownian motion) in a pure steady straining motion ($\boldsymbol{\Omega} = \mathbf{0}$) on the bulk stress tensor. For elongated particles of length a on which no external force or couple acts and taking up the same preferred orientation, Batchelor gave the approximate relation for the stress tensor which can be compared immediately to those of the EL theory with $\alpha_1 = 4\pi/(3V)\sum(a/2)^3/(\log h/R_0), \alpha_4 = 2\mu_0, \alpha_{2,3,5,6} = 0, S = 1$, where $\boldsymbol{n}$ is the direction of the particle axes, the sum is over the particles in the volume V, R_0 is the effective radius of the cross-section of the particle, and $h = (na)^{-1/2}$.

7.2.2. Concentrated suspensions of rod-like polymers

Doi [308] has presented a dynamical mean field theory for concentrated solutions of rod-like polymers. We follow here the version by Kuzuu and Doi [80]. Viscous contributions to the stress tensor are generally assumed negligible, but we include the viscosity μ_0 of the solvent. The stress tensor of this model formally equals expression (63) with $C_1 = C_2 = C_3 = 0$ in (64). The potential is composed of two contributions

$$V = V_m + V_e, \quad V_e = -\frac{1}{2}\chi_a(\boldsymbol{H}\cdot\boldsymbol{u})^2, \quad V_m = -\frac{3}{2}U_m k_B T\langle\boldsymbol{uu}\rangle : \overline{\boldsymbol{uu}} \ , \tag{67}$$

V_e denotes the contribution due to an induced dipole by an external field $\boldsymbol{H}$, χ_a being the anisotropic susceptibility of a rod, and V_m denotes the mean-field contribution, U_m being a constant reflecting the energy intensity of the mean field. A similar equation was also presented by Hess [309].

7.3. Uniaxial fluids, micro-macro correspondence

It is common to classify the types of alignment according to the eigenvalues of the second moment of the alignment:

$$\langle\boldsymbol{uu}\rangle = A_1\boldsymbol{ll} + A_2\boldsymbol{mm} + (1 - A_1 - A_2)\boldsymbol{nn} \ , \tag{68}$$

where $\boldsymbol{l}, \boldsymbol{m}$, and $\boldsymbol{n}$ form a triad of orthogonal unit vectors. In the special case in which the distribution of particles of the suspension in a given flow is *uniaxial*, e.g., $\psi_{\text{uni}} = \psi(|\boldsymbol{u}\cdot\boldsymbol{n}|)$, $\boldsymbol{n}(\boldsymbol{x}, t)$ denoting the axis of symmetry, one obtains that $A_1 = A_2$. Traditionally, the parameter $S_2 \equiv 1 - 3A_1$ is used. In this case, we have the following explicit relations for the second and fourth moments of the alignment [85,80]:

$$\overline{\langle\boldsymbol{uu}\rangle}_{\text{uni}} = S_2\overline{\boldsymbol{nn}} \Leftrightarrow \langle\boldsymbol{uu}\rangle_{\text{uni}} = S_2\boldsymbol{nn} + \frac{1}{3}(1 - S_2)\mathbf{1} \ , \tag{69}$$

and (in cartesian coordinates) $\langle u_i u_j u_k u_l\rangle_{\text{uni}} = S_4 n_i n_j n_k n_l + (S_2 - S_4)(\delta_{ij}n_k n_l + \delta_{ik}n_j n_l + \delta_{kj}n_i n_l + \delta_{il}n_j n_k + \delta_{jl}n_i n_k + \delta_{kl}n_i n_j)/7 + (7 - 10S_2 + 3S_4)(\delta_{ij}\delta_{kl} + \delta_{ik}\delta_{jl} + \delta_{il}\delta_{jk})/105$, where S_2 and S_4 are scalar measures of the degree of orientation related to Legendre polynomials: $S_2 = \langle P_2(\boldsymbol{u}\cdot\boldsymbol{n})\rangle$, $S_4 = \langle P_4(\boldsymbol{u}\cdot\boldsymbol{n})\rangle$. They must satisfy $-\frac{1}{2} \leqslant S_2, S_4 \leqslant 1$. In the case of perfect alignment $S_2 = S_4 = 1$, and in the case of random alignment $S_2 = S_4 = 0$. Note that the odd moments vanish identically due to symmetry

of the distribution function ψ. Similar relations hold for the higher moments, but we refrain from writing them.

The uniaxial assumption is not valid for all flows of the suspension. More generally, the alignment will be biaxial, i.e., $A_1 \neq A_2$. The biaxial case requires the use of multiple directors plus additional biaxial scalar measures (see [310] and references cited herein). For this review we are however concerned only with those flows for which this assumption holds since we want to make a comparison to the EL theory, which assumes uniaxial symmetry. In this case we need only a single unit vector plus the set $\{S_{2i}\}$ of scalars to completely describe the alignment. Furthermore, note that each even-order moment of the alignment introduces a new scalar measure of the alignment S_{2i}. The EL theory assumes that there is a closure relation so that all higher-order parameters can be expressed as a function of S_2. Such an assumption is consistent, for example, with a Gaussian distribution about the symmetry axis $\boldsymbol{n}$. However, it will not be necessary to specify any particular closure relation.

7.3.1. Application: concentrated suspensions of disks, spheres, rods

Comparing micro- (63) with macroscopic (60) stress tensors and also comparing the equation of change for the alignment tensor (66) with (61) one obtains for the particular case of concentrated suspensions of rod-like polymers, cf. Section 7.2.2, upon extending from rods ($B = 1$) to uniaxial ellipsoids also including disks ($B = -1$) and spheres ($B = 0$) the following microscopic interpretation of the EL parameters [287], with $\chi \equiv nk_BT/(2D_r)$

$$
\begin{aligned}
\alpha_1 &= -2\chi B^2 S_4 \ , \\
\alpha_2 &= -\chi B(1+\lambda^{-1})S_2 \ , \\
\alpha_3 &= -\chi B(1-\lambda^{-1})S_2 \ , \\
\alpha_4 &= 2\mu_0 + 2B^2\left(\frac{1}{5}+\frac{1}{7}S_2\right) - \eta\frac{4}{35}B^2 S_4 \ , \\
\alpha_5 &= \frac{3}{7}\chi B^2\left(S_2+\frac{4}{3}S_4\right) + \chi B S_2 \ , \\
\alpha_6 &= \frac{3}{7}\chi B^2\left(S_2+\frac{4}{3}S_4\right) - \eta B S_2 \ , \\
\beta_1 &= -\chi B \ , \\
\beta_2 &= 35\chi(21+15S_2-36S_4)^{-1} \ , \\
\beta_3 &= \beta_1 \ , \\
\gamma_1 &= \alpha_3 - \alpha_2 = 2\chi B\lambda^{-1}S_2 \ , \\
\gamma_2 &= \alpha_3 + \alpha_2 = -2\chi B S_2 \ , \\
\lambda &\equiv -\frac{\gamma_2}{\gamma_1} = \frac{\alpha_3-\alpha_2}{\alpha_3+\alpha_2} = \frac{(14+5S_2+16S_4)B}{35S_2} \ ,
\end{aligned}
\tag{70}
$$

where λ is the 'tumbling parameter'. Vector and scalar molecular fields are given by

$$\boldsymbol{n} \times \boldsymbol{h}_n = -n\langle(\boldsymbol{u} \times \nabla_{\boldsymbol{u}})V\rangle_{\text{uni}} \ ,$$

$$h_S = 35\, nk_BT\langle \boldsymbol{u}\nabla_{\boldsymbol{u}}U\rangle_{\text{uni}}(24S_4 - 10S_2 - 14)^{-1} \ . \tag{71}$$

One easily confirms that Parodi's relation and all other relationships known from the director theory (summarized in Section 7.1) are in full agreement with our micro-based expressions (70). Carlsson's conjecture [311,312] on the signs of α_2 and α_3 provided that S_2 is positive is also confirmed by (70).

7.3.2. Example: tumbling

One way to characterize materials is according to the behavior of the director in a steady shear flow. As discussed by Chandrasekhar [229] and de Gennes [227], $|\lambda| < 1$ implies that the director always tumbles in steady shear flow, whereas $|\lambda| \geqslant 1$ implies that the director has a steady solution. The above expression for the tumbling parameter λ (not provided by Kuzuu and Doi [80]) has been confirmed by Archer and Larson [294] who also took into account numerically the flow-induced biaxiality showing that there can be a modest but significant effect on the coefficient λ. Predictions (70) have been already compared with experiments [313–315], and extended to biaxial fluids [310]. A very similar expression for λ (using $S_4 \propto S_2^2$) had been derived early by Hess [81] for the case of uniaxial symmetry based on a truncation approximation to the FP equation, obtaining $\gamma_1 \propto S_2^2(1 - c_1S_2^2)$, and $\gamma_2 \propto -B\,S_2(1 + c_2S_2 - c_3S_2^2)$, where $c_{1,2,3}$ are temperature dependent constants. A typical relaxation time [316] for reorientations of the director is given by $\tau = 1/(\dot{\gamma}\sqrt{\lambda^2 - 1})$, where $\dot{\gamma}$ is the shear rate. Thus τ is seen to be a function of the order parameters and the axis ratio.

Also the coefficients α_2 and α_3 determine the type of flow via λ. For a negative product $\alpha_2\alpha_3$ (i.e., $|\lambda| < 1$) there is no steady state solution in simple shearing, for positive $\alpha_2\alpha_3$ the molecules will be aligned under shear flow, with a flow angle χ given by $\cos 2\chi = \lambda^{-1}$. In Fig. 52, we can see how the sign of $\alpha_2\alpha_3$ varies with order parameter S_2 and geometry B (using the closure relation [317] $S_4 = S_2 - S_2(1 - S_2)^{\nu}$ where $\nu = 3/5$, again there is no qualitative difference in the choice of the exponent ν). According to (70), $\lambda \to B$ when both $S_2, S_4 \to 1$. Also $\lambda \to \infty$ when both $S_2, S_4 \to 0$. Thus we will always have tumbling in the case of suspensions of almost perfectly aligned (i.e., $S_2, S_4 \approx 1$) rigid ellipsoids of revolution but steady solutions for suspensions with small degree of alignment ($S_2, S_4 \approx 0$). The transition between the two regimes is given by $|\lambda| = 1$. Note that in the case of perfect alignment (i.e., $S_2 = S_4 = 1$), (70) reduces to $\lambda = B$ and for ellipsoids of revolution we always have $|B| < 1$, which is the classical result that a single ellipsoid of revolution tumbles in steady shear flow [60,318]. Fig. 53 indicates the dependence of the tumbling of the director on the degrees of alignment S_2 and S_4. These results are independent of the particular potential, thus apply also to mean-field theory.

The calculated viscosity coefficients in (70) are subject to the restrictions given in Section 7.1. From (70) it follows that $\beta_2 \geqslant 0$ if and only if $S_4 \leqslant (5S_2 + 7)/12$, which excludes arbitrary pairs of values for S_2 and S_4. The excluded region is shown in Fig. 53. The remaining inequalities are automatically satisfied when $\beta_2 \geqslant 0$.

7.3.3. Example: Miesowicz viscosities

It is common to measure the three Miesowicz viscosities η_i, $i = 1, 2, 3$ defined as the ratio of the yx-component of the stress tensor and the shear rate $\dot{\gamma}$. The label $i = 1, 2, 3$ refers to the cases where

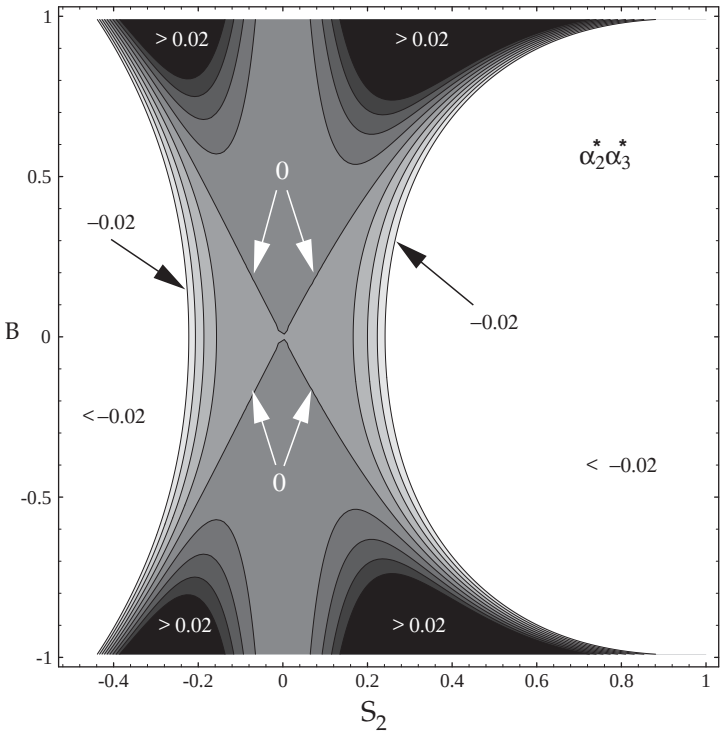

Fig. 52. Contour plot of $\alpha_2\alpha_3$ as a function of geometry B and order parameter S_2. Positive region corresponds to tumbling regimes, negative region to steady flow alignment. The dimensionless viscosities are defined by $\alpha_i^* := \alpha_i D_r/(ck_BT)$.

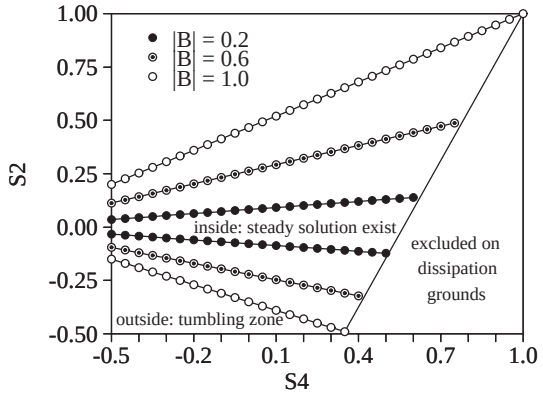

Fig. 53. The existence of steady solutions for the director in shear flow depends upon the geometric coefficient B of the ellipsoids and the degrees of alignment S_2 and S_4. The boundary between tumbling/nontumbling (see text) is plotted. As shown in this section, some combinations of S_2 and S_4 are excluded on dissipation grounds [287].

the director $\boldsymbol{n}$ is parallel to the x-, y-, z-axis, respectively (cf. Fig. 54). An orienting (magnetic) field has to be strong enough to overcome the flow induced orientation. A fourth coefficient η_4 with $\boldsymbol{n}$ parallel to the bisector between the x- and y-axes is needed to characterize the shear viscosity

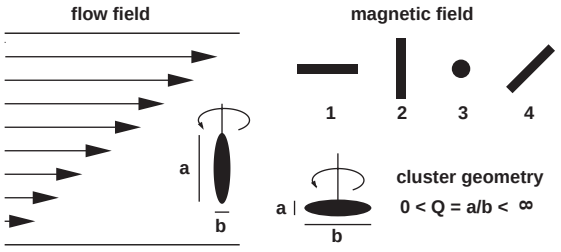

Fig. 54. For the measurement of the Miesowicz viscosities $\eta_{1,2,3}$ and the viscosity η_4 the magnetization-induced by the external magnetic field has to point in flow ($1 = x$), flow gradient ($2 = y$), vorticity ($3 = z$) direction. The ellipsoids of revolution considered within the FP approach in this review are characterized by a single shape factor $-1 < B < 1$ where $B > 0$ and $B < 0$ for rodlike and dislike aggregates, respectively.

completely. Instead of η_4, the Helfrich viscosity coefficient $\eta_{12} = 4\eta_4 - 2(\eta_1 + \eta_2)$ is used in addition to the Miesowicz coefficients. The 'rotational' viscosity γ_1 can be measured via the torque exerted on a nematic liquid crystal in the presence of a rotating magnetic field (Tsvetkov effect). The four effective viscosities measurable in a flow experiment, cf. Fig. 54, are related to the EL viscosity coefficients by $\eta_1 = (\alpha_4 + \alpha_6 + \alpha_3)/2, \eta_2 = (\alpha_4 + \alpha_5 - \alpha_2)/2, \eta_3 = \alpha_4/2, \eta_{12} = \alpha_1$. Explicit expression for these quantities are obtained by inserting the viscosity coefficients from (70).

7.4. Uniaxial fluids: decoupling approximations

In this section we briefly comment on the validity of closure schemes often used in the literature, in particular the so-called Hinch and Leal (HL) closures. They have been used to close the infinite number of coupled equations of motion for alignment tensors, derived from the FP equation such as (49). Here we wish to point out that for the case of uniaxial symmetry there is a single possible closure which requires the knowledge of a scalar function $S_4(S_2)$ rather than a full tensorial relationship, and we will show, that this closure is different from the HL closures.

For systems composed of uniaxial-shaped particles with symmetry axis $\boldsymbol{u}$, the tensorial second- and fourth-order moments of the (non-anisotropic) alignment are denoted by $\boldsymbol{a}_2 = \langle \boldsymbol{uu} \rangle$, $\boldsymbol{a}_4 = \langle \boldsymbol{uuuu} \rangle$, where $\langle \cdot \rangle$ is an orientational average. As shown before in this review it is often convenient to use alternative but equivalent tensorial measures that are symmetric in all indices and traceless when contracted over any pair of indices. We denoted such alignment tensors with the '$\sqcap$' symbol. For the second and fourth order moments $\boldsymbol{a}_2$ and $\boldsymbol{a}_4$ one explicitly has $\overline{\boldsymbol{a}_2} = \boldsymbol{a}_2 - \boldsymbol{I}/3$, and

$$\overline{\boldsymbol{a}_4} = \boldsymbol{a}_4 - \frac{6}{7}\{\boldsymbol{a}_2\boldsymbol{I}\}_{\mathrm{sym}} + \frac{3}{35}\{\boldsymbol{I}\,\boldsymbol{I}\}_{\mathrm{sym}}\ , \tag{72}$$

respectively, where $\{\cdot\}_{\mathrm{sym}}$ denotes a symmetrized expression defined by $\{X_{\mu\nu}Y_{\kappa\lambda}\}_{\mathrm{sym}} \equiv 6^{-1}(X_{\mu\nu}Y_{\kappa\lambda} + X_{\mu\kappa}Y_{\nu\lambda} + X_{\mu\lambda}Y_{\kappa\lambda} + X_{\nu\kappa}Y_{\mu\lambda} + X_{\nu\lambda}Y_{\mu\kappa} + X_{\kappa\lambda}Y_{\mu\nu})$ for the dyadic product of symmetric tensors $\boldsymbol{X}$ and $\boldsymbol{Y}$. At this point the reader may convince himself that the rhs of (72) is symmetric and traceless by rewriting these equations for nine components. Such an exercise helps interpreting the following (very simple) equations efficiently. There are orthogonal unit vectors $\boldsymbol{n}$, $\boldsymbol{m}$, $\boldsymbol{l}$ such that $\boldsymbol{a}_2 = \lambda_1\boldsymbol{n} + \lambda_2\boldsymbol{m}\,\boldsymbol{m} + \lambda_3\boldsymbol{l}\boldsymbol{l}$. The λ_i are the principal values of $\boldsymbol{a}_2$, and the unit vectors $\boldsymbol{n}$, $\boldsymbol{m}$ and $\boldsymbol{l}$ are the principal directions. The λ_i are subject to the constraint $\mathrm{Tr}\,\overline{\boldsymbol{a}}_2 = 0$, i.e. $\sum_i \lambda_i = 1$. Similar relations hold for alignment

tensors of arbitrary orders. The symmetry of orientational distribution f which defines the moments (alignment tensors) $\overline{\boldsymbol{a}_i}$ is directly reflected by the number of distinct principal values. For example, for the second-order moment $\boldsymbol{a}_2$, we have 1, 2 and 3 distinct principal value(s) for isotropic, uniaxial, and biaxial symmetry, respectively. Let us summarize some trivial implications.

(i) Isotropic symmetry: $\lambda_{1,2,3} = 1/3, \boldsymbol{a}_2 = \boldsymbol{I}/3, \overline{\boldsymbol{a}}_2 = \boldsymbol{0}, \boldsymbol{a}_4 = \{\boldsymbol{II}\}_{\mathrm{sym}}/5, \overline{\boldsymbol{a}_4} = \boldsymbol{0}$. Any closure relation for $\boldsymbol{a}_4$ in terms of $\boldsymbol{a}_2$ which should at least be non-violated close to equilibrium (if isotropic) must therefore fulfill the relationship $\boldsymbol{a}_4 = (9/5)\{\boldsymbol{a}_2\boldsymbol{a}_2\}_{\mathrm{sym}}$ which is, in particular, incompatible with the closure $\boldsymbol{a}_4 = \boldsymbol{a}_2\boldsymbol{a}_2$.

(ii) Uniaxial symmetry: Two of the principal values of the second-order alignment tensor are equal (say $\lambda_2 = \lambda_3$). In this case we can write $\boldsymbol{a}_2 = S_2\boldsymbol{nn} + (1 - S_2)\boldsymbol{I}/3$, $\overline{\boldsymbol{a}_2} = S_2\,\overline{\boldsymbol{nn}}$, with an order parameter $S_2 \equiv (3\lambda_1 - 1)/2$. The fourth-order moments are given by $\overline{\boldsymbol{a}_4} = S_4\,\overline{\boldsymbol{nnnn}}$, and

$$\boldsymbol{a}_4 = S_4\boldsymbol{nnnn} + \frac{6}{7}(S_2 - S_4)\{\boldsymbol{Inn}\}_{\mathrm{sym}} + \frac{1}{35}(7 - 10S_2 + 3S_4)\{\boldsymbol{II}\}_{\mathrm{sym}} \ . \tag{73}$$

Here S_2 and S_4 are the uniaxial scalar order parameters. They are related to the particle orientations by averages of Legendre polynomials: $S_2 = \langle P_2(\boldsymbol{u}\cdot\boldsymbol{n})\rangle, S_4 = \langle P_4(\boldsymbol{u}\cdot\boldsymbol{n})\rangle$, and range in value by $-1/2 \leqslant S_2 \leqslant 1, -3/8 \leqslant S_4 \leqslant 1$. The principal direction $\boldsymbol{n}$ is called the uniaxial director. As for the isotropic case, both anisotropic moments $\overline{\boldsymbol{a}}_2$ and $\overline{\boldsymbol{a}}_4$ are formally 'simpler' to handle than $\boldsymbol{a}_2$ and $\boldsymbol{a}_4$.

7.4.1. Decoupling with correct tensorial symmetry

Substitution of $\boldsymbol{nn}$ in terms of $\boldsymbol{a}_2$ and S_2 into (73) yields

$$S_2^2\,\overline{\boldsymbol{a}}_4 = S_4\,\overline{\overline{\boldsymbol{a}_2}\ \overline{\boldsymbol{a}_2}} \ . \tag{74}$$

No assumption has been made other than uniaxial symmetry, so that this tensorial closure relationship is *exact* for uniaxial and isotropic symmetry, but carries still unspecified scalar order parameters S_2, S_4. Obviously, there is not such a simple analog for the biaxial case.

Based on the above representations of the second- and fourth-order alignment tensors, we now consider possible closure schemes for $\boldsymbol{B} : \boldsymbol{a}_4$ with $\boldsymbol{B}$ an arbitrary symmetric and traceless tensor. such a closure is needed, e.g. in (66) to derive a closed form nonlinear equation for the second moment.

Two more commonly cited closures, motivated by HL [319], are the HL1 closure:

$$\boldsymbol{B} : \boldsymbol{a}_4 = \frac{1}{5}(6\boldsymbol{a}_2\cdot\boldsymbol{B}\cdot\boldsymbol{a}_2 - \boldsymbol{B}:\boldsymbol{a}_2\boldsymbol{a}_2 + 2\boldsymbol{I}(\boldsymbol{a}_2 - \boldsymbol{a}_2\cdot\boldsymbol{a}_2):\boldsymbol{B}) \ , \tag{75}$$

and HL2 closure:

$$\begin{aligned}\boldsymbol{B} : \boldsymbol{a}_4 = {} & \boldsymbol{B}:\boldsymbol{a}_2\boldsymbol{a}_2 + 2\boldsymbol{a}_2\cdot\boldsymbol{B}\cdot\boldsymbol{a}_2 - \frac{2\boldsymbol{a}_2\cdot\boldsymbol{a}_2:\boldsymbol{B}}{\boldsymbol{a}_2:\boldsymbol{a}_2}\,\boldsymbol{a}_2\cdot\boldsymbol{a}_2 \\ & + \exp\left\{\frac{(2 - 6\boldsymbol{a}_2:\boldsymbol{a}_2)}{(1 - \boldsymbol{a}_2:\boldsymbol{a}_2)}\right\}\left[\frac{52}{315}\boldsymbol{B} - \frac{8}{21}(\boldsymbol{B}\cdot\boldsymbol{a}_2 + \boldsymbol{a}_2\cdot\boldsymbol{B} - \frac{2}{3}\boldsymbol{B}:\boldsymbol{a}_2)\,\boldsymbol{I}\right] \ .\end{aligned} \tag{76}$$

These are based on interpolation between weak and strong flow limits in a Brownian suspension of rods. For closure (74), which is exact for the case of uniaxial symmetry, and relies only on an approximation between scalar quantities S_4 and S_2, we obtain by straightforward calculation, for the

special case $S_4 = S_2^2$, which fulfills $S_4 = 0 \leftrightarrow S_2 = 0$ and $S_4 = 1 \leftrightarrow S_2 = 1$ and is the only consistent one which is parameter-free: KS1 closure:

$$\boldsymbol{B} : \boldsymbol{a}_4 = \frac{1}{105}\{2\boldsymbol{B} - 10(\boldsymbol{B}\cdot\boldsymbol{a}_2 + \boldsymbol{a}_2\cdot\boldsymbol{B}) + 35\boldsymbol{B} : \boldsymbol{a}_2\boldsymbol{a}_2 - 20(\boldsymbol{B}\cdot\boldsymbol{a}_2\cdot\boldsymbol{a}_2 + \boldsymbol{a}_2\cdot\boldsymbol{a}_2\cdot\boldsymbol{B}) + 70\boldsymbol{a}_2\cdot\boldsymbol{B}\cdot\boldsymbol{a}_2 + 4\boldsymbol{B}\boldsymbol{a}_2 : \boldsymbol{a}_2 - 5\boldsymbol{I}(\boldsymbol{a}_2 : \boldsymbol{B} + 2\,\mathrm{Tr}[\boldsymbol{B}\cdot\boldsymbol{a}_2\cdot\boldsymbol{a}_2])\}\ . \tag{77}$$

All the above closures (HL1,HL2,KS1) correctly reduce to the expected $2\boldsymbol{B}/15$ and $\boldsymbol{B} : \boldsymbol{nnnn}$ for isotropic symmetry ($\boldsymbol{a}_2 = \boldsymbol{I}/3$) and perfect uniaxial alignment ($\boldsymbol{a}_2 = \boldsymbol{n}$), respectively. In order to compare these closures one can plot the nonvanishing components of the quantity $\boldsymbol{B} : \boldsymbol{a}_4$ vs the amplitude A of $\boldsymbol{B}$, where $\boldsymbol{B}$ has the following form $\boldsymbol{B}=A((2-a-2b,b,0),(b,b-1,0),(0,0,a+b-1))$. For the (relevant) case that $\boldsymbol{B}$ represents a traceless velocity gradient, and the prefactor a flow rate, the choices $a = 0, b = 1$ and $a = b = 0$ characterize shear (A: shear rate) and uniaxial elongational (A: elongation rate) flow fields, respectively. As for the HLx closures, $\mathrm{Tr}(\boldsymbol{B} : \boldsymbol{a}_4) = \boldsymbol{B} : \boldsymbol{a}_2$ holds for (77). Any reasonable closure specified by S_4 in terms of S_2 (for 'conventional fluids' with positive order parameters) should at least satisfy $0 < S_4 < S_2$. For example, the ansatz $S_4 = S_2 - S_2(1 - S_2)^v$ parameterized by $0 < v < 1$ has been proposed in [317], the corresponding closures are called KSv-closures, and contain the KS1 closure as a special case. The HLx closures, however, allow to produce pairs S_2, S_4 which fall outside this regime. The closure (74), which is immediately extended to higher order tensors, may be preferred if one wants to keep the exact tensorial symmetry while performing a closure relationship between (only) two scalar quantities for a closure involving $\boldsymbol{a}_4$ and, in general, n scalar functions for a closure involving $\boldsymbol{a}_{2n}$.

7.5. Ferrofluids: dynamics and rheology

Ferrofluids containing spherical colloidal particles with a permanent ferromagnetic core have been modeled by a system composed of ellipsoidal aggregates (transient chains) along the lines indicated in the previous sections [320,100,321]. The stress tensor of this model equals expression (63). The FP equation for the orientation distribution function is given by (49) with orienting torque (65). The potential V_μ for a magnetic moment $\boldsymbol{\mu} = \mu\boldsymbol{u}$ in the local magnetic field $\boldsymbol{H}$ is given by $-\beta V_\mu = \beta\mu\boldsymbol{H}\cdot\boldsymbol{u} = \boldsymbol{h}\cdot\boldsymbol{u}$, with $\beta = 1/(k_BT)$. Hereby the dimensionless magnetic field $\boldsymbol{h} = \mu\boldsymbol{H}/k_BT$ and its amplitude h (Langevin parameter) are introduced. For spheres, $B = 0$, the FP equation reduces to the kinetic equation for dilute ferrofluids developed in Ref. [322]. The equilibrium magnetization directly obtained from the equilibrium distribution of the FP equation is $\boldsymbol{M}_{\mathrm{eq}} = n\mu\langle\boldsymbol{u}\rangle_{\mathrm{eq}} = n\mu L(h)\boldsymbol{h}/h$, where $L(x) \equiv \coth(x) - 1/x$ is the Langevin function. This equilibrium magnetization is the classical result for a system of noninteracting magnetic dipoles. The equation for the first moment, i.e., the magnetization, is derived from the FP equation ((49) with $V = V_\mu$)

$$\partial_t\langle\boldsymbol{u}\rangle = \boldsymbol{\omega}\times\langle\boldsymbol{u}\rangle + B\langle(\boldsymbol{I} - \boldsymbol{uu})\boldsymbol{u}\rangle{:}\boldsymbol{\gamma} - \frac{1}{\tau}\langle\boldsymbol{u}\rangle + \frac{1}{2\tau}(\boldsymbol{I} - \langle\boldsymbol{uu}\rangle)\cdot\boldsymbol{h}\ . \tag{78}$$

The one for the second is given in [100]. Using these equations of change, the explicit contribution of the potential V_μ to the full stress tensor can be eliminated. In particular, one obtains for the

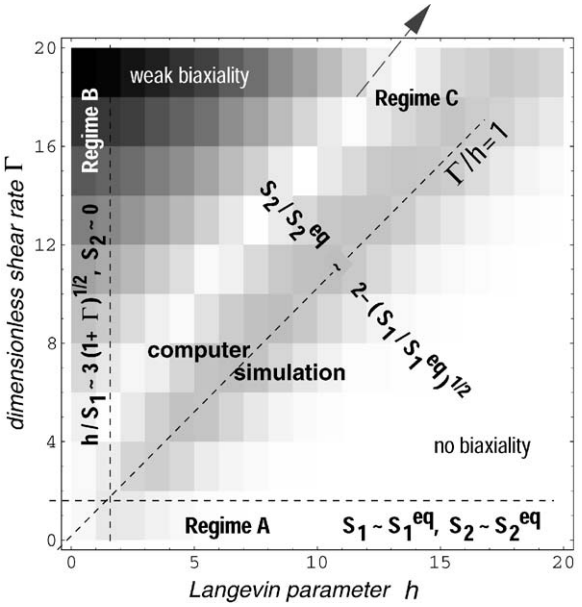

Fig. 55. The shaded background represents a measure for the (minor) relevance of biaxiality—obtained via NEBD—on the prediction of the rotational viscosity γ_1 as function of dimensionless magnetic field h and vorticity $\tau\dot{\gamma}$ [100]. Shading ranges from white (uniaxial) to black. In the top left corner (data for $\tau\dot{\gamma} = 10,\ h = 1$) we have a 1.2% relative deviation between uniaxial and biaxial formulas for γ_1. The depicted regimes refer to analytical solutions of the FP equation. A: weak magnetic field, B: weak flow field, C: deterministic limit. The figure summarizes analytical as well as approximative results for these regimes. Adapted from Ref. [320].

antisymmetric part of the stress tensor $\boldsymbol{\sigma}^a$, upon inserting the following result:

$$\boldsymbol{h} = \tau\boldsymbol{\Pi}^{-1} \cdot \left(\partial_t\langle\boldsymbol{u}\rangle - \boldsymbol{\omega}\times\langle\boldsymbol{u}\rangle - B[\boldsymbol{\gamma}\cdot\langle\boldsymbol{u}\rangle - \langle\boldsymbol{uuu}\rangle{:}\boldsymbol{\gamma}] + \tau^{-1}\langle\boldsymbol{u}\rangle\right) \ , \tag{79}$$

where $\boldsymbol{\Pi}^{-1}$ denotes the inverse of the matrix $\boldsymbol{\Pi} \equiv (\boldsymbol{I} - \langle\boldsymbol{uu}\rangle)$, an expression in terms of the moments alone: $\boldsymbol{\sigma}^{\mathrm{a}} = -\gamma_1(\boldsymbol{N}\times\boldsymbol{nn}) - \gamma_2(\boldsymbol{\gamma}\cdot\boldsymbol{nn})\times\boldsymbol{nn}$ with the viscosity coefficients $\gamma_1 \propto (3S_1^2)/(2+S_2), \gamma_2 \propto -B\{3S_1(3S_1+2S_3)\}/\{5(2+S_2)\}$, and a shape-dependent proportionality coefficient [321]. By performing NEBD simulation [100] for this system it had been observed that the assumption of uniaxial symmetry can be successfully applied in a wide regime of shear rates and magnetic fields, see Fig. 55 for an schematic overview. This figures also summarizes (closure) relationships between the order parameters for different regimes. In Ref. [323] the stationary and oscillatory properties of dilute ferromagnetic colloidal suspensions in plane Couette flow were studied. Analytical expressions for the off-equilibrium magnetization and the shear viscosity are obtained within the so-called effective field approximation (EFA), and the predictions of a different approximation based on the linearized moment expansion (LME) were obtained. Direct NEBD simulation of the FP equation were performed in order to test the range of validity of these approximations. It turns out that both EFA and LME provide very good approximations to the stationary off-equilibrium magnetization as well as the stationary shear viscosity in case of weak Couette flow if the magnetic field is oriented in gradient direction. If the magnetic field is oriented in flow direction, and for small amplitude oscillatory Couette flow, the LME should be favored. A sample result which estimates the quality

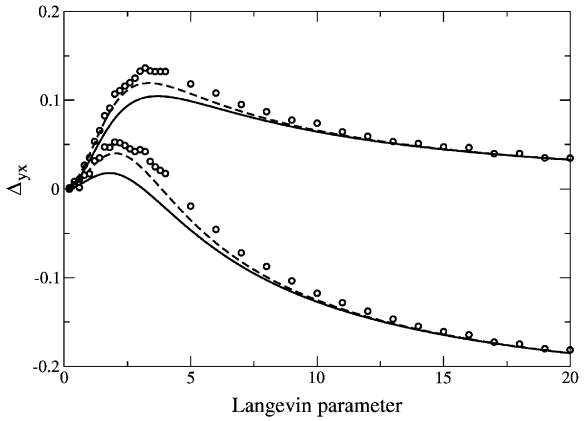

Fig. 56. Stationary relative change Δ_{yx} of the shear viscosity for a dilute suspension of ferromagnetic particles, cf. Section 7.5, in plane Couette flow as a function of the Langevin parameter h. The magnetic field was oriented in flow direction, dimensionless shear rate $\dot{\gamma} = 0.1$. Symbols represent the result of the NEBD simulation, full line correspond to the EFA, dashed line to the LME approximation. The value of the axis ratio of the ellipsoid was chosen as $r = 2(B = 3/5)$ for the lower and $r = 5(B = 12/13)$ for the upper curves. Adapted from Ref. [323].

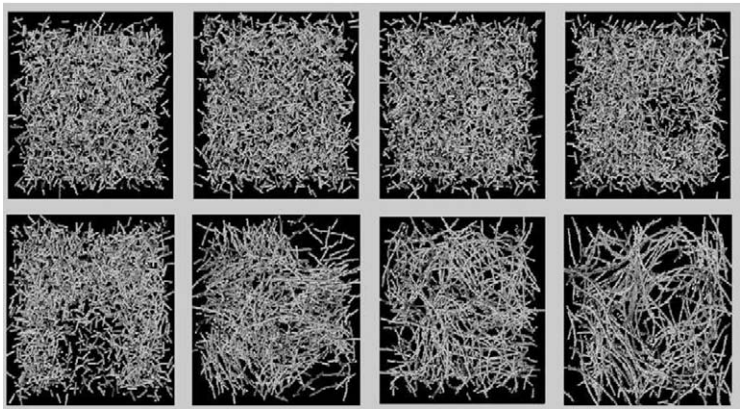

Fig. 57. Sample MD snapshot for a simple ferrofluid with increasing (top left to bottom right) permanent magnetic moment, where external orienting (flow, magnetic) fields are absent. The figure serves to demonstrate, that ferrofluids exhibit anisotropic viscosities even in the absence of a magnetic field (due to chain formation), and that they can be modeled with a combination of the methods presented for colloidal suspensions and FENE-C wormlike micelles.

of the approximations is given in Fig. 56. Fig. 57 provides a sample time series for a ferrofluid we obtained via MD for a collection of (LJ) repulsive freely rotating permanent magnetic dipoles. Here, it is illustrated why ferrofluids exhibit anisotropic viscosities even in the absence of a magnetic field: often due to chain formation. Not just chains, but other types of agglomerates have been observed via MD as well. Also antiferromagnetic phases belong to this class. This phase can be stabilized if attractive (LJ) interactions—beside dipolar interactions—are present.

7.6. Liquid crystals: periodic and irregular dynamics

Detailed theoretical studies [325,326], based on solutions of a generalized FP equation [81,308], revealed that in addition to the tumbling motion, wagging and kayaking types of motions, as well as combinations thereof occur. Recently, also chaotic motions were inferred from a moment approximation to the same FP equation leading to a 65-dimensional dynamical system [327] for uniaxial particles. While we are going to consider uniaxial particles (following [324]) one may notice that for long triaxial ellipsoidal non-Brownian particles chaotic behavior had been also predicted in [328]. Point of departure is the following equation of change for the alignment tensor (notice the similarity with Eq. (54))

$$\tau_a(\partial \boldsymbol{a}/\partial t - 2\overline{\omega \times \boldsymbol{a}}) + \boldsymbol{\Phi}(\boldsymbol{a}) = -\sqrt{2}\tau_{\mathrm{ap}}\boldsymbol{\gamma} \ . \tag{80}$$

The quantity $\boldsymbol{\Phi}$ is the derivative of a Landau–de Gennes free energy Φ, Eq. (81) below, with respect to the alignment tensor. It contains terms of first, second, and third order in $\boldsymbol{a}$. The equation stated here was first derived within the framework of irreversible thermodynamics [296,297], where the relaxation time coefficients $\tau_a > 0$ and τ_{ap} are considered as phenomenological parameters, for their microscopic interpretation see Section 7. Eq. (80) can also be derived, within certain approximations [329], from the FP used there. Then τ_a and the ratio $-\tau_{\mathrm{ap}}/\tau_a$ are related to the rotational diffusion coefficient D_r and to a nonsphericity parameter associated with the shape B of a particle. Eq. (80) is applicable to both the isotropic and the nematic phases. Limiting cases that follow from this equation are the pretransitional behavior of the flow birefringence [309,330] in the isotropic phase and the EL theory (Section 7.1) in the uniaxial nematic phase. Eq. (80) has been discussed intensively in recent, in particular experimental, works, see e.g. [197,331] and references cited herein.

7.6.1. Landau–de Gennes potential

The five components a_i of $\boldsymbol{a}$—relative to the symmetry-adapted basis system (8), (9)—are expressed in units of the magnitude of the equilibrium alignment at the temperature (or concentration) where the nematic phase of a lyotropic LC coexists with its isotropic phase. In its dimensionless form the Landau–de Gennes free energy invokes a single model parameter ϑ, viz.,

$$2\Phi = \vartheta \boldsymbol{a}^2 - 2I^{(3)} + \boldsymbol{a}^4, \quad I^{(3)} = \sqrt{6}\,\mathrm{tr}(\boldsymbol{a}\cdot\boldsymbol{a}\cdot\boldsymbol{a}) \ . \tag{81}$$

Here $I^{(3)}$ is the third order scalar invariant. The dynamical system (80) has been rewritten in terms of the a_i's in [329] and contains three control parameters two of which are determined by the state point and the material chosen, the third control parameter is a dimensionless shear rate $\Gamma \propto \dot{\gamma}$ [332]. Eq. (80) with $a_{3,4} = 0$ describes correctly the flow aligned state as well as the tumbling and wagging behavior of the full system for certain ranges of control parameters, see [329] for a detailed analysis. Here we wish focus on the symmetry breaking solutions with $a_{3,4} \neq 0$. These solutions are associated with kayaking types of motions, but also rather complex and chaotic orbits are found. We use a fourth-order Runge–Kutta method with fixed time step to solve the dynamic system (Fig. 58).

7.6.2. In-plane and out-of-plane states

A solution phase diagram of the various in-plane and out-of-plane states is drawn for $\vartheta = 0$ in Fig. 59, in its caption we introduce abbreviations for the types of orbits. The three orbits, T, W, A

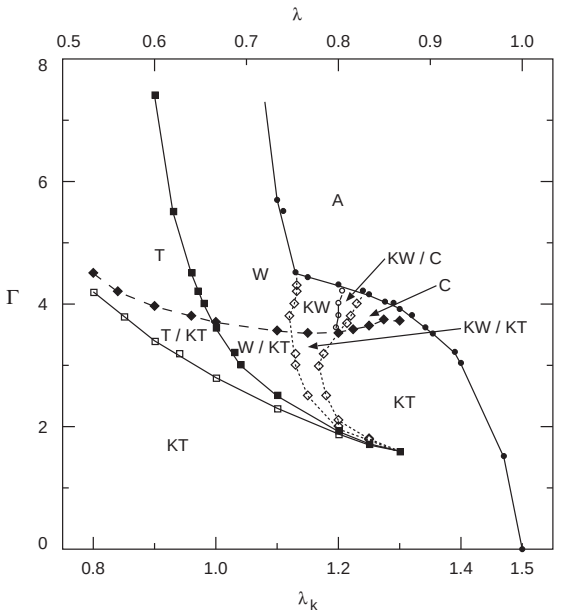

Fig. 58. Solution phase diagram of the steady and transient states of a liquid crystal modeled by the FP equation (49) supplemented by the Landau–de-Gennes potential, Eq. (81) with $\vartheta = 0$. The solid line is the border between the in-plane orbits T(umbling), W(agging) and A(ligned); the dashed line and the dotted line delimit the regions where the out-of-plane orbits K(ayaking)T and KW, respectively, exist. Here Γ, λ, and λ_k denote dimensionless shear rate Γ, tumbling parameter of the EL theory, and $\lambda_k = \sqrt{5}\lambda S_2^{\mathrm{eq}}$ where $S_2^{\mathrm{eq}} = \lim_{\Gamma\to 0} S_2$ is an equilibrium order parameter. Adapted from Ref. [324].

were identified in [329]. The kayaking orbits [325,326], KT and KW, are distinguished from each other according to Ref. [333]. Because the physical situation is invariant under the transformation $a_{3,4} \to -a_{3,4}$, two equivalent kayaking states exist. The system shows rather complicated dynamical behavior in region C of the solution diagram where neither one of the simple periodic states nor an aligning state is stable. The specific orbits had been classified in [324] as (i) Periodic KT/KW composite states where the KW sequences are damped with increasing shear rate; (ii) Irregular KT or KT/KW states for which the largest Lyapunov exponent is of order $0.01 \ldots 0.05$; (iii) Intermittent KT, and (iv) Period doubling KT states. The route to chaos for increasing shear rates had been found to depend on the tumbling parameter. When the flow-aligned (A) phase is approached from the complex (C) regime, the oscillation period grows infinitely high, in contrast to the behavior at the KW $\to$ A transition, where the amplitude of the oscillation gets damped. The resulting bifurcation plot has a striking similarity to the Feigenbaum diagram of the logistic map, $x_{n+1} = r x_n(1 - x_n)$. The distance between successive period doubling steps in Fig. 59 shrinks rapidly with the order of the period as in the Feigenbaum diagram. Even the chaotic region exhibits the same type of banded structure and has windows of periodic behavior. However, at $\Gamma \approx 3.748$, the chaotic band enlarges abruptly. The reason for this behavior is the equivalence of the states $a_{3,4}$ and $-a_{3,4}$. To test the similarity of the period doubling routes, the values Γ_n where a period of order 2^n emerges and the value Γ_∞ for the beginning of chaos were calculated in [324] for $n = 1 \ldots 5$. Like for the logistic map, the Γ_n scale according to a law $\Gamma_n = \Gamma_\infty - C\,\delta^{-n}$ for $n \gg 1$, with the Feigenbaum constant δ.

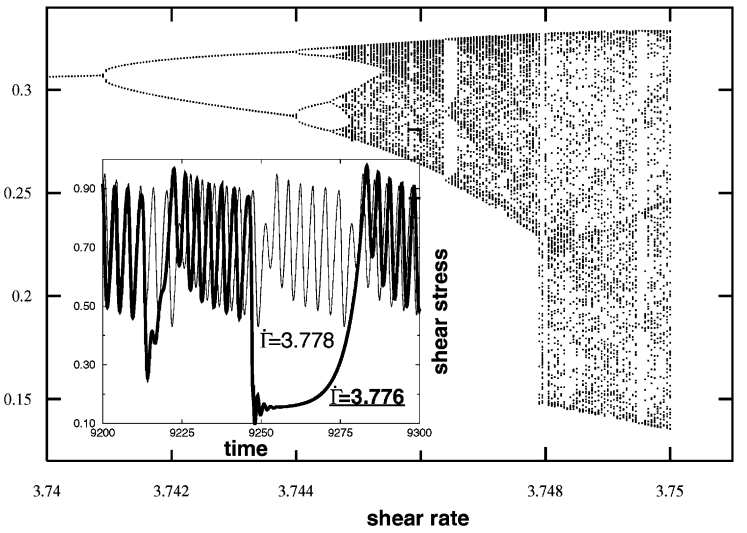

Fig. 59. Feigenbaum diagram of the period doubling route (same system as for Fig. 58), for the particular shear rate $\Gamma = 3.74 \ldots 3.75$. Plot of the Poincaré map $a_4(t_i)$ for $i = 1 \ldots 82$ at $a_3 = 0$ vs the 'control parameter' Γ, the dimensionless shear rate. The a_i's denote components of the alignment tensor with respect to the symmetry adapted set of basis tensors (8), (9). The inset shows the shear stress vs time for two fixed shear rates, $\Gamma = 3.778$ (thin line), and $\Gamma = 3.776$ (thick line), where the latter case exemplifies transient, rheochaotic behavior. All quantities in dimensionless units. Adapted from Ref. [324].

For our problem, a nonlinear fit yields $\delta = 4.83 \pm 0.02$. The value agrees qualitatively with that for the logistic map. $\delta = 4.669 \ldots$, and a similar value had been reported in [327]. Irregular behavior of the alignment tensor $\boldsymbol{a}$ immediately converts into irregular behavior for rheological properties, cf. Fig. 59 for an example. Based on the findings reported here, the inhomogeneous extension [299,334,335] of the present model can be expected to be of relevance in describing experimentally observed instabilities, irregular banded and striped textures [336–339].

8. Connection between different levels of description

8.1. Boltzmann equation

One of the major issues raised by the Boltzmann equation is the problem of the reduced description. Equations of hydrodynamics constitute a closet set of equations for the hydrodynamic field (local density, local momentum, and local temperature). From the standpoint of the Boltzmann equation, these quantities are low-order moments of the one-body distribution function, or, in other words, the macroscopic variables. The problem of the reduced description consists in deriving equations for the macroscopic variables from kinetic equations, and predicting conditions under which the macroscopic description sets in. The classical methods of reduced description for the Boltzmann equation are: the Hilbert method, the Chapman–Enskog method, and the Grad moment method, reviewed in [4]. The general approach to the problem of reduced description for dissipative system was recognized as the problem of finding stable invariant manifolds in the space of distribution function. The notion

of invariant manifold generalizes the normal solution in the Hilbert and in the Chapman–Enskog method, and the finite-moment sets of distribution function in the Grad method. A generalization of the Grad moment method is the concept of the quasiequilibrium approximation, cf. Section 2.6 and Refs. [4,97]. Boltzmann's kinetic equation has been expressed in GENERIC form [340], cf. Section 8.3, demonstrating that no dissipative potential is required for representing these equations.

8.2. Generalized Poisson structures

A similar formal structure, namely a symplectic structure, for thermodynamics and classical mechanics has been noted early, e.g., by Peterson in his work about the analogy between thermodynamics and mechanics [62]. Peterson notes the equations of state—by which he means identical relations among the thermodynamic variables characterizing a system—are actually first-order partial differential equations for a function which defines the thermodynamics of the system. Like the Hamilton–Jacobi equation, such equations can be solved along trajectories given by Hamilton's equations, the trajectories being quasistatic processes which obey the given equation of state. This gave rise to the notion of thermodynamic functions as infinitesimal generators of quasistatic processes, with a natural Poisson bracket formulation. This formulation of thermodynamic transformations is invariant under canonical coordinate transformations, just as classical mechanics is. The time-structure invariance of the Poisson bracket as manifested through the Jacobi identity has been used to derive constraint relationships on closure approximations [67]. Next we turn to the modern GENERIC framework which offers a particular useful generalized Poisson structure (GPS). The Poisson structure, together with a Jacobi identity had been recognized recently in two-fluid electrodynamics, in the generalized Heisenberg picture quantum mechanics, fluid models of plasma physics, and other branches of physics, cf. [40]. There is a variety of directions, which have not yet been worked out in detail, but extensively discussed. Upon these are nonholonomic constraints [341], boundary conditions [342,343], and extensions to so-called super-Poisson structures [344], Nambu–Jacobi brackets [345,346]. For these structures a number of different representations is known such that knowledge can be directly passed over to GENERIC concerning the development of efficient algorithms solving the GENERIC equations.

8.3. GENERIC equations

The GENERIC equations [40,347] preserve their structure across different levels (micro–macro) of description for beyond-equilibrium systems. For a given set of system variables $\boldsymbol{x}$ (defining the actual state space) the following (reversible and dissipative) brackets

$$\{A,B\} \equiv \frac{\delta A}{\delta \boldsymbol{x}} \cdot \boldsymbol{L} \cdot \frac{\delta B}{\delta \boldsymbol{x}}, \quad [A,B] \equiv \frac{\delta A}{\delta \boldsymbol{x}} \cdot \boldsymbol{M} \cdot \frac{\delta B}{\delta \boldsymbol{x}} \tag{82}$$

for arbitrary functionals A, B on state space, the time evolution equation for arbitrary A

$$\frac{\mathrm{d}A}{\mathrm{d}t} = \{A,H\} + [A,S] \ , \tag{83}$$

the degeneracy conditions

$$\boldsymbol{M} \cdot \frac{\delta H}{\delta \boldsymbol{x}} = 0, \quad \boldsymbol{L} \cdot \frac{\delta S}{\delta \boldsymbol{x}} = 0 \ , \tag{84}$$

the antisymmetry of $\boldsymbol{L}$, the Casimir symmetry of $\boldsymbol{M}$, together with the positive definiteness of $\boldsymbol{M}$ and the following Jacobi identity (for arbitrary functionals A, B, C)

$$0 = \{\{A,B\},C\} + \{\{B,C\},A\} + \{\{C,A\},B\} \tag{85}$$

constitute the GENERIC framework [40]. The Hamiltonian H and entropy S essentially model the system under consideration, whereas $\boldsymbol{L}$ can be motivated by analyzing the transformation behavior of variables, and $\boldsymbol{M}$ models the dissipative motion of variables. The requirement for energy conservation and increasing entropy, respectively, implies the antisymmetry of $\boldsymbol{L}$ and a degeneracy condition and positive semidefinite block $\boldsymbol{M}$. The Jacobi identity must hold in order to ensure a self-consistent time-invariant description. A large number of thermodynamically admissible (generalized and extended) physical models has been collected at www.polyphys.mat.ethz.ch.

For a GENERIC bracket one can deduce the following evolution equation $\mathrm{d}\{A,B\}/\mathrm{d}t = \{\mathrm{d}A/\mathrm{d}t, B\} + \{A, \mathrm{d}B/\mathrm{d}t\} = \{\{A,B\},H\}$. This expression reflects the time structure invariance of a Poisson bracket, i.e., the operator $\boldsymbol{L}$ behaves as a 'conserved' quantity. If the subscript t denotes the time-dependent solution F_t of the evolution equation $\mathrm{d}F_t/\mathrm{d}t = \{F_t, H\}$, then the Jacobi identity implies time structure invariance in the sense that $\{A,B\}_t = \{A_t, B_t\}$ for arbitrary functions A, B on state space. Definition (82) implies that when evaluating the Jacobi identity (85) second derivatives of the functions A, B, C would appear in principle. However, these second derivatives cancel pairwise, simplifying the Jacobi identity. The bracket of classical point mechanics fulfills the Jacobi identity since all elements of the matrix $\boldsymbol{L}$ are constant. It is sufficient to test the Jacobi identity against three *linear* functions [348] (this reference also provides a code for evaluating Jacobi identities). Worked out examples are given in [40,348].

Dynamic GENERIC equations for a single-segment reptation model without independent alignment, incorporating ideas of convective constraint release and anisotropic tube cross section in flow [349] have been developed by Öttinger [350], and investigated in [265], see also Section 6.1.

8.4. Dissipative particles

Because large-scale NEMD simulation can bridge time scales dictated by fast modes of motion together with slow modes, which determine viscosity, it can capture the effects of varying molecular topology on fluid rheology resulting, e.g., from chemical reactions. Mesoscopic regimes involving scales exceeding several nsec and/or micrometers require the 'fast' molecular modes of motion to be eliminated in favor of a more coarse grained representation, where the internal degrees of freedom of the fluid are ignored and only their center of mass motion is resolved. On this level, the particles will represent clusters of atoms or molecules, so-called, dissipative particles (DPD). It is possible to link and pass the averaged properties of molecular ensembles onto dissipative particles by using bottom up approach from NEMD/NEBD by means of the somewhat systematic coarse-graining procedure [351]. GENERIC had been used to construct modifications of Smoothed Particle Hydrodynamics (SPH) including thermal fluctuations and DPD in [352]. A method suited for the efficient treatment of polymer solution dynamics is the Lattice Boltzmann (LB) method and its improved versions [353]. A GENERIC formulation of LB has been discussed in [354]. In its application to polymer solution dynamics, the polymer itself is still treated on a simple molecular level using a bead–spring lattice model, but the solvent molecules are treated on the level of a discretized Boltzmann equation. In this way the hydrodynamics of the solvent is

correctly captured, and the hydrodynamic interaction between different units on the polymer chain, which is mediated by the hydrodynamic flow generated within the solvent through the motion of the polymer, is present in the simulation without explicit treatment of all solvent molecules. It is expected, that NEMD, DPD and LB together can capture both microscopic and macroscopic scales [355].

8.5. Langevin and Fokker–Planck equation, Brownian dynamics

In order to apply the GENERIC framework it is important to identity the relevant (state) variables which may sufficiently describe the given physical system. In Section 6 we dealt with primitive path models which certainly are more abstract and less dimensional objects than FENE chains discussed in the foregoing sections. With the treatment of elongated particles (Section 7) we continued the way through models possessing a decreasing number of molecular details. We therefore provide some general comments on how to reduce the number of variables in those dynamical model systems, which are described in terms of stochastic differential equations, such as Langevin equations for a set of stochastic variables $\boldsymbol{x}$, whose typical structure is to split the equation of motion for a variable into a deterministic (drift) plus a stochastic (diffusion) part

$$\frac{\mathrm{d}}{\mathrm{d}t}\boldsymbol{x} = \boldsymbol{A}(\boldsymbol{x}) + \boldsymbol{B}\cdot\boldsymbol{\eta} \tag{86}$$

with time t and 'noise' $\boldsymbol{\eta}$ or equivalent FP equations (used at several places throughout this review) for the corresponding distribution function $\psi(\boldsymbol{x},t)$

$$\frac{\partial\psi}{\partial t} = \mathscr{L}_{\mathrm{FP}}\psi, \quad \mathscr{L}_{\mathrm{FP}} = -\frac{\partial}{\partial\boldsymbol{x}}\cdot\boldsymbol{A}(\boldsymbol{x},t) + \frac{\partial}{\partial\boldsymbol{x}}\frac{\partial}{\partial\boldsymbol{x}} : \boldsymbol{D}(\boldsymbol{x},t) \tag{87}$$

with diffusion tensor $\boldsymbol{D} = \boldsymbol{B}^{\dagger}\cdot\boldsymbol{B}$ using Ito's interpretation. The difficulty of solving the FP equation like any other partial differential equation increases with increasing number of independent variables. It is therefore advisable to eliminate as many variables as possible. For an introduction to stochastic modeling, including an introduction to nonequilibrium Brownian dynamics (NEBD) computer simulation which rigorously solves (86), see [356,357,368].

8.6. Projection operator methods

If the drift and diffusion coefficients do not depend on some variables, the Fourier transform of the probability density for these variables can then be obtained by an equation where the variables no longer appear. To be more specific, if the drift and diffusion coefficients do not depend on $x_1,\ldots,x_n$ with $N > n$ being the total number of variables, making a Fourier transform of p with respect to the first n variables, by using the FP equation (87) and performing partial integrations the following equation for $\hat{\psi} = \hat{\psi}(x_{n+1},\ldots,x_N)$ must be solved: $\partial\hat{\psi}/\partial t = \hat{\mathscr{L}}_{\mathrm{FP}}\hat{\psi} = \hat{\mathscr{L}}_{\mathrm{FP}}(x_{n+1},\ldots,x_N)$ with

$$\hat{\mathscr{L}}_{\mathrm{FP}} = -i\sum_{i=1}^{n} k_i A_i - \sum_{i=n+1}^{N}\frac{\partial A_i}{\partial x_i} - \sum_{i,j=1}^{n} k_i k_j D_{ij} + 2i\sum_{i=1}^{n}\sum_{j=n+1}^{N} k_i\frac{\partial D_{ij}}{\partial x_j} + \sum_{i,j=n+1}^{N}\frac{\partial^2 D_{ij}}{\partial x_i\partial x_j}\ . \tag{88}$$

Generally, (88) must be resolved for every $\boldsymbol{k}$. If one is looking only for periodic solutions in the variables x_i ($i \leqslant n$), the wave numbers k_i must be integers and the integral (for the Fourier transform)

must be replaced by a sum over these integer numbers. Furthermore, if one is interested only in some expectation values of the form $\langle \exp \mathrm{i}mx_i(t)\rangle$ (for a specific $i \leqslant n$), only the solution of (88) with $k_i = -m$ needs to be calculated. A class of FP equations with two variables where the drift and diffusion coefficients do not depend on one variable and where solutions are given in terms of hypergeometric functions, see [358] and Appendix A6 of [357]. If the decay constants for some variables are much larger than those for other ones, the 'fast' variables can then approximately be eliminated. This is achieved by adiabatic elimination of the fast variables. Starting from the Langevin equation (86) for the slow ($\equiv x_1$) and fast ($\equiv x_2$) variables, the FP equation for the distribution function $\psi(\boldsymbol{x})$ is rewritten as $\partial\psi/\partial t = [\mathscr{L}_1 + \mathscr{L}_2]\psi$, with $-i = 1$ (slow) and $i = 2$ (fast)—

$$\mathscr{L}_i = \frac{\partial \tilde{A}_i(\boldsymbol{x})}{\partial x_i} + \frac{\partial^2}{\partial x_i^2} D_{ii}(\boldsymbol{x}), \quad \tilde{A}_i(\boldsymbol{x}) = A_i(\boldsymbol{x}) + B_{ii}\frac{\partial}{\partial x_i} B_{ii} \ . \tag{89}$$

In the spirit of the Born–Oppenheimer approximation in quantum mechanics one first looks for eigenfunctions of the operator $\mathscr{L}_2$. Here the variable x_1 appears as a parameter. We assume that for every parameter a stationary solution and discrete eigenvalues λ_n and eigenfunctions ϕ_n exist ($n \geqslant 0$). These generally depend on the parameter x_1: $\mathscr{L}_2(\boldsymbol{x})\phi_n(\boldsymbol{x}) = \lambda_n(x_1)\phi_n(\boldsymbol{x})$. For $n = 0$, $\lambda_0 = 0$ we have the stationary solution $\psi_{\mathrm{stat}} = \phi_0(\boldsymbol{x})$. By expanding the distribution function ψ into the complete set ϕ_n of the operator $\mathscr{L}_2\psi(\boldsymbol{x}) = \sum_m c_m(x_1,t)\phi_m(\boldsymbol{x})$, and inserting this expansion into the FP equation involving $\mathscr{L}_{1,2}$ one obtains $[\partial/\partial t + \lambda_n(x_1)]c_n = \sum_{m=0}^{\infty} L_{n,m}c_m$, with $L_{n,m} \equiv \int \phi_n^+ \mathscr{L}_1(\boldsymbol{x})\phi_m(\boldsymbol{x})\,\mathrm{d}x_2$, and the functions ϕ^+ denote the eigenfunctions of the adjoint operator $\mathscr{L}_1^\dagger$. The orthonormalization and completeness relations read $\int \phi_n^\dagger \phi_m\,\mathrm{d}x_2 = \delta_{nm}$ and $\int \phi_n^\dagger(x_1,x_2)\phi_n(x_1,x_2') = \delta(x_2 - x_2')$, respectively. The $L_{n,m}$ are operators with respect to the slow variable x_1. Because we are interested only in the time scale large compared to the decay coefficient of the fast variable, we may neglect the time derivative in the equation with $n \geqslant 1$. Finally, the equation of motion for the distribution function $\psi(x_1,t) = c_0(x_1,t)$ of the relevant variable x_1 reads

$$\frac{\partial\psi(x_1,t)}{\partial t} = \mathscr{L}_0\psi(x_1,t), \quad \mathscr{L}_0 = L_{0,0} + \sum_{n=1}^{\infty} L_{0,n}\lambda_n(x_1)^{-1}L_{n,0} + \cdots \ , \tag{90}$$

where the dots denote higher order terms and, in particular,

$$L_{0,0} = -\frac{\partial x}{\partial x_1}\int \tilde{A}_1(\boldsymbol{x})\phi_0(\boldsymbol{x})\,\mathrm{d}x_2 + \frac{\partial^2}{\partial x_1^2}\int D_{ii}(\boldsymbol{x})\phi_0(\boldsymbol{x})\,\mathrm{d}x_2 \ . \tag{91}$$

To solve (90) explicitly for the distribution function $\psi(x_1,t)$ for the slow variables, the operator $\mathscr{L}_0$ should be given analytically. This is the case only if the eigenvalues and eigenfunctions of $\mathscr{L}_2$ are known analytically and if the matrix elements occurring in (90) can be calculated analytically. An application of this procedure is given in p. 192 of Ref. [357]. Quite often the elimination of one or more variables is done with the Nakajima–Zwanzig projector operator formalism [359–362]. This formalism can be alternatively applied, whereby a projection operator $\mathscr{P}$ is defined by $\mathscr{P}\psi = (\int \phi_0^\dagger\psi\,\mathrm{d}x_2)\phi_0$, where ϕ_0 is the (above) stationary solution. In view of the orthogonality relations given above, $\mathscr{P}^2 = \mathscr{P}$ for a projection operator holds. Because the system $\phi_n, \phi_n^\dagger$ is

complete, the operator $1-\mathscr{P}$ may be cast in the form $\mathscr{Q}\psi \equiv (1-\mathscr{P})\psi = \sum_{n=1}^{\infty}(\int \phi_n^{\dagger}\psi \,\mathrm{d}x_2)\phi_n$. In the projection operator formalism, the equation of motion is split up into two coupled equations for $\mathscr{P}\psi$ and $(1-\mathscr{P})\psi$, i.e., into

$$\frac{\partial}{\partial t}\psi = \mathscr{L}_{\mathrm{FP}}\psi = \mathscr{P}\mathscr{L}_{\mathrm{FP}}\psi + \mathscr{Q}\mathscr{L}_{\mathrm{FP}}\psi \ , \tag{92}$$

with $\mathscr{P}\mathscr{L}_{\mathrm{FP}}\psi = \mathscr{P}\mathscr{L}\mathscr{P}\psi + \mathscr{P}\mathscr{L}\mathscr{Q}\psi$, and $\mathscr{Q}\mathscr{L}_{\mathrm{FP}}\psi = \mathscr{Q}\mathscr{L}\mathscr{P}\psi + \mathscr{Q}\mathscr{L}\mathscr{Q}\psi$. The usual Markov approximation to the formal solution of this problem consists in neglecting the time derivative, as used here in order to derive (90).

An appropriate way of systematic coarse-graining is provided by GENERIC [40] and its statistical foundation based on projection operator techniques for separating time scales [363]. For Monte Carlo simulations, nonequilibrium ensembles corresponding to the deformations of polymer molecules in flows can be introduced and used in order to determine deformation-dependent energies and entropies [364], which are the generators of reversible and irreversible time-evolution, Eq. (82), respectively. For MD simulations, the projection-operator formalism shows that all dynamic material information can and actually should be evaluated in a systematic way from simulations over time spans much shorter than the final relaxation time [365].

8.7. Stress tensors: Giesekus–Kramers–GENERIC

Within so called GENERIC Canonical Monte Carlo (GCMC) [364] and the 'reduced description' mentioned in Section 2.6 the relevant distribution function is approximated using a reduced set of (slow) variables. These may be particular moments of the distribution function itself. Using the underlying FP equation from this representation one can derive equations of change for the slow variables, and sometimes solve the set of equations for the 'conjugate' or 'dual' variables efficiently. Within GCMC the distribution function (based on all 'atomistic' phase space coordinates abbreviated as $\boldsymbol{z}$) involves unknown Lagrange parameters $\boldsymbol{\Lambda}$ and a 'phase space function' $\boldsymbol{\Pi}(\boldsymbol{z})$:

$$\psi(\boldsymbol{z})_{\boldsymbol{\Lambda}} = \psi_{\mathrm{eq}}\frac{1}{Z}\exp^{-\boldsymbol{\Lambda}:\boldsymbol{\Pi}}, \quad \psi_{\mathrm{eq}} \propto \exp^{-\beta E_0} \tag{93}$$

normalized by Z. Here, For the case of the homogeneous Hookean bead–spring model (Rouse model) with bond energy $E_0 \equiv (H/2)\sum_k \boldsymbol{Q}_k \cdot \boldsymbol{Q}_k$ we wish to see under which conditions the three different representations for the stress tensor (Gieskus, Kramers, GENERIC) are equal to each other, and we want to provide an expression of the Lagrange parameter in terms of flow parameters. See [366] for a discussion about material objectivity and thermodynamical consistency of stress tensor expressions.

Let us consider a single (arbitrary) normal mode $\boldsymbol{\Pi} \equiv \boldsymbol{X}_P\boldsymbol{X}_P$ $(P \in 1,\ldots,N-1)$ as slow variable. The first mode, for example, is given by $\boldsymbol{X}_1 \equiv \sum_i (2/N)^{1/2}\sin(\mathrm{i}\pi/N)\boldsymbol{Q}_i$ [68]. The Gieskus expression for the stress tensor is known as

$$\boldsymbol{\sigma}^{\mathrm{GIE}} = -\frac{1}{2}n\zeta\sum_{i,j=1}^{N-1} C_{i,j}(\boldsymbol{\kappa}\cdot\langle\boldsymbol{Q}_i\boldsymbol{Q}_j\rangle + \langle\boldsymbol{Q}_i\boldsymbol{Q}_j\rangle\cdot\boldsymbol{\kappa}^{\mathrm{T}}) \tag{94}$$

with the useful properties $\sum_{ij} C_{ij}\boldsymbol{Q}_i\boldsymbol{Q}_j = \sum_k c_k \boldsymbol{X}_k\boldsymbol{X}_k$, $c_k = 1/a_k$ and $a_k = 4\sin^2(k\pi/(2N))$ and $\sum_{k=1}^{N-1} c_k = (N^2-1)/6$ [6]. The Kramers expression reads [6]

$$\boldsymbol{\sigma}^{\mathrm{KRA}} = n\sum_i^{N-1} \langle \boldsymbol{Q}_i \boldsymbol{F}_i \rangle + (N-1)nk_BT\,\mathbf{1} \tag{95}$$

with $\boldsymbol{F}_i = -\mathrm{d}E_0/\mathrm{d}\boldsymbol{Q}_i$, and the GENERIC expression for the same problem (assuming a symmetric stress tensor) reads [40]

$$\boldsymbol{\sigma}^{\mathrm{GEN}} = nk_BT(\boldsymbol{\Lambda}\cdot\boldsymbol{X} + \boldsymbol{X}^{\mathrm{T}}\cdot\boldsymbol{\Lambda}^{\mathrm{T}})),\ \boldsymbol{X} = \langle \boldsymbol{\Pi}\rangle \tag{96}$$

In the above equations the average is defined via $\langle F\rangle = \int\int F\,\psi_{\boldsymbol{\Lambda}}\,\mathrm{d}\boldsymbol{z}$ where $\boldsymbol{z} = \{\boldsymbol{Q}_1, \boldsymbol{Q}_2, \ldots, \boldsymbol{Q}_{N-1}\}$. Inserting the special form $\boldsymbol{\Pi}$ into (93) we obtain $\psi(\boldsymbol{z})_{\boldsymbol{\Lambda}} = Z^{-1}\exp\{-\boldsymbol{\Lambda} : \boldsymbol{X}_1\boldsymbol{X}_1 - (\beta H/2)\sum_k \boldsymbol{X}_k\cdot\boldsymbol{X}_k\}$ and $\boldsymbol{X} = \langle\boldsymbol{\Pi}\rangle = \frac{1}{2}(\boldsymbol{\Lambda} + (\beta H/2)\mathbf{1})^{-1}$, or equivalently, an expression of the Lagrange parameter in terms of the averaged normal mode $\boldsymbol{\Lambda} = \frac{1}{2}(\boldsymbol{X}^{-1} - \beta H\mathbf{1})$. The GENERIC stress is thus rewritten as

$$\boldsymbol{\sigma}^{\mathrm{GEN}} = nk_BT(\mathbf{1} - \beta H\boldsymbol{X})\ . \tag{97}$$

By using the identity

$$\langle \boldsymbol{X}_k\boldsymbol{X}_k\rangle = \frac{1}{\beta H}\mathbf{1} + \delta_{k,P}\left(\boldsymbol{X} - \frac{1}{\beta H}\mathbf{1}\right) \tag{98}$$

we immediately see, that $\boldsymbol{\sigma}^{\mathrm{KRA}} = \boldsymbol{\sigma}^{\mathrm{GEN}}$ rigorously holds. Concerning the correspondence between Gieskus and GENERIC stresses we arrive at the following condition for $\boldsymbol{X}$ in terms of the flow field: $\boldsymbol{\sigma}^{\mathrm{GEN}} = \boldsymbol{\sigma}^{\mathrm{GIE}}$ if and only if

$$-4\lambda_H\dot{\gamma}\left(\frac{N^2-1}{6} - c_P\right) - 2c_P\lambda_H(\beta H)(\boldsymbol{\kappa}\cdot\boldsymbol{X} + \boldsymbol{X}\cdot\boldsymbol{\kappa}^{\mathrm{T}}) = \mathbf{1} - \beta H\,\boldsymbol{X} \tag{99}$$

with the time constant of Hookean dumbbell $\lambda_H = \zeta/(4H)$. In order to apply these findings, let us consider simple shear flow with dimensionless shear rate $\Gamma = \dot{\gamma}\lambda_H$. For that particular case we obtain the following moment $\boldsymbol{X}$ and Lagrange parameter $\boldsymbol{\Lambda}$ in terms of the shear rate:

$$\boldsymbol{X} = \frac{1}{\beta H}\begin{pmatrix} 1 + 4c_P\dfrac{(N^2-1)}{3}\Gamma^2 & \dfrac{N^2-1}{3}\Gamma & 0 \\ & 1 & 0 \\ & & 1 \end{pmatrix}, \tag{100}$$

$$\boldsymbol{\Lambda} = \beta H\begin{pmatrix} \dfrac{(N^2-1)(N^2-1-12c_P)}{2(9-\Gamma^2(N^2-1)(N^2-1-12c_P))}\Gamma^2 & -\dfrac{3(N^2-1)}{2(9-\Gamma^2(N^2-1)(N^2-1-12c_P))}\Gamma & 0 \\ & \dfrac{(N^2-1)}{2(9-\Gamma^2(N^2-1)(N^2-1-12c_P))}\Gamma^2 & 0 \\ & & 0 \end{pmatrix}. \tag{101}$$

Note that $N^2-1-12c_P<0$ for $P=1$, $N^2-1-12c_P>0$ for $P=2,3$, both signs (dependent on N) otherwise. The first mode should always be taken into account within the set of slow variables. $\boldsymbol{\Lambda}$ is nontrivial and singular. When considering a single mode P we therefore recover the expected form of the stress tensor and the exact Rouse viscosity by matching the stresses, but we have disagreement for the first normal stress. To be more specific,

$$\eta = nk_BT\lambda_H\frac{(N^2-1)}{3} = \eta^{\text{Rouse}},$$

$$\Psi_1 = nk_BT\lambda_H^2\frac{4(N^2-1)}{3}c_P \neq \Psi_1^{\text{Rouse}} \ . \tag{102}$$

This example can be generalized to other types of flow and other (more suitable) choices for the phase space function $\boldsymbol{\Pi}$ in terms of 'atomistic coordinates'. Several examples are discussed in [364]. The goal is to approximate the correct distribution function in a most efficient way by considering a small number of relevant variables. These must not necessarily be the normal coordinates we had just chosen for illustrative purpose.

8.8. Coarse-graining: from atomistic chains to the primitive path

A procedure for coarse-graining polymer molecules from the atomistic level of description (and also FENE chain level) to the reptation level for entangled polymers had been presented in Ref. [142]. While this method is based on collapsing a certain number of atoms or monomers into a large unit at their center of mass, the smooth and uniform dependence of the coarse-grained chain on positions of all atoms proposed in [367] is useful if one is interested in a two-way coupling of two levels of description as pointed out in [368]. We just summarize how to explicitly apply coarse-graining from the latter procedure, which is illustrated in Fig. 60.

The transformation, parametrized by a single parameter, $\mathscr{P}_\xi : \{\boldsymbol{x}_i^0\} \to \{\boldsymbol{x}_i\}$ maps a set of $i=1,\ldots,N$ atomistic (or FENE chain) coordinates of a linear chain to a new set with an equal number of coordinates, called coarse-grained coordinates $\boldsymbol{x}_i$, which define the coarse-grained chain or 'primitive path' $\{\boldsymbol{x}_i\}$ of the atomistic chain. In order to motivate the mapping, we require, that $\mathscr{P}_0 = \mathrm{Id}$, i.e., for $\xi=0$ all information of the atomistic chains is conserved for the coarse-grained chain. The opposite limit reflects a complete loss of information about the atomistic structure, i.e., the projection in the limit $\xi\to\infty$ gives give a straight line (or dot) for arbitrary atomistic configurations. The recommended mapping results from minimization of the energy

$$E \propto \frac{1}{2}\sum_{i=1}^{N}(\boldsymbol{x}_i-\boldsymbol{x}_i^0)^2 + \frac{\xi}{2}\sum_{i=1}^{N-1}(\boldsymbol{x}_{i+1}-\boldsymbol{x}_i)^2, \tag{103}$$

for a system of two types of Hookean springs. The first type connects adjacent beads within the primitive chain, the second type connects the beads of the primitive chain with the atomistic beads, and ξ is the ratio between spring coefficients. The mapping from atomistic $\boldsymbol{x}_o$ to coarse-grained coordinates

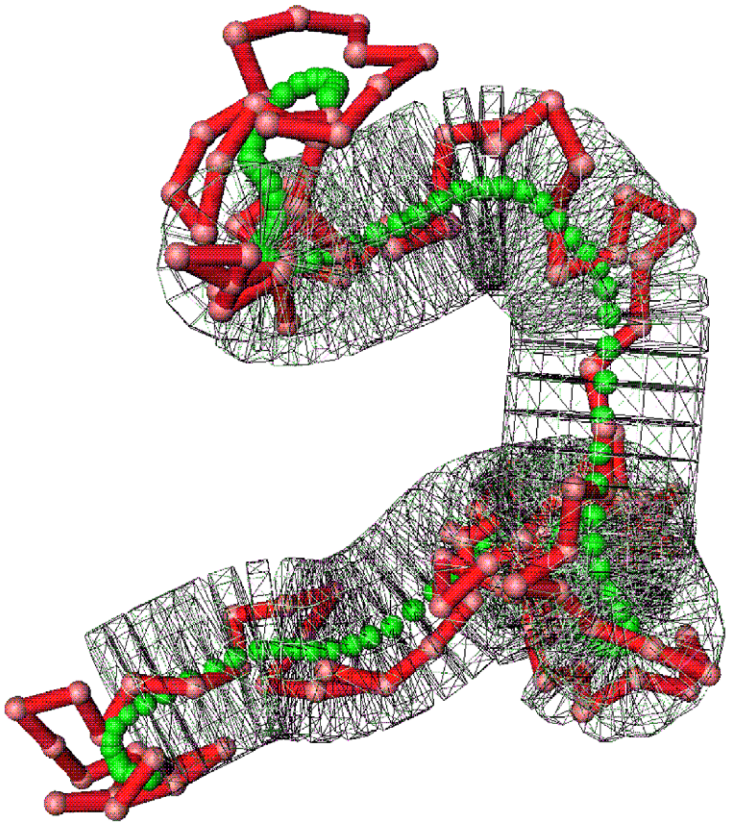

Fig. 60. Microscopic chain (dark beads) and its primitive path (light beads, tangential cylinder indicated). The latter is obtained by the mapping $\mathscr{P}_\xi$ via Eq. (104) for a certain ratio of spring coefficients ξ.

$\boldsymbol{x}$ reads, with the $N \times N$ tri-diagonal matrix $\mathscr{P}^{-1}$ which can be inverted with order N effort:

$$\boldsymbol{x}_i = \sum_{j=1}^{N} \mathscr{P}_{ij} \cdot \boldsymbol{x}_j^0, \quad \mathscr{P}^{-1} = \begin{pmatrix} 1+\xi & -\xi & 0 & \cdots & \cdots & 0 \\ -\xi & 1+2\xi & -\xi & 0 & \ddots & \vdots \\ 0 & -\xi & 1+2\xi & \ddots & \ddots & \vdots \\ \vdots & \ddots & \ddots & \ddots & -\xi & 0 \\ \vdots & \ddots & 0 & -\xi & 1+2\xi & -\xi \\ 0 & \cdots & \cdots & 0 & -\xi & 1+\xi \end{pmatrix}, \tag{104}$$

for all $i = 1 \ldots N$. The discrete coarse-graining had been recently analyzed in [368] for wormlike 'atomistic' chains characterized by their squared end-to-end vector $\langle \boldsymbol{R}_{(0)}^2 \rangle$ and their tube diameter d_T (i.e., quantities usually tabulated, cf. Section 4.5 and Table 3). One of the important result of [368]

states, that the correct parameter ξ is determined by these two characteristics via

$$\frac{1}{\xi^{1/2}} \propto \frac{\langle \boldsymbol{R}_{(0)}^2 \rangle}{N-1} \frac{1}{d_T^2}, \quad \text{for } \xi^{1/2} \ll N, \tag{105}$$

with a prefactor of order unity. In terms of the quantities introduced in Section 4.5 this relationship is rewritten as $\xi \propto N_e^2$, for $N \gg N_e$ with the characteristic entanglement length N_e.

9. Concluding remarks

The development of constitutive relationships which connect strain or strain rate with stress and material behavior is at the heart of a successful macroscopic modeling of complex fluids. We reviewed simple physical models which allow to find such relationships for the case of neutral bulk polymeric fluids, nematic fluids, ferrofluids, colloidal suspensions. We have shown that the simplest approximate treatments (Section 2) such as the Peterlin approximation turn out to be insufficiently precise. More detailed chain models which allow to capture molecular architecture, finite extensibility, bending stiffness and interchain interactions without approximation, on the other hand, are computationally expensive while remaining conceptually simple (Sections 3–5). In order to predict rheooptic behaviors on time and length scales relevant for applications chemical details are shown to be not essential. These models serve to make progress towards appropriate decoupling approximations for stochastic differential equations, and a reduced description using relevant (slow) variables (Sections 6–8). Most interestingly, they provide deep insight into the microscopic origins of viscoelastic behavior.

This paper should be viewed as an introduction to the microscopic modeling of anisotropic, in particular, polymeric fluids involving FENE chain models, tube models, and elongated particle models and can serve as a starting point to devise suitable models and to understand nonequilibrium complex fluids as encountered in applications and current experiments. We discussed several efficient strategies to solve microscopic models such as the Cholesky decomposition or variance reduction methods for FENE solutions with HI. We provided examples which demonstrated how to attack the nonanalytical solvable models in approximate, and less approximate fashion. Coarsening procedures have been applied to microscopic trajectories onto objects which can be retreated within the framework of primitive path models. Using the coarsening procedure of Section 8.8 one should be able to extract the parameters of tube models directly from atomistic simulation on the nanosecond scale, i.e., small compared to the reptation time scale. Insight from the microscopic FENE chain level—such as anisotropic tube renewal, stress-optic failures—have been used to refine these theories and to work out consequences in Section 6. The rheological crossover observed for FENE chain melts allowed to discuss and interpret characteristic lengths scales in polymer melts. These scales can be expressed in terms of density, molecular weight, and flexibility, i.e., based on geometric or ‘topological’ quantities and independent of chemical details. The soft ellipsoid model [369,5] is another representative of a coarsening strategy from many monomers to many polymers. Elongated (rigid) particle models have been characterized in detail and connection was made to macroscopic description such as the EL theory for nematics. Inhomogeneous extensions of FP discussed in this review have studied, e.g., for liquid crystals in order to calculate elastic coefficients [306].

The formulation of new models for nonequilibrium fluids remains a difficult task but should be guided through frameworks ensuring their thermodynamically admissible, intrinsically consistent, description. The corresponding GENERIC approach reviewed in Section 8.3 has not yet been extended to describe nonholonomic constraints or boundary conditions. It may be interesting to show, e.g., how the simple model for polymer melts considering anisotropic tube renewal (Section 6.2) may be cast into a suitable generalized framework.

This review did rarely provide sufficiently detailed information on how to implement simulations, but original articles for each application have been cited, where missing details can be found. Standard textbooks such as [157,68,143,197,209,6] contain background and supplementary information on the modeling of nonequilibrium fluids. An overview of some of the more popular computational models and methods used today in the field of molecular and mesoscale simulation of polymeric materials, ranging from molecular models and methods that treat electronic degrees of freedom to mesoscopic field theoretic methods can be also found in [370,5,14].

Acknowledgements

It is my pleasure to thank A. Ben-Shaul, W. Carl, P.J. Daivis, M. Doi, P. Espanol, D.J. Evans, J. Fang, P. Fischer, W. Gelbart, S. Hess, H. Hoffmann, W.G. Hoover, M. Hütter, P. Ilg, I.V. Karlin, K. Kremer, K. Kroy, R.G. Larson, W. Loose, C. Luap, R. Makhloufi, P. Marrucci, V. Mavrantzas, R. Muller, H.C. Öttinger, J. Ramirez, G. Rienäcker, E. Sackmann, C. Schneggenburger, H.S. Sellers, I. Stankovic, D.N. Theodorou, B.D. Todd, H. Voigt, K. Wilhelm for collaborations and very inspiring discussions on the physics and simulation of complex fluids. This research had had been performed under the auspices of the Deutsche Forschungsgemeinschaft (Sfb 448, SPP 1106) and was supported in part by the National Science Foundation under Grant No. PHY99-07949 via the program 'Dynamics of complex and macromolecular fluids' at the ITP, Santa Barbara, CA. Supercomputer facilities Cray/ZIB Berlin and Beowulf/ETH Zürich have been extensively used.

References

[1] N. Goldenfeld, L.P. Kadanoff, Science 284 (1999) 87.
[2] S.S. Saarman, Phys. Rep. 305 (1998) 1.
[3] R.R. Netz, D. Andelman, Phys. Rep. 380 (2003) 1.
[4] A.N. Gorban, I.V. Karlin, A.Y. Zinovyev, Constructive methods of invariant manifolds for kinetic problems, Phys. Rep. (2004), to appear.
[5] K. Kremer, F. Muller-Plathe, Mol. Simul. 28 (2002) 729.
[6] R.B. Bird, O. Hassager, R.C. Armstrong, C.F. Curtiss, Dynamics of Polymeric Liquids, Volumes 1+2, Wiley, New York, 1987.
[7] T.C.B. McLeish, Adv. Phys. 51 (2002) 1379.
[8] R.G. Larson, T.T. Perkins, D.E. Smith, S. Chu, Phys. Rev. E 56 (1997) 1794, and references cited herein.
[9] R.B. Bird, J.M. Wiest, Annu. Rev. Fluid Mech. 27 (1995) 169.
[10] P.S. Doyle, E.S.G. Shaqfeh, A.P. Gast, J. Fluid Mech. 334 (1997) 251.
[11] B.H.A.A. Van den Brule, J. Non-Newtonian Fluid Mech. 47 (1993) 357.
[12] B. Dünweg, D. Reith, M. Steinhauser, et al., J. Chem. Phys. 117 (2002) 914.
[13] K. Kremer, Macromol. Chem. Phys. 204 (2003) 257.

[14] K. Binder, G. Ciccotti (Eds.), Monte Carlo and Molecular Dynamics of Condensed Matter Systems, IPS Conference Proceedings, Bologna, 1996, pp. 669–723 and 825–841.
[15] J.W. Rudisill, P.T. Cummings, J. Non-Newtonian Fluid Mech. 41 (1992) 275.
[16] H.X. Guo, K. Kremer, T. Soddemann, Phys. Rev. E 66 (2002) 061503.
[17] M. Murat, G.S. Grest, K. Kremer, Europhys. Lett. 42 (1998) 401.
[18] G.S. Grest, Curr. Opin. Colloid Interface Sci. 2 (1997) 271.
[19] M. Kröger, W. Loose, S. Hess, J. Rheol. 37 (1993) 1057.
[20] P.J. Daivis, M.L. Matin, B.D. Todd, J. Non-Newtonian Fluid Mech. 111 (2003) 1.
[21] J. Koplik, J.R. Banavar, Phys. Rev. Lett. 84 (2000) 4401.
[22] G.S. Grest, Adv. Polym. Sci. 138 (1999) 149.
[23] P.G. Khalatur, A.R. Khokhlov, D.A. Mologin, J. Chem. Phys. 109 (1998) 9602, 9614.
[24] M.J. Stevens, M. Mondello, G.S. Grest, S.T. Cui, H.D. Cochran, P.T. Cummings, J. Chem. Phys. 106 (1997) 7303.
[25] Z.F. Xu, R. Khare, J.J. de Pablo, S. Kim, J. Chem. Phys. 106 (1997) 8285.
[26] P. Padilla, S. Toxvaerd, J. Chem. Phys. 104 (1996) 5956.
[27] J. Koplik, J.R. Banavar, Phys. Rev. Lett. 78 (1997) 2116.
[28] A. Uhlherr, D.N. Theodorou, Curr. Opin. Solid State Mech. 3 (1998) 544.
[29] W.M. Gelbart, A. Ben-Shaul, D. Roux, Micelles, Membranes, Microemulsions and Monolayers, Springer, New York, 1994.
[30] R.G. Larson, Curr. Opin. Colloid Interface Sci. 2 (1997) 361.
[31] M. Kröger, R. Makhloufi, Phys. Rev. E 53 (1996) 2531.
[32] W. Carl, R. Makhloufi, M. Kröger, J. Phys. France II (Paris) 7 (1997) 931.
[33] S.R. Zhao, C.P. Sun, W.X. Zhang, J. Chem. Phys. 106 (1997) 2520, 2530.
[34] M. Kröger, Comput. Phys. Commun. 118 (1999) 278.
[35] F. Affouard, M. Kröger, S. Hess, Phys. Rev. E 54 (1996) 5178.
[36] T. Odijk, Curr. Opin. Colloid Interface Sci. 1 (1996) 337.
[37] G. Lielens, P. Halin, I. Jaumain, R. Keunings, V. Legat, J. Non-Newtonian Fluid Mech. 76 (1998) 249.
[38] M. Dressler, B.J. Edwards, H.C. Öttinger, Rheol. Acta 38 (1999) 117.
[39] P. Wapperom, M.A. Hulsen, J. Rheol. 42 (1998) 999.
[40] H.C. Öttinger, M. Grmela, Phys. Rev. E 56 (1997) 6633.
[41] T. Soddemann, B. Dünweg, K. Kremer, Eur. Phys. J. E 6 (2001) 409.
[42] H.R. Warner, Ind. Eng. Chem. Fundam. 11 (1972) 379.
[43] A. Peterlin, Makromol. Chem. 44 (1961) 338.
[44] A. Peterlin, J. Polym. Sci., Polym. Lett. 48 (1966) 287.
[45] X. Fan, J. Non-Newtonian Fluid Mech. 17 (1985) 125.
[46] L.E. Wedgewood, D.N. Ostrov, R.B. Bird, J. Non-Newtonian Fluid Mech. 40 (1991) 119.
[47] P.S. Doyle, E.S.G. Shaqfeh, G.H. McKinley, S.H. Spiegelberg, J. Non-Newtonian Fluid Mech. 76 (1998) 79.
[48] M.D. Chilcott, J.M. Rallison, J. Non-Newtonian Fluid Mech. 29 (1988) 381.
[49] J. Remmelgas, P. Singh, L.G. Leal, J. Non-Newtonian Fluid Mech. 88 (1999) 31.
[50] G. Lielens, R. Keunings, V. Legat, J. Non-Newtonian Fluid Mech. 87 (1999) 179.
[51] C. Schneggenburger, M. Kröger, S. Hess, J. Non-Newtonian Fluid Mech. 62 (1996) 235.
[52] G.G. Fuller, Optical Rheometry of Complex Fluids, Oxford University Press, UK, 1995.
[53] B. Dünweg, K. Kremer, Phys. Rev. Lett. 61 (1991) 2996.
[54] B. Dünweg, K. Kremer, J. Chem. Phys. 99 (1993) 6983.
[55] S. Hess, C. Aust, L. Bennett, M. Kröger, C. Pereira Borgmeyer, T. Weider, Physica A 240 (1997) 126.
[56] C. Aust, M. Kröger, S. Hess, Macromolecules 32 (1999) 5660.
[57] J.K.C. Suen, Y.L.J. Joo, R.C. Armstrong, Annu. Rev. Fluid Mech. 34 (2002) 417.
[58] M. Melchior, H.C. Öttinger, J. Chem. Phys. 103 (1995) 9506.
[59] B.Z. Dlugogorski, M. Grmela, P.J. Carreau, J. Non-Newtonian Fluid Mech. 49 (1993) 23.
[60] G.B. Jeffrey, Proc. R. Soc. London, Ser. A 102 (1922) 161.
[61] E.J. Hinch, L.G. Leal, J. Fluid Mech. 71 (1975) 481.
[62] M.A. Peterson, Am. J. Phys. 47 (1979) 488.
[63] A.N. Kaufman, Phys. Lett. A 100 (1984) 419.

[64] A. Beris, B.J. Edwards, Thermodynamics of Flowing Systems with Internal Microstructure, Engineering and Science Series, Vol. 36, Oxford University Press, New York, 1994.
[65] R.J.J. Jongschaap, J. Non-Newtonian Fluid Mech. 96 (2001) 63.
[66] B.J. Edwards, H.C. Öttinger, R.J.J. Jongschaap, J. Non-Equilibrium Thermodyn. 22 (1997) 356.
[67] B.J. Edwards, H.C. Öttinger, Phys. Rev. E 56 (1997) 4097.
[68] H.C. Öttinger, Stochastic processes in polymeric fluids, in: Tools and Examples for Developing Simulation Algorithms, Springer, Berlin, 1996.
[69] H.C. Öttinger, J. Non-Newtonian Fluid Mech. 26 (1987) 207.
[70] L.E. Wedgewood, H.C. Öttinger, J. Non-Newtonian Fluid Mech. 27 (1988) 245.
[71] J. Bossart, H.C. Öttinger, Macromolecules 28 (1995) 5852;
J. Bossart, H.C. Öttinger, Macromolecules 30 (1997) 5527.
[72] C. Pierleoni, J.P. Ryckaert, Phys. Rev. Lett. 71 (1993) 1724.
[73] C. Pierleoni, J.-P. Ryckaert, Macromolecules 28 (1995) 5097.
[74] M. Herrchen, H.C. Öttinger, J. Non-Newtonian Fluid Mech. 68 (1997) 17.
[75] C.D. Dimitropoulos, R. Sureshkumar, A.N. Beris, J. Non-Newtonian Fluid Mech. 79 (1998) 433.
[76] Q. Zhou, R. Akhavan, J. Non-Newtonian Fluid Mech. 109 (2003) 115.
[77] R. Keunings, J. Non-Newtonian Fluid Mech. 68 (1997) 85.
[78] P. Ilg, I.V. Karlin, Phys. Rev. E 62 (2000) 1441.
[79] A. Link, J. Springer, Macromolecules 26 (1993) 464.
[80] N. Kuzuu, M. Doi, J. Phys. Soc. Jpn. 52 (1983) 3486.
[81] S. Hess, Z. Naturforsch. 31a (1976) 1034.
[82] W. Maier, A.Z. Saupe, Z. Naturforsch. 14a (1959) 882.
[83] W. Hess, J. Polym. Sci., Polym. Symp. 73 (1985) 201.
[84] S. Hess, J. Non-Newtonian Fluid Mech. 23 (1987) 305.
[85] S. Hess, W. Köhler, Formeln zur Tensorrechnung, Palm & Enke, Erlangen, 1980.
[86] P. Kaiser, W. Wiese, S. Hess, J. Non-Equilibrium Thermodyn. 17 (1992) 153.
[87] J. Remmelgas, L.G. Leal, J. Non-Newtonian Fluid Mech. 89 (2000) 231.
[88] E.C. Lee, M.J. Solomon, S.J. Muller, Macromolecules 30 (1997) 7313.
[89] J. Honerkamp, R. Seitz, J. Chem. Phys. 87 (1987) 3120.
[90] P. Van der Schoot, Macromolecules 25 (1992) 2923, and references cited herein.
[91] F. Boue, P. Lindner, Europhys. Lett. 25 (1994) 421.
[92] T. Kume, K. Asakawa, E. Moses, K. Matsuzaka, T. Hashimoto, Acta Polym. 46 (1995) 79.
[93] S.A. Patlazhan, P. Navard, J. Phys. France II (Paris) 5 (1995) 1017.
[94] M. Zisenis, J. Springer, Polymer 36 (1995) 3459.
[95] Y. Tsunashima, J. Chem. Phys. 102 (1995) 4673.
[96] R. Balian, From Microphysics to Macrophysics, Vol. 2, 2nd Edition, Springer, Berlin, 1992.
[97] P. Ilg, I.V. Karlin, M. Kröger, H.C. Öttinger, Physica A 319 (2003) 134.
[98] A.N. Gorban, I.V. Karlin, P. Ilg, H.C. Öttinger, J. Non-Newtonian Fluid Mech. 96 (2001) 203.
[99] P. Ilg, I.V. Karlin, H.C. Öttinger, Physica A 315 (2002) 367.
[100] P. Ilg, M. Kröger, S. Hess, J. Chem. Phys. 116 (2002) 9078.
[101] G. Strobl, The Physics of Polymers, Springer, Heidelberg, 1996.
[102] J.G. Kirkwood, J. Riseman, J. Chem. Phys. 16 (1948) 565.
[103] S.W. Fetsko, P.T. Cummings, Int. J. Thermophys. 15 (1994) 1085.
[104] M. Kröger, A. Alba, M. Laso, H.C. Öttinger, J. Chem. Phys. 113 (2000) 4767.
[105] H.C. Öttinger, J. Chem. Phys. 86 (1987) 3731;
H.C. Öttinger, J. Chem. Phys. 87 (1987) 1460.
[106] J. Rotne, S. Prager, J. Chem. Phys. 50 (1969) 4831.
[107] G.B. Thurston, A. Peterlin, J. Chem. Phys. 46 (1967) 4881.
[108] H.C. Öttinger, Y. Rabin, J. Non-Newtonian Fluid Mech. 33 (1989) 53.
[109] R.G. Larson, Constitutive Equations for Polymer Melts and Solutions, Butterworths, Boston, 1988.
[110] M. Fixman, Macromolecules 19 (1986) 1195, 1204.

[111] W. Press, S.A. Teukolsky, W.T. Vetterling, B.P. Flannery, Numerical Recipes in Fortran, 2nd Edition, Cambridge University Press, Cambridge, UK, 1992, p. 184.
[112] D. Dahlquist, A. Bork, Numerical Methods, Prentice-Hall, Englewood Cliffs, NJ, 1974.
[113] R.M. Jendrejack, M.D. Graham, J.J. de Pablo, J. Chem. Phys. 113 (2000) 2894.
[114] R. Rzehak, D. Kienle, T. Kawakatsu, W. Zimmermann, Europhys. Lett. 46 (1999) 821.
[115] R. Rzehak, W. Kromen, T. Kawakatsu, W. Zimmermann, Eur. Phys. J. E 2 (2000) 3.
[116] M. Melchior, H.C. Öttinger, J. Chem. Phys. 105 (1996) 3316.
[117] S. Navarro, M.C.L. Martinez, J. Garcia de la Torre, J. Chem. Phys. 103 (1995) 7631.
[118] P.S. Grassia, E.J. Hinch, L.C. Nitsche, J. Fluid Mech. 282 (1995) 373.
[119] J.D. Schieber, J. Non-Newtonian Fluid Mech. 45 (1992) 47.
[120] C. Elvingston, Biophys. Chem. 43 (1992) 9.
[121] W. Zylka, J. Chem. Phys. 94 (1991) 4628.
[122] C. Elvingston, J. Comput. Chem. 12 (1991) 71.
[123] M. Fixman, J. Chem. Phys. 89 (1988) 2442.
[124] M. Fixman, Faraday Discuss. 83 (1987) 199.
[125] D.-J. Yang, Y.-H. Lin, Polymer 44 (2003) 2807.
[126] A.J. Banchio, J.F. Brady, J. Chem. Phys. 118 (2003) 10323.
[127] J. Huang, T. Schlick, J. Chem. Phys. 117 (2002) 8573.
[128] J.R. Prakash, H.C. Öttinger, J. Non-Newtonian Fluid Mech. 71 (1997) 245.
[129] Y. Oono, M. Kohmoto, J. Chem. Phys. 78 (1983) 1.
[130] H.C. Öttinger, Phys. Rev. A 40 (1989) 2664.
[131] M. Schmidt, W. Burchard, Macromolecules 14 (1981) 210.
[132] A.Z. Akcasu, C.C. Han, Macromolecules 12 (1979) 276.
[133] Y. Miyaki, Y. Einaga, H. Fujita, M. Fakuda, Macromolecules 13 (1980) 588.
[134] M. Fixman, J. Chem. Phys. 78 (1983) 1594.
[135] J. Garcia de la Torre, M.C. Lopez, M.M. Terado, J. Freire, Macromolecules 17 (1984) 2715.
[136] A.M. Rubio, J.J. Freire, J.H.R. Clarke, C.W. Yong, M. Bishop, J. Chem. Phys. 102 (1995) 2277.
[137] J.M. Garcia Bernal, M.M. Lopez, M.M. Tirado, J. Freire, Macromolecules 24 (1991) 693.
[138] B.H. Zimm, G.M. Roe, L.F. Epstein, J. Chem. Phys. 24 (1956) 279.
[139] M. Daoud, G. Jannink, J. Phys. Lett. 39 (1976) 1045.
[140] P.G. de Gennes, Macromolecules 9 (1976) 587, 594.
[141] K. Kremer, G.S. Grest, I. Carmesin, Phys. Rev. Lett. 61 (1988) 566.
[142] K. Kremer, G.S. Grest, J. Chem. Phys. 92 (1990) 5057.
[143] K. Binder (Ed.), Monte Carlo and Molecular Dynamics Simulations in Polymer Science, Oxford University Press, USA, 1996.
[144] T. Aoyagi, M. Doi, Comput. Theor. Polym. Sci. 10 (2000) 317.
[145] J. Gao, J.H. Weiner, J. Chem. Phys. 90 (1989) 6749.
[146] M. Kröger, C. Luap, R. Muller, Macromolecules 30 (1997) 526.
[147] B.D. Todd, Comput. Phys. Commun. 142 (2001) 14.
[148] M. Pütz, K. Kremer, G.S. Grest, Europhys. Lett. 49 (2000) 735;
M. Pütz, K. Kremer, G.S. Grest, Europhys. Lett. 52 (2000) 721.
[149] Y. Masubuchi, J.I. Takimoto, K. Koyama, G. Ianniruberto, G. Marrucci, F. Greco, J. Chem. Phys. 115 (2001) 4387.
[150] T.P. Lodge, N.A. Rotstein, S. Prager, Adv. Chem. Phys. 79 (1990) 1.
[151] L.R.G. Treloar, Trans. Faraday. Soc. 36 (1940) 538.
[152] F. Bueche, J. Chem. Phys. 20 (1952) 1959.
[153] S.F. Edwards, Proc. Phys. Soc. 91 (1967) 513.
[154] P.G. de Gennes, J. Chem. Phys. 55 (1971) 572.
[155] A.L. Khodolenko, T.A. Vilgis, Phys. Rep. 298 (1998) 251.
[156] J.D. Weeks, D. Chandler, H.C. Andersen, J. Chem. Phys. 54 (1971) 5237.
[157] M.P. Allen, D.J. Tildesley, Computer Simulations of Liquids, Oxford Science, Oxford, UK, 1990.
[158] D.J. Evans, G.P. Morris, Statistical Mechanics of Nonequilibrium Liquids, Academic Press, London, 1990.

[159] W.G. Hoover, Physica A 240 (1997) 1.
[160] S. Hess, M. Kröger, Phys. Rev. E 61 (2000) 4629.
[161] G.S. Grest, B. Dünweg, K. Kremer, Comput. Phys. Commun. 55 (1989) 269.
[162] V.G. Mavrantzas, T.D. Boone, E. Zervopoulou, D.N. Theodorou, Macromolecules 32 (1999) 5072.
[163] M. Kröger, S. Hess, Phys. Rev. Lett. 85 (2000) 1128.
[164] R. Muller, J.J. Pesce, Polymer 35 (1994) 734.
[165] J.D. Ferry, Viscoelastic Properties of Polymers, 3rd Edition, Wiley, New York, 1980.
[166] M. Pütz, K. Kremer, G.S. Grest, Europhys. Lett. 49 (2000) 735.
[167] L.J. Fetters, D.J. Lohse, S.T. Milner, W.W. Graessley, Macromolecules 32 (1999) 6847.
[168] C. Luap, R. Muller, C. Picot, ILL exp. rep. 9-11-305;
[169] M. Kröger, H. Voigt, Macromol. Theory Simul. 3 (1994) 639.
[170] J. Gao, J.H. Weiner, Macromolecules 27 (1994) 1201, and references cited herein.
[171] M.N. Hounkonnou, C. Pierleoni, J.-P. Ryckaert, J. Chem. Phys. 97 (1992) 9335.
[172] J.T. Padding, W.J. Briels, J. Chem. Phys. 117 (2002) 925.
[173] D.J. Evans, W.G. Hoover, B.H. Failor, B. Moran, A.J.C. Ladd, Phys. Rev. A 28 (1983) 1016.
[174] H.J. Janeschitz-Kriegl, Polymer Melt Rheology and Flow Birefringence, Springer, Berlin, 1983.
[175] L.S. Priss, I.I. Vishnyakoov, I.P. Pavlova, Int. J. Polym. Mater. 8 (1980) 85.
[176] B.E. Read, Polym. Eng. Sci. 23 (1983) 835.
[177] J. Wilhelm, E. Frey, Phys. Rev. Lett. 77 (1996) 2581.
[178] T.B. Liverpool, R. Golestanian, K. Kremer, Phys. Rev. Lett. 80 (1998) 405.
[179] R. Everaers, F. Jülicher, A. Ajdari, A.C. Maggs, Phys. Rev. Lett. 82 (1999) 3717.
[180] Y. Kats, D.A. Kessler, Y. Rabin, Phys. Rev. E 65 (2002) 020801(R).
[181] S.F. Edwards, Proc. Phys. Soc. London 85 (1965) 613.
[182] N. Saito, K. Takahashi, Y. Yunoki, J. Phys. Soc. Jpn. 22 (1967) 219.
[183] K.F. Freed, Adv. Chem. Phys. 22 (1972) 1.
[184] J. des Cloizeaux, Phys. Rev. A 10 (1974) 1665.
[185] M. Muthukumar, B.G. Nickel, J. Chem. Phys. 80 (1984) 5839;
M. Muthukumar, B.G. Nickel, J. Chem. Phys. 86 (1987) 460.
[186] Y. Oono, Adv. Chem. Phys. 61 (1985) 301.
[187] O. Kratky, G. Porod, Recueil Trav. Chim. 68 (1949) 1106.
[188] N. Saito, K. Takahashi, Y. Yunoki, J. Phys. Soc. Jpn. 22 (1967) 219.
[189] R.P. Feynman, A.R. Hibbs, Quantum Mechanics and Path Integrals, McGraw-Hill, New York, 1975.
[190] J.B. Lagowski, J. Noolandj, J. Chem. Phys. 95 (1991) 1266.
[191] S.M. Bhattacharjee, M. Muthukumar, J. Chem. Phys. 86 (1987) 411.
[192] A.D. Egorov, P.I. Sobolevsky, L.A. Yanovich, Functional Integrals: Approximate Evaluation and Applications, in: Mathematics and Its Applications, Vol. 249, Kluwer, Dordrecht, 1993.
[193] D.J. Amit, Field Theory, The Renormalization Group and Critical Phenomena, McGraw-Hill, London, 1978.
[194] S. Panyukov, Y. Rabin, Europhys. Lett. 57 (2002) 512.
[195] P.G. de Gennes, Scaling Concepts in Polymer Physics, Cornell University Press, Ithaca, NY, 1979.
[196] W.M. Gelbart, A. Ben-Shaul, J. Phys. Chem. 100 (1996) 13169.
[197] R.G. Larson, The Structure and Rheology of Complex Fluids, Oxford University Press, Oxford, UK, 1999.
[198] J.P. Wittmer, A. Milchev, M.E. Cates, J. Chem. Phys. 109 (1998) 834.
[199] A.T. Bernardes, V.B. Henriques, P.M. Bisch, J. Chem. Phys. 101 (1994) 645.
[200] Y. Rouault, A. Milchev, Phys. Rev. E 51 (1995) 5905.
[201] K. Binder, Rep. Progr. Phys. 60 (1997) 487.
[202] P.J. Flory, Principles of Polymer Chemistry, Cornell University Press, Ithaca, NY, 1953.
[203] T.L. Hill, Statistical Mechanics, McGraw-Hill, New York, 1956.
[204] Y.A. Shchipunov, H. Hoffmann, Rheol. Acta 39 (2000) 542.
[205] P. Boltenhagen, Y.T. Hu, E.F. Matthys, D.J. Pine, Europhys. Lett. 38 (1997) 389.
[206] S.-Q. Wang, W.M. Gelbart, A. Ben-Shaul, J. Phys. Chem. 94 (1990) 2219.
[207] J.N. Israelachvili, D.J. Mitchell, B.W. Ninham, J. Chem. Soc. Faraday Trans. II 72 (1976) 1525.
[208] H. C. Booij, J. Chem. Phys. 80 (1984) 4571.

[209] M. Doi, S.F. Edwards, The Theory of Polymer Dynamics, Clarendon, Oxford, 1986.
[210] W. Carl, J. Chem. Soc. Faraday Trans. 91 (1995) 2525.
[211] W. Carl, W. Bruns, Macromol. Theory Simul. 3 (1994) 295.
[212] M.E. Cates, J. Phys. France (Paris) 49 (1988) 1593.
[213] R. Makhloufi, J.P. Decruppe, A. Aitali, R. Cressely, Europhys. Lett. 32 (1995) 253.
[214] M.E. Cates, Phys. Scripta 49 (1993) 107.
[215] P. Van Der Schoot, M.E. Cates, Europhys. Lett. 25 (1994) 515.
[216] Y. Bohbot, A. Ben-Shaul, R. Granek, W.M. Gelbart, J. Chem. Phys. 103 (1995) 8764.
[217] E. Sackmann, Macromol. Chem. Phys. 195 (1994) 7–28.
[218] J. Käs, H. Strey, E. Sackmann, Nature 368 (1994) 226.
[219] J. Käs, H. Strey, J.X. Tang, D. Finger, R. Ezzell, E. Sackmann, P.A. Janmey, Biophys. J. 70 (1996) 609–625.
[220] P.A. Janmey, S. Hvidt, J. Käs, D. Lerche, A. Maggs, E. Sackmann, M. Schliwa, T.P. Stossel, J. Biol. Chem. 269 (1994) 32503.
[221] H.J.C. Berendsen, Science 271 (1996) 954.
[222] I. Carmesin, K. Kremer, Macromolecules 21 (1988) 2819.
[223] H.P. Deutsch, K. Binder, Chem. Phys. 94 (1991) 2294.
[224] G.S. Grest, K. Kremer, E.R. Duering, Physica A 194 (1993) 330.
[225] P. Debnath, B.J. Cherayil, J. Chem. Phys. 118 (2003) 1970.
[226] J. Wilhelm, E. Frey, Phys. Rev. Lett. 77 (1996) 2581, and references cited herein.
[227] P.G. de Gennes, The Physics of Liquid Crystals, Clarendon Press, Oxford, 1974.
[228] G. Vertogen, W.H. de Jeu, Thermotropic Liquid Crystals, Fundamentals, Springer, Berlin, 1988.
[229] S. Chandrasekhar, Liquid Crystals, Cambridge University Press, Cambridge, UK, 1971.
[230] J.P. Bareman, G. Cardini, M.L. Klein, Phys. Rev. Lett. 60 (1988) 2152.
[231] J. Baschnagel, K. Binder, Physica A 204 (1994) 47.
[232] M.E. Mann, C.H. Marshall, A.D.J. Haymet, Mol. Phys. 66 (1989) 493.
[233] C.W. Greeff, M.A. Lee, Phys. Rev. 49 (1994) 3225.
[234] D. Frenkel, Mol. Phys. 60 (1987) 1.
[235] L.F. Rull, Physica A 80 (1995) 113.
[236] D.J. Adams, G.R. Luckhurst, R.W. Phippen, Mol. Phys. 61 (1987) 1575.
[237] E. Egberts, H.J.C. Berendsen, J. Chem. Phys. 89 (1988) 3718.
[238] R.R. Netz, A.N. Berker, Phys. Rev. Lett. 68 (1992) 333.
[239] D. Levesque, M. Mazars, J.-J. Weis, J. Chem. Phys. 103 (1995) 3820.
[240] A.L. Tsykalo, Mol. Cryst. Liq. Cryst. 129 (1985) 409.
[241] S. Hess, D. Frenkel, M.P. Allen, Mol. Phys. 74 (1991) 765.
[242] M.A. Glaser, R. Malzbender, N.A. Clark, D.M. Walba, Mol. Simul. 14 (1995) 343.
[243] R.D. Kamien, G.S. Grest, Phys. Rev. E 55 (1997) 1197.
[244] H. Heller, M. Schaefer, K. Schulten, J. Phys. Chem. 97 (1993) 8343.
[245] M.P. Allen, in: M. Baus, L.F. Rull, J.P. Ryckaert (Eds.), Observation, Prediction and Simulation of Phase Transitions on Complex Fluids, Kluwer Academic Publ., Dordrecht, 1995.
[246] B.H. Zimm, W.H. Stockmayer, J. Chem. Phys. 17 (1949) 1301.
[247] C.W. Cross, B.M. Fung, J. Chem. Phys. 101 (1994) 6839.
[248] A.V. Komolkin, A. Maliniak, Mol. Phys. 84 (1995) 1227.
[249] D.C. Rapaport, The Art of Molecular Dynamics Simulation, Cambridge University Press, Cambridge, UK, 1995.
[250] J.A. Board, J.W. Causey, J.F. Leathrum, A. Windemuth, K. Schulten, J. Chem. Phys. Lett. 198 (1992) 89.
[251] A. Windemuth, K. Schulten, Mol. Simul. 5 (1991) 353.
[252] E. Paci, M. Marchi, J. Phys. Chem. 100 (1996) 4314.
[253] G.V. Paolini, G. Ciccotti, M. Ferrario, Mol. Phys. 80 (1993) 297.
[254] A.L. Tsykalo, Thermophysical Properties of Liquid Crystals, Gordon and Breach Science, London, 1991.
[255] M. Kröger, Makromol. Chem. Macromol. Symp. 133 (1998) 101.
[256] R.H.W. Wientjes, R.J.J. Jongschaap, M.H.G. Duits, J. Mellema, J. Rheol. 43 (1999) 375.
[257] S.H. Kim, H.G. Sim, K.H. Ahn, S.J. Lee, Korea-Australia Rheol. J. 14 (2002) 49.
[258] K.R. Geurts, L.E. Wedgewood, J. Chem. Phys. 106 (1997) 339.

[259] R.D. Groot, A. Bot, W.G.M. Agterof, J. Chem. Phys. 104 (1996) 9202.
[260] M. Doi, J. Polym. Sci. Polym. Phys. Ed. 21 (1983) 667.
[261] R. Ketzmerick, H.C. Öttinger, Continuum Mech. Thermodyn. 1 (1989) 113.
[262] C. Tsenoglou, ACS Polym. Preprints 28 (1987) 185.
[263] J. des Cloizeaux, Europhys. Lett. 5 (1988) 437.
[264] N.P.T. O'Connor, R.C. Ball, Macromolecules 25 (1992) 5677.
[265] J. Fang, M. Kröger, H.C. Öttinger, J. Rheol. 44 (2000) 1293.
[266] D.C. Venerus, H. Kahvand, J. Rheol. 38 (1994) 1297, and references cited herein.
[267] J.P. Oberhauser, L.G. Leal, D.W. Mead, J. Polym. Sci. Polym. Phys. 36 (1998) 265.
[268] C.C. Hua, J.D. Schieber, J. Chem. Phys. 109 (1998) 10018.
[269] C.C. Hua, J.D. Schieber, D.C. Venerus, J. Chem. Phys. 109 (1998) 10028.
[270] C.C. Hua, J.D. Schieber, D.C. Venerus, J. Rheol. 43 (1999) 701.
[271] J.D. Schieber, J. Neergard, S. Gupta, J. Rheol. 47 (2003) 213.
[272] D.W. Mead, R.G. Larson, M. Doi, Macromolecules 31 (1998) 7895.
[273] H.C. Öttinger, J. Rheol. 43 (1999) 1461.
[274] M. Doi, J. Takimoto, Phil. Trans. R. Soc. London Ser. A 361 (2003) 641.
[275] M.H. Wagner, J. Rheol. 38 (1994) 655.
[276] M.H. Wagner, V Schulze, A. Gottfert, Polym. Eng. Sci. 36 (1996) 925.
[277] A. Peterlin, H.A. Stuart, in: A. Eucken, K.I. Wolf (Eds.), Hand- und Jahrbuch d. Chem. Phys., Vol. 8, 1943, p. 113.
[278] M. Kröger, S. Hess, Physica A 195 (1993) 336.
[279] S. Hess, Physica A 86 (1977) 383;
S. Hess, Physica A 87 (1977) 273;
S. Hess, Physica A 112 (1982) 287.
[280] H. Giesekus, Rheol. Acta 2 (1962) 50.
[281] T. Masuda, K. Kitagawa, I. Inoue, S. Onogi, Macromolecules 3 (1970) 109.
[282] L.A. Holmes, S. Kusamizu, K. Osaki, J.D. Ferry, J. Polym. Sci. A 2 (1971) 2009.
[283] M. Kröger, Makromol. Chem. Macromol. Symp. 81 (1994) 83.
[284] A. Lozinski, C. Chauviere, J. Fang, R.G. Owens, J. Rheol. 47 (2003) 535.
[285] M. Laso, M. Picasso, H.C. Öttinger, AIChE J. 43 (1997) 877.
[286] M. Abramowitz, I.A. Stegun, NBS Handbook of Mathematical Functions, Dover, Washington, DC, 1964, p. 804.
[287] M. Kröger, H.S. Sellers, J. Chem. Phys. 103 (1995) 807.
[288] F.M. Leslie, Arch. Rat. Mech. Anal. 28 (1968) 265.
[289] F.M. Leslie, Continuum Mech. Thermodyn. 4 (1992) 167.
[290] J.L. Ericksen, Arch. Rat. Mech. Anal. 113 (1991) 197.
[291] D. Baalss, S. Hess, Z. Naturforsch. 43a (1988) 662.
[292] G.L. Hand, Arch. Rat. Mech. Anal. 7 (1961) 81.
[293] S.-D. Lee, J. Chem. Phys. 88 (1988) 5196.
[294] L.A. Archer, R.G. Larson, J. Chem. Phys. 103 (1995) 3108.
[295] G.L. Hand, J. Fluid Mech. 13 (1962) 33.
[296] S. Hess, Z. Naturforsch. 30a (1975) 728.
[297] C. Pereira Borgmeyer, S. Hess, J. Non-Equilibrium Thermodyn. 20 (1995) 359.
[298] I. Pardowitz, S. Hess, Physica A 100 (1980) 540.
[299] S. Hess, I. Pardowitz, Z. Naturforsch. 36a (1981) 554.
[300] E.H. Macmillan, J. Rheol. 33 (1989) 1071.
[301] J.L. Ericksen, Arch. Rat. Mech. Anal. 4 (1969) 231.
[302] G. Marrucci, Mol. Cryst. Liq. Cryst. 72 (1982) 153.
[303] A.N. Semonov, Zh. Eksp. Teor. Fiz. 85 (1983) 549.
[304] S. Yamamoto, T. Matsuoka, J. Chem. Phys. 100 (1994) 3317.
[305] H. Brenner, D.W. Condiff, J. Colloids Interface Sci. 47 (1974) 199.
[306] M. Kröger, H.S. Sellers, A molecular theory for spatially inhomogeneous, concentrated solutions of rod-like liquid crystal polymers, in: L. Garrido (Ed.), Complex Fluids, Lecture Notes in Physics, Vol. 415, Springer, New York, 1992, p. 295.

[307] G.K. Batchelor, J. Fluid Mech. 46 (1971) 813.
[308] M. Doi, J. Polym. Sci. Polym. Phys. 19 (1981) 229.
[309] S. Hess, Z. Naturforsch. 31a (1976) 1507.
[310] M. Kröger, H.S. Sellers, Phys. Rev. E 56 (1997) 1804.
[311] T. Carlsson, Mol. Cryst. Liq. Cryst. 89 (1982) 57.
[312] T. Carlsson, J. Phys. 44 (1983) 909.
[313] D.J. Ternet, R.G. Larson, R.G. Leal, Rheol. Acta. 38 (1999) 183.
[314] A.V. Zakharov, A.V. Komolkin, A. Maliniak, Phys. Rev. E 59 (1999) 6802.
[315] M. Fialkowski, Phys. Rev. E 58 (1998) 1955.
[316] T. Carlsson, K. Skarp, Mol. Cryst. Liq. Cryst. 78 (1981) 157.
[317] H. Ehrentraut, S. Hess, Phys. Rev. E 51 (1995) 2203.
[318] F.P. Bretherton, J. Fluid Mech. 14 (1962) 284.
[319] E.J. Hinch, L.G. Leal, J. Fluid Mech. 76 (1976) 187.
[320] M. Kröger, P. Ilg, S. Hess, J. Phys.: Condens. Matter 15 (2003) S1403.
[321] P. Ilg, M. Kröger, Phys. Rev. E 66 (2002) 021501.
[322] M.A. Martsenyuk, Yu L. Raikher, M.I. Shliomis, Sov. Phys. JETP 38 (1974) 413.
[323] P. Ilg, M. Kröger, S. Hess, A.Y. Zubarev, Phys. Rev. E 67 (2003) 061401.
[324] G. Rienäcker, M. Kröger, S. Hess, Phys. Rev. E 66 (2002) 040702.
[325] R.G. Larson, H.C. Öttinger, Macromolecules 24 (1991) 6270.
[326] P.L. Maffettone, S. Crescitelli, J. Rheol. 38 (1994) 1559.
[327] M. Grosso, R. Keunings, S. Crescitelli, P.L. Maffettone, Phys. Rev. Lett. 86 (2001) 3184.
[328] A.L. Yarin, O. Gottlieb, I.V. Roisman, J. Fluid Mech. 340 (1997) 83.
[329] G. Rienäcker, M. Kröger, S. Hess, Physica A 315 (2002) 537.
[330] P.D. Olmsted, P. Goldbart, Phys. Rev. A 41 (1990) 4578;
P.D. Olmsted, P. Goldbart, Phys. Rev. A 46 (1992) 4966.
[331] J. Mewis, M. Mortier, J. Vermant, P. Moldenaers, Macromolecules 30 (1997) 1323.
[332] G. Rienäcker, S. Hess, Physica A 267 (1999) 294.
[333] N.C. Andrews, A.J. McHugh, B.J. Edwards, J. Rheol. 40 (1996) 459.
[334] G. Marrucci, F. Greco, Mol. Cryst. Liq. Cryst. 206 (1991) 17.
[335] G. Sgalari, G.L. Leal, J.J. Feng, J. Non-Newtonian Fluid Mech. 102 (2002) 361.
[336] R. Bandyopadhyay, G. Basappa, A.K. Sood, Phys. Rev. Lett. 84 (2002) 2022.
[337] K.S. Kumar, T.R. Ramamohan, J. Rheol. 39 (1995) 1229.
[338] M.E. Cates, D.A. Head, A. Ajdari, Phys. Rev. E 66 (2002) 025202(R).
[339] A.S. Wunenburger, A. Colin, J. Leng, A. Arneodo, D. Roux, Phys. Rev. Lett. 86 (2001) 1374.
[340] H.C. Öttinger, J. Non-Equilibrium Thermodyn. 22 (1997) 386.
[341] W.S. Koon, J.E. Marsden, Rep. Math. Phys. 40 (1997) 21.
[342] V.O. Solovievm, J. Math. Phys. 34 (1993) 5747.
[343] D. Lewis, J. Marsden, R. Montgomery, Physica D 18 (1986) 391.
[344] J.A. De Azcarraga, J.M. Izquierdo, A.M. Perelomov, J.C. Perez-Bueno, J. Math. Phys. 38 (1997) 3735.
[345] L. Takhtajan, Commun. Math. Phys. 160 (1994) 295.
[346] J. Grabowski, G. Marmo, J. Phys. A 32 (1999) 4239.
[347] H.C. Öttinger, Appl. Rheol. 9 (1999) 17.
[348] M. Kröger, M. Hütter, H.C. Öttinger, Comput. Phys. Commun. 137 (2001) 325.
[349] G. Ianniruberto, G. Marrucci, J. Non-Newtonian Fluid Mech. 79 (1998) 225.
[350] H.C. Öttinger, J. Non-Newtonian Fluid Mech. 89 (1999) 165.
[351] E.G. Flekkoy, P.V. Coveney, Phys. Rev. Lett. 83 (1999) 1775.
[352] M. Serrano, P. Espanol, Phys. Rev. E 64 (2001) 046115.
[353] S. Succi, I.V. Karlin, H. Chen, Rev. Mod. Phys. 74 (2002) 1203.
[354] I.V. Karlin, A. Ferrante, H.C. Öttinger, Europhys. Lett. 47 (1999) 182.
[355] W. Dzwinel, NEPTIS 11, 8–10 December, Kyoto, Japan, 2002.
[356] J. Honerkamp, Stochastische Dynamische Systeme, VCH, Weinheim, 1990.
[357] H. Risken, The Fokker–Planck equation, Springer, Berlin, 1984.

[358] A. Schenzle, H. Brand, Phys. Rev. A 20 (1979) 1628.
[359] S. Nakajima, Prog. Theor. Phys. 20 (1958) 948.
[360] R.W. Zwanzig, J. Chem. Phys. 33 (1960) 1338.
[361] R.W. Zwanzig, Lectures in Theoretical Physics, Vol. 3, Wiley-Interscience, New York, 1961.
[362] H. Grabert, Projection Operator Techniques in Nonequilibrium Statistical Mechanics, Springer, New York, 1982.
[363] H.C. Öttinger, Phys. Rev. E 57 (1998) 1416.
[364] V.G. Mavrantzas, H.C. Öttinger, Macromolecules 35 (2002) 960.
[365] V.A. Harmandaris, V.G. Mavrantzas, D.N. Theodorou, M. Kröger, J. Ramirez, H.C. Öttinger, D. Vlassopoulos, Macromolecules 36 (2003) 1376.
[366] J.D. Schieber, H.C. Öttinger, J. Rheol. 38 (1994) 1909.
[367] M. Kröger, J. Ramirez, H.C. Öttinger, Polymer 43 (2002) 477.
[368] H.C. Öttinger, Coarse-graining wormlike polymer chains for substantiating reptation, J. Non-Newtonian Fluid Mech. (2004), in press.
[369] M. Murat, K. Kremer, J. Chem. Phys. 108 (1998) 4340.
[370] S.C. Glotzer, W. Paul, Ann. Rev. Mater. Res. 32 (2002) 401.